DEVELOPMENT OF HIGH PERFORMANCE MULTICOLOR QUANTUM WELL INFRARED PHOTODETECTORS AND STUDIES OF ENHANCING LIGHT COUPLING AND RADIATION EFFECTS IN QWIPS

Dr. Sheng S. Li

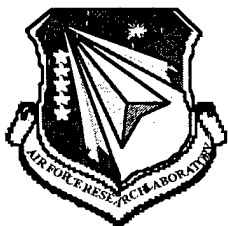Dept. of Electrical and Computer Engineering
University of Florida
Gainsville, FL 32611-6130

July 1999

Final Report

20000204 115

AIR FORCE RESEARCH LABORATORY
Space Vehicles Directorate
3550 Aberdeen Ave SE
AIR FORCE MATERIEL COMMAND
KIRTLAND AIR FORCE BASE, NM 87117-5776

AFRL-VS-TR-1999-1100

This report has been reviewed by the Public Affairs Office and is releasable to the National Technical Information Service (NTIS). At NTIS, it will be available to the general public, including foreign nationals.

If you change your address, wish to be removed from this mailing list, or your organization no longer employs the addressee, please notify AFRL/VSSS, 3550 Aberdeen Ave SE, Kirtland AFB, NM 87117-5776.

Do not return copies of this report unless contractual obligations or notice on a specific document requires its return.

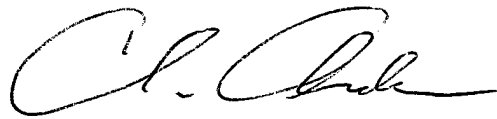This report has been approved for publication.

DAVID CARDIMONA
Project Manager

FOR THE COMMANDER

KEITH A. SHROCK, DR-3   CHRISTINE M. ANDERSON, SES
Chief, Space Sensing &   Director, Space Vehicles
Vehicle Control Branch

REPORT DOCUMENTATION PAGE

Form Approved
OMB No. 0704-0188

Public reporting burden for this collection of information is estimated to average 1 hour per response, including the time for reviewing instructions, searching existing data sources, gathering and maintaining the data needed, and completing and reviewing the collection of information. Send comments regarding this burden estimate or any other aspect of this collection of information, including suggestions for reducing this burden, to Washington Headquarters Services, Directorate for Information Operations and Reports, 1215 Jefferson Davis Highway, Suite 1204, Arlington, VA 22202-4302, and to the Office of Management and Budget, Paperwork Reduction Project (0704-0188), Washington, DC 20503.

1. AGENCY USE ONLY *(Leave blank)*	2. REPORT DATE	3. REPORT TYPE AND DATES COVERED
	July 10, 1999	Final Report; 3/2/98-6/30/99

4. TITLE AND SUBTITLE
Development of High Performance Multicolor Quantum Well Infrared Photodetectors and Studies of Enhancing Light Coupling and Radiation Effects in QWIPs

5. FUNDING NUMBERS
#F29601-98-C-0022 BAA
Program Element: 62601F
Project: 8809
Task: TJ
Work Unit: AC

6. AUTHOR(S)
Sheng S. Li

7. PERFORMING ORGANIZATION NAME(S) AND ADDRESS(ES)
University of Florida
561 EB-33, P. O. Box 116130
Gainesville, FL 32611-6130

8. PERFORMING ORGANIZATION REPORT NUMBER

9. SPONSORING/MONITORING AGENCY NAME(S) AND ADDRESS(ES)
Air Force Research Laboratory (AFRL)
3550 Aberdeen Ave., S. E.
Kirtland AFB, NM 87117-5776

10. SPONSORING/MONITORING AGENCY REPORT NUMBER

AFRL-VS-TR-1999-1100

11. SUPPLEMENTARY NOTES
The views, opinions, and/or findings contained in this report are those of the author(s) and should not be construed as an official Department of the Air Force position, policy, or decision, unless so designated by other documentation.

12a. DISTRIBUTION AVAILABILITY STATEMENT
Approved for public release; distribution unlimited.

12b. DISTRIBUTION CODE

13. ABSTRACT *(Maximum 200 words)*
In this report, we present the design, fabrication, and characterization of several high performance multi-color and broadband quantum well infrared photodetectors (QWIPs) for both MWIR and LWIR applications. The report covers tasks performed during the period from March 3, 1998 through July 10, 1999. A very high sensitivity, high-strain, multi-color triple-coupled (TC-) QWIP using InGaAs/AlGaAs/InGaAs material systems has been developed in this project for LWIR multi-color detection. A two-stack InGaAs/AlGaAs/InGaAs TC-QWIP and InGaAs/AlGaAs BC-QWIP has been developed for the LWIR and MWIR dual-band detection. In addition, a high-strain InGaAs/GaAs BC-QWIP with and without two-dimensional (2-D) grating coupler has been designed, fabricated, and characterized for the LWIR detection. This device shows very high responsivity under 45° back-illumination. Several broadband (BB-) QWIPs have been developed for the LWIR detection. These include (1) two-stack, five-well n-type InGaAs/AlGaAs broadband (BB-) QWIPs with 3- and 7-period QWs in the unit cell, (2) 3- and 4-well n-type BB-QWIPs, and (3) two 3- and 4- well p-type BB-QWIPs. In addition, a three-stack InGaAs/AlGaAs/InGaAs BB TC-QWIP grown on GaAs substrate has been developed for LWIR detection, which has a FWHM spectral bandwidth twice larger than the single-stack TC-QWIP. Finally, a MWIR InGaAs/InAlAs TC-QWIP grown on InP substrate, operating up to T = 116K with excellent device performance, has also been demonstrated. Four journal papers and six conference papers have been published and presented from this work.

14. SUBJECT TERMS
Quantum Well Infrared Photodetector (QWIP), multi-color, multi-stack, high- strain (HS), triple-coupled (TC) QWIP, broadband (BB) QWIP, LWIR, MWIR.

15. NUMBER OF PAGES
130

16. PRICE CODE

17. SECURITY CLASSIFICATION OF REPORT	18. SECURITY CLASSIFICATION OF THIS PAGE	19. SECURITY CLASSIFICATION OF ABSTRACT	20. LIMITATION OF ABSTRACT
UNCLASSIFIED	UNCLASSIFIED	UNCLASSIFIED	Same as Item 12a.

Standard Form 298 (Rev. 2-89) (EG)
Prescribed by ANSI Std. 239.18
Designed using Perform Pro, WHS/DIOR, Oct 94

TABLE OF CONTENTS

LIST OF FIGURES

LIST OF TABLES

1 SUMMARY

This is the final report for a research program performed under contract with the Air Force Research Laboratory (contract # F29601-98-C-0022). The objective of this project is to develop new high performance multicolor quantum well infrared photodetectors (QWIPs) for IR imaging and low background detection applications in the 3-5 μm (MWIR) and 8-14 μm (LWIR) wavelength bands using III-V semiconductor material systems grown by the MBE technique. The scope of this program includes the design, growth, and fabrication of multi-color QWIPs as well as electrical and radiometric testing of these detectors. The purpose of the testing is to obtain sufficient data to determine the usefulness of the QWIPs developed under this project for future space surveillance applications. In addition, the program will also cover the investigation of new light coupling schemes aimed at enhancing the absorption quantum efficiency of QWIPs in order to increase the sensitivity of the detectors for detection of faint targets and for low background and low temperature (40K) applications. For low temperature operation, the device's dark current will be dominated by defect-assisted tunneling (DAT) process. As a result, defects are expected to play an important role in low temperature operation of QWIPs. To meet this challenge we will perform Deep Level Transient Spectroscopy (DLTS) measurements on QWIPs to identify interface and barrier defects in the QWIP and to correlate these defects to the dark current of the detectors. From this study, improved and optimized QWIP structures will be developed for low background detection.

A. Research Achievements:

This final technical report covers the research accomplishments of the first year of a research program on the development of high performance multi-color QWIPs for both MWIR and LWIR applications (originally scheduled to last four years). The research accomplishments during the first year funding are summarized as follows.

1. Demonstrated a high sensitivity, high-strain InGaAs/AlGaAs/InGaAs multi-color triple-coupled quantum well infrared photodetector (TC-QWIP) for 8-14 µm long-wavelength detection. Detailed results are depicted in chapter 2.

2. Demonstrated a InGaAs/AlGaAs/InGaAs broadband triple-coupled quantum well infrared photodetector (BB TC-QWIP) for 8-14 µm long-wavelength detection. Detailed results are depicted in chapter 3.

3. Design, fabrication, and characterization of a MWIR TC-QWIP. The results are described in chapter 4.

4. Demonstrated a multi-color, two-stack, high-strain InGaAs/AlGaAs/InGaAs asymmetrical triple-coupled (TC-) QWIP and an InGaAs/AlGaAs bound-to-continuum (BC-) QWIP for LWIR and MWIR dual band detection. Detailed results are discussed in chapter 5.

5. Demonstrated a n-type GaAs/InGaAs high-strain bound-to-continuum quantum well infrared photodetector (HS BC-QWIP) for LWIR detection. The results are described in chapter 6.

6. Demonstrated three-well, four-well, and five-well n-type and two three-well p-type $In_xGa_{1-x}As/Al_yGa_{1-y}As$ broadband quantum well infrared photodetectors (BB-QWIPs) grown on GaAs substrate for 7–14 µm LWIR detection. The results are depicted in chapter 7.

7. Published four journal papers and presented six invited and contributed papers at the international symposium on long wavelength infrared detectors and arrays and the SPIE Conference on Infrared Detectors and Materials.

B. Publications

(a) Referred journal papers:

1. J. Chu, Sheng S. Li, and A. Singh, "Investigation of Broadband Quantum Well Infrared Photodetectors for 8-14 µm Detection," IEEE J. of Quantum Electronics, vol.35 (3), pp.312-319, March, 1999.

2. J. Chu, <u>Sheng S. Li</u>, and A. Singh, "Broadband P-Type Quantum Well Infrared Photodetectors," Appl. Phys. Letts., vol.**73** (23), pp.3414-3416, Dec.7 1998.

3 . J. C. Chiang and <u>Sheng S. Li</u>, "Ultra-high Sensitivity, High-Strain InGaAs/AlGaAs/InGaAs Triple-Coupled Quantum Well Infrared Photodetector," Electronics Letts., vol.**34** (18), pp.1794-1795, Sept.2, 1998.

4. J. Chu, <u>Sheng S. Li</u>, A. Singh, and P. Ho, "A Normal Incidence P-type Strain Layer Quantum Well Infrared Photodetector with 19.2 μm Peak Detection Wavelength," Appl. Phys. Letts., vol.**73** (12), pp.1664-1666, Sept.21, 1998.

(b) <u>Conference Presentations and Proceeding Papers</u>

1. Sheng S. Li, J. Chu, and A. Singh, " Broadband Quantum Well Infrared Photodetectors for MWIR and LWIR Detection," <u>invited paper</u>, presented at SPIE International Conference on Photodetectors: Materials and Devices IV, San Jose, CA, Jan. 24-26, 1999. Full paper in Conference Proceedings.

2. <u>Sheng S. Li</u>, J. C. Chiang, J. H. Lee, A. Singh, "Voltage Tunable Multi-color Triple-coupled Quantum Well Infrared Photodetectors for MWIR and LWIR Detection," <u>invited paper</u>, presented at *6th Intn. Symposium on Long Wavelength Infrared Detectors and Arrays: Physics and Applications*, Boston, MA, Nov. 5-6, 1998. Proceedings: ECS-PV-98-21, pp.134-144 (1998).

3. J. C. Chiang, <u>Sheng S. Li</u>, and A. Singh, "High Sensitivity Normal Incidence Triple-coupled Quantum Well Infrared Photodetector for Lower Background Infrared Detection," presented at SPIE AeroSense Conf. on Infrared Detectors and Focal Plane Arrays V, Orlando, FL, April 14-17, 1998. *Proc. of SPIE,* vol.3379-22 pp. 213-224 (1998).

4. J. C. Chiang, <u>Sheng S. Li</u>, and A. Singh, "Two-Stack Indirect-barrier/triple-coupled Quantum Well Infrared Photodetector for Mid-wavelength and Long-Wavelength Infrared Detection," presented at SPIE AeroSense Conf. on Infrared Detectors and Focal Plane Arrays V, Orlando, FL, April 14-17, 1998. Full paper published in the *Proc. of SPIE*, vol.3379-29, pp.274-287 (1998).

5. J. T. Chu, <u>Sheng S. Li</u>, and A. Singh, "Broadband LWIR Quantum Well Infrared Photodetectors," presented at SPIE AeroSense Conf. on Infrared Detectors and Focal Plane Arrays V, Orlando, FL, April 14-17, 1998.

6. J. T. Chu, <u>Sheng S. Li</u>, and A. Singh, "Voltage Tunable P-Type Superlattice Infrared Photodetector," presented at SPIE AeroSense Conf. on Infrared Detectors and Focal Plane Arrays V, Orlando, FL, April 14-17, 1998.

2 A HIGH PERFORMANCE HIGH STRAIN TRIPLE-COUPLED QUANTUM WELL INFRARED PHOTODETECTOR

2.1 Introduction

Quantum well infrared photodetectors (QWIPs) based on high-strain InGaAs material grown on the GaAs substrate have been investigated for both the 3 – 5 μm mid-wavelength and 8 – 14 μm long-wavelength infrared detection [1-5]. Due to the quantum mechanical selection rule, the intersubband absorption under normal incident illumination is usually not allowed in n-type QWIPs. As a result, a metal or dielectric grating coupler [5-7] is required for most n-type QWIPs in order to achieve normal incident absorption. The unique feature of these high-strain QWIPs is that a large normal incident absorption without using grating coupler has been observed, which has a responsivity ratio of the normal incidence to the 45° incidence ranging from 30 % to 50 %. It indicates that high sensitivity gratingless normal incidence n-type QWIPs can be achieved by optimizing the QWIP's structure. In addition, it can greatly reduce the fabricating complexity, which can significantly reduce the cost of n-type QWIP focal plane arrays (FPAs).

In this chapter, a high sensitivity triple-coupled quantum infrared photodetector (TC-QWIP) using high-strain n-type $In_{0.25}Ga_{0.75}As/Al_{0.11}Ga_{0.89}As/In_{0.12}Ga_{0.88}As$ asymmetrical coupled quantum well structure has been developed for 8 – 14 μm LWIR detection.

2.2 Device Design and Fabrication

The high-strain TC-QWIP consists of a highly doped (n = 7×10^{17} cm^{-3}) high-strain (HS) $In_{0.12}Ga_{0.88}As$ quantum well of 5.5 nm thick, two undoped thin $Al_{0.11}Ga_{0.89}As/In_{0.12}Ga_{0.88}As$ (2/4 nm layer thickness) quantum wells separated by a 50 nm $Al_{0.11}Ga_{0.89}As$ barrier layer; this basic structure is repeated 5 and 10 times in series to

form a two-stack HS TC-QWIP with 5-period and 10-period multiquantum wells. Finally, a 0.1 μm thick undoped GaAs layers was grown between the multiquantum wells and the top and bottom GaAs contact layers (both doped to $n = 2 \times 10^{18}$ cm^{-3}) to reduce the tunneling current from contacts to QWs, which results in a lower dark current. Table 2.1 lists the layer structure of this high-strain TC-QWIP. Figure 2.1(a) shows the schematic diagram of the conduction band and the bound state energy levels for this high-strain TC-QWIP structure, and Fig. 2.1(b) shows the calculated transmission probability under zero bias condition.

For the TC-QWIP, due to the strong coupling effect of the three asymmetrical QWs and two thin AlGaAs barriers, the bound states in the In$_z$Ga$_{1-z}$As QWs and the first excited state in the In$_x$Ga$_{1-x}$As QW are coupled to form the second (E_2) and third (E_3) bound states inside the TC-QWs, as illustrated in Fig. 2.1(a). The intersubband transition for this TC-QWIP is dominated by the $E_1 \rightarrow E_3$ (λ_{13} = 10.9 μm at zero bias) bound-to-bound (BTB) state transition, while a secondary photoresponse peak due to $E_1 \rightarrow E_C$ (λ_{1C} = 8.8 μm at 0 V) bound-to-continuum (BTC) state transition was also observed in this device.

The test structure with an active area of 200×200 μm^2 was fabricated on the QWIP samples by standard wet chemical etching for device characterization use. The mesa structure of the 5-period HS TC-QWIP was formed first by completely removing the top contact layer and the 10-period-stack, and then by etching down from the middle contact layer to the bottom contact layer. The mesa structure of the 10-period HS TC-QWIP was formed by etching down from the middle contact layer to the bottom contact layer. A square ohmic contact ring composed of AuGe/Ni/Au was then deposited on the periphery

of the mesa structure of the highly doped contact layers and alloyed for the ohmic contacts. Finally, the devices were prepared both with 45° polished facet on the substrate for coupling incident IR radiation into the quantum wells and with a front-side normal incident illumination.

2.3 Results and Discussion

2.3.1 Dark Current Measurements

Figure 2.2 shows the temperature dependence of the dark J-V curves of the 5-period HS TC-QWIP. The dark J-V curves show an asymmetrical behavior which is a common feature for the n-type QWIPs. The 300 K window currents with a 180° FOV was also shown in Fig. 2.2, and the BLIP temperature was found to be 65 K with bias voltages up to -3 V. This is 5 K higher than the lightly strained TC-QWIP discussed in reference [8]. Figure 2.3 shows the temperature dependence of the dark J-V curves of the 10-period HS TC-QWIP. The dark J-V curves show a similar behavior as those of the 5-period HS TC-QWIP. The 300 K window currents with a 180° FOV was also shown in Fig. 2.3, and the BLIP temperature was found to be 65 K with biases up to -5 V, which is similar to the 5-period TC-QWIP. For comparison, Fig. 2.4 shows the dark J-V versus the electric field (assumed the bias voltage is uniformly distributed across the whole structure) for the 5- and 10-period TC- QWIPs at 77 K. The result shows that the 5-period device has a higher dark current than that of the 10-period QWIP under same applied electric field.

2.3.2 Photoresponse Measurements

The photocurrent spectra were measured with 45° facet illumination and with front-side normal incidence illumination using a 0.25 m grating monochromator and a

calibrated blackbody source at $T = 1000°$ C. Figure 2.5 shows the spectral responsivity of the 5-period HS TC-QWIP measured with a 45° facet at V_b = -3, -2.8 and -2.6 V and $T =$ 30 K; the inset shows the linear dependence of the peak wavelengths for both $E_1 \rightarrow E_3$ and $E_1 \rightarrow E_C$ transitions with the applied bias voltage. The wavelength tunabilities for this device are ranging from 6.9 to 7.3 μm and 9.6 to 10.1 μm for the $E_1 \rightarrow E_C$ and $E_1 \rightarrow$ E_3 transitions, respectively. The interpolated peak wavelengths at zero bias are found to be 8.6 μm and 11.1 μm for the $E_1 \rightarrow E_C$ and $E_1 \rightarrow E_3$ transitions, respectively, which are in good agreement with the calculated peak wavelengths at zero bias: 8.8 μm and 10.9 μm, respectively, as shown in Fig. 2.1(b). The peak responsivities were found to be increased with the bias voltage up to -3 V and the maximum peak responsivity was found to be of 2.77 A/W at λ_p = 9.6 μm, V_b = -3 V and T = 30 K. We also measured the spectral responsivity of this device with a front-side normal incidence illumination. The results are shown in Fig. 2.6 along with those of 45° facet illumination. It was found that the responsivity ratios of the normal incidence to 45° incidence are 55 % - 75 % and 60 % - 80 % for the $E_1 \rightarrow E_C$ and $E_1 \rightarrow E_3$ transitions, respectively. Figure 2.7 shows the spectral responsivity of the 10-period HS TC-QWIP measured with a 45° facet illumination at V_b = -5, -4.5 and -4 V and T = 30 K; the inset shows the linear dependence of the peak wavelengths for both $E_1 \rightarrow E_3$ and $E_1 \rightarrow E_C$ transitions with the applied bias voltage. The wavelength tunabilities and the peak responsivities for this device were found to be almost the same as those of 5-period device, but requires a higher bias voltage applied to the device. Figure 2.8 shows the peak responsivities versus the bias voltage for both the normal incidence and 45° incidence devices measured at T = 30 K. It was found that the responsivity ratios of the normal incidence to 45° incidence are 30 % - 40 % and 50 % -

60 % for the $E_1 \rightarrow E_C$ and $E_1 \rightarrow E_3$ transitions, respectively, which are lower than those of the 5-period device. Figure 2.9 shows the temperature dependence of the peak responsivity for the $E_1 \rightarrow E_3$ transition versus the electric field with a 45° incidence illumination. From the results of this study, it is noted that (1) the 5-period device has larger peak responsivity than those of the 10-period device under the same temperature and electric field conditions and (2) for each same period device, the peak responsivity is increased by up to 200 % when the temperature was raised from 30 K to 77 K, and (3) both devices show very large normal incidence absorption and responsivity.

2.3.3 Detectivity

Figures 2.10 and 2.11 show the calculated detectivities for both the 5-period and 10-period devices at 77 K and 30 K, respectively, using the noise model by Wang et al. [9]. The results show that the 10-period device has a higher non-BLIP detectivity of 2.93×10^{10} cm-Hz$^{1/2}$/W at λ_p = 9.8 μm, V_b = -4.5 V and 77 K, but the 5-period device has a higher BLIP detectivity of 2.21×10^{10} cm-Hz$^{1/2}$/W at λ_p = 9.6 μm, V_b = -3 V and 30 K.

2.4 Conclusions

In conclusion, we have demonstrated a very high performance voltage-tunable TC-QWIP using high-strain n-type $In_{0.25}Ga_{0.75}As/Al_{0.11}Ga_{0.89}As/In_{0.12}Ga_{0.88}As$ asymmetrical coupled quantum well structure for 8 – 14 μm LWIR detection. The maximum responsivities at λ_p = 9.6 μm were found to be 1.71 A/W and 2.77 A/W at V_b = -2.8 V, -3 V and T = 77 K, 30 K, respectively, for the 5-period device. For the 10-period device, the maximum responsivities were found to be 1.3 A/W and 2.71 A/W at λ_p = 9.8 μm, V_b = -4.5 V, and T = 77 K, and at λ_p = 9.6 μm, V_b = -5 V, and T = 30 K, respectively. The

maximum detectivities were found to be 1.44×10^{10} cm-Hz$^{1/2}$/W and 2.93×10^{10} cm-Hz$^{1/2}$/W at λ_p = 9.9 μm, V_b = -2.6 V and T = 77 K, and at λ_p = 9.8 μm, V_b = -4.5 V, and T = 77 K for the 5-period and 10-period devices, respectively. It is shown that this HS TC-QWIP can be used as a voltage-tunable two-color or multicolor QWIP for lower background LWIR detection. In addition, the device shows very large normal incidence absorption, which offers excellent possibility for fabricating low cost, large area gratingless TC-QWIP focal plane arrays (FPAs) for IR imaging camera applications.

Table 2.1 The layer structure of a high performance, high-strain InGaAs/AlGaAs/InGaAs TC-QWIP grown on GaAs substrate for LWIR detection.

Layer		Thickness (Å)	Dopant	Concentration (cm^{-3})
n GaAs (top contact)		5000	Si	2×10^{18}
i GaAs		1000	none	none
i Al$_{0.11}$Ga$_{0.89}$As		500	none	none
i In$_{0.12}$Ga$_{0.88}$As		35	none	none
i Al$_{0.11}$Ga$_{0.89}$As		20	none	none
i In$_{0.12}$Ga$_{0.88}$As	X 10	40	none	none
i Al$_{0.11}$Ga$_{0.92}$As		20	none	none
n In$_{0.25}$Ga$_{0.75}$As		55	Si	7×10^{17}
i Al$_{0.11}$Ga$_{0.89}$As		500	none	none
i GaAs		1000	none	none
n GaAs		5000	Si	2×10^{18}
i GaAs		1000	none	none
i Al$_{0.11}$Ga$_{0.89}$As		500	none	none
i In$_{0.12}$Ga$_{0.88}$As		35	none	none
i Al$_{0.11}$Ga$_{0.89}$As		20	none	none
i In$_{0.12}$Ga$_{0.88}$As	X 5	40	none	none
i Al$_{0.11}$Ga$_{0.92}$As		20	none	none
n In$_{0.25}$Ga$_{0.75}$As		55	Si	7×10^{17}
i Al$_{0.11}$Ga$_{0.89}$As		500	none	none
i GaAs		1000	none	none
n GaAs (bottom contact)		10000	Si	2×10^{18}
S.I. GaAs substrate		625 ± 25 μm	none	none

HS TC-QWIP
$In_{0.25}Ga_{0.75}As/Al_{0.11}Ga_{0.89}As/In_{0.12}Ga_{0.88}As$

(a)

(b)

Figure 2.1   (a) The schematic conduction band diagram and (b) the transmission coefficient of the high-strain TC-QWIP for LWIR detection.
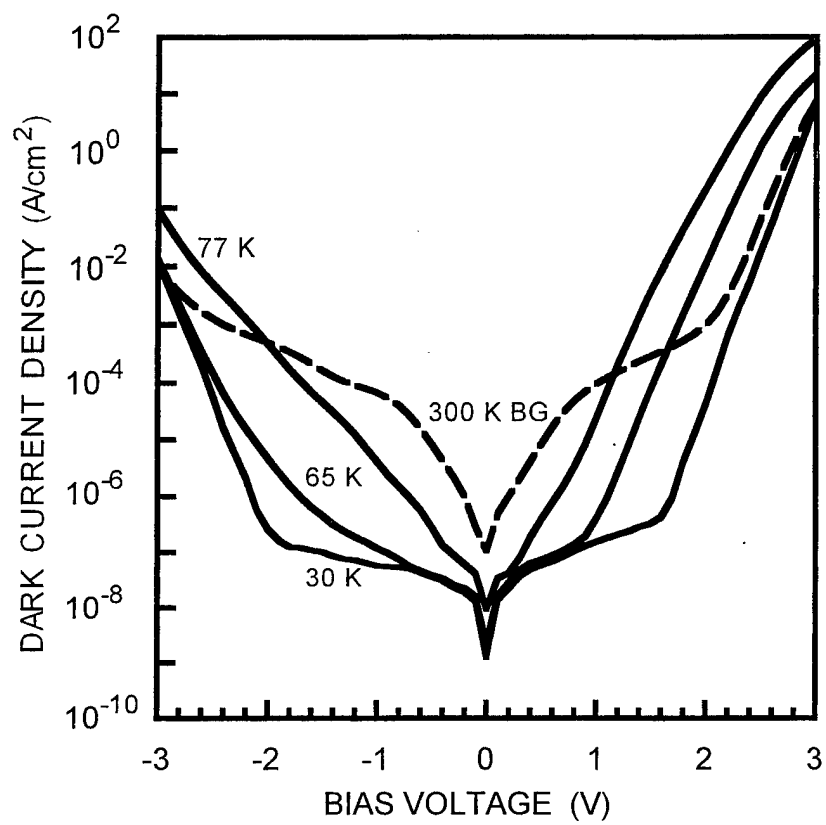
Figure 2.2 The dark *J-V* curves for the 5-period HS TC-QWIP.
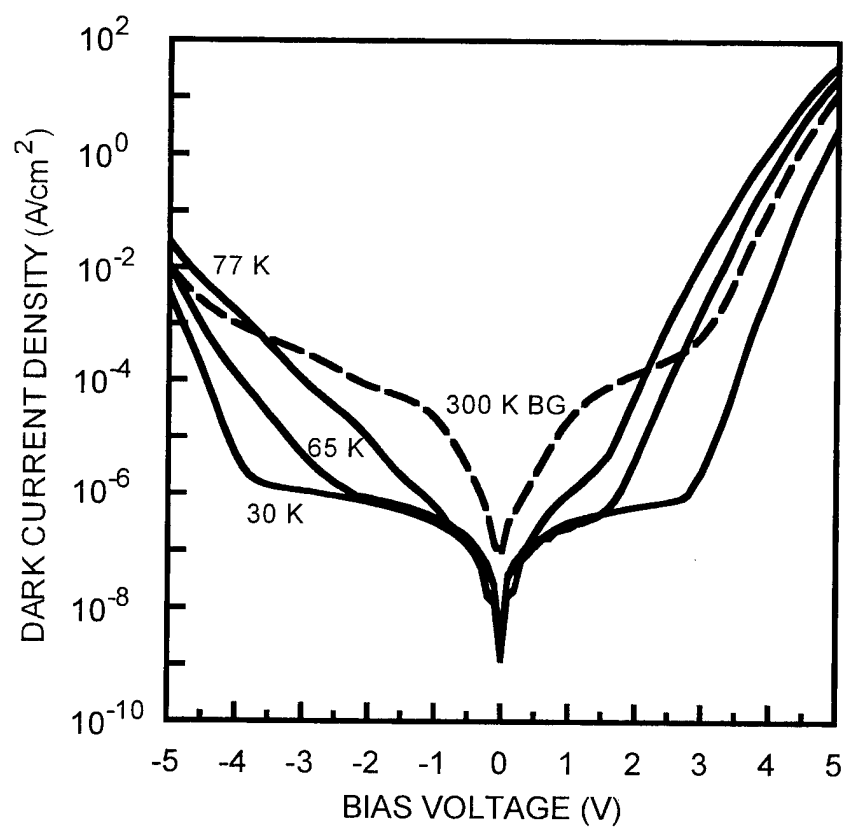
Figure 2.3 The dark *J-V* curves for the 10-period HS TC-QWIP.
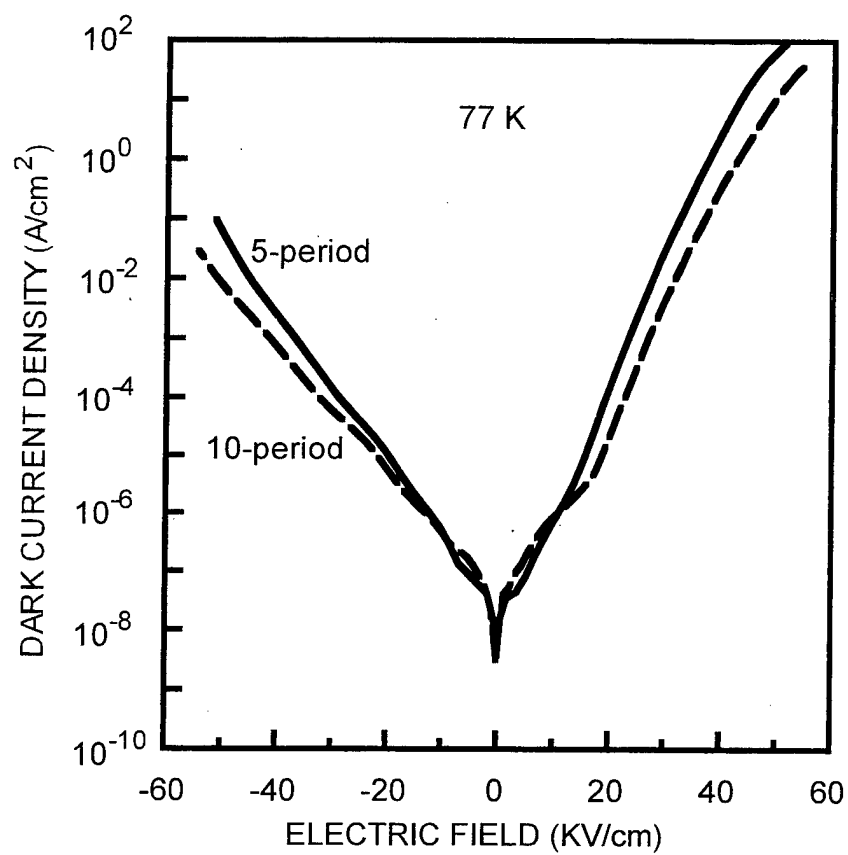
Figure 2.4 The dark current density versus electric field at 77 K for both the 5-period and 10-period HS TC-QWIPs.
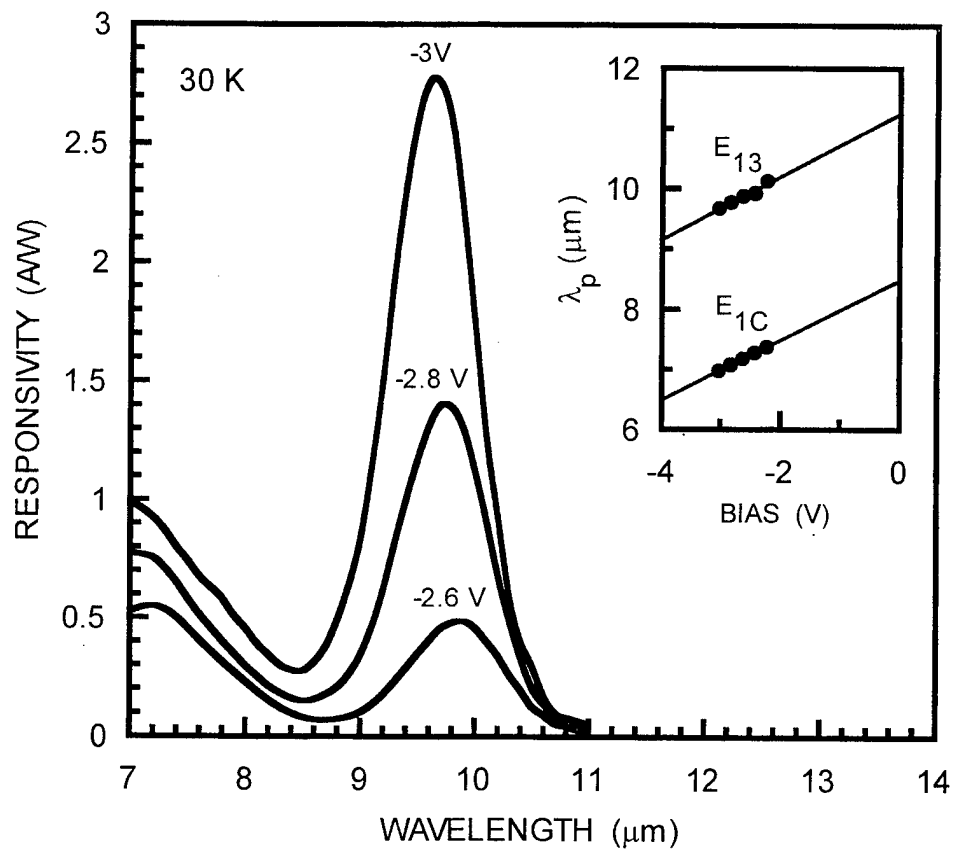
Figure 2.5 The spectral responsivities for the 5-period HS TC-QWIP with a 45° incidence measured at 30 K.
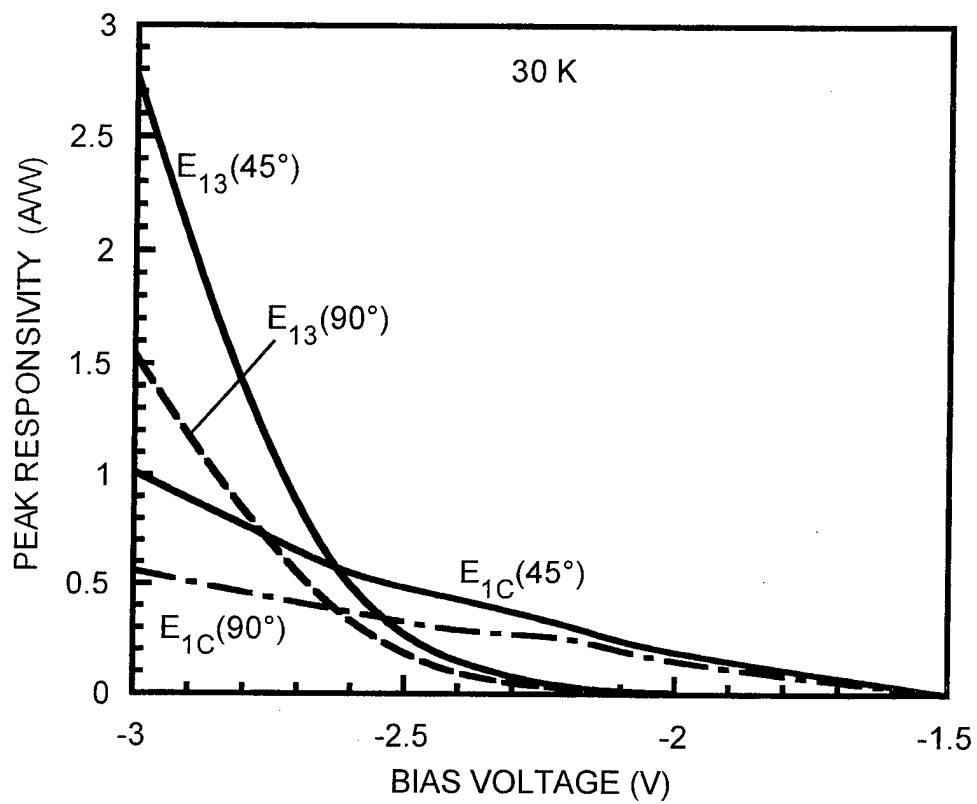
Figure 2.6 The peak responsivities versus bias for the 5-period HS TC-QWIP with 45°
incidence and normal incidence measured at 30 K.
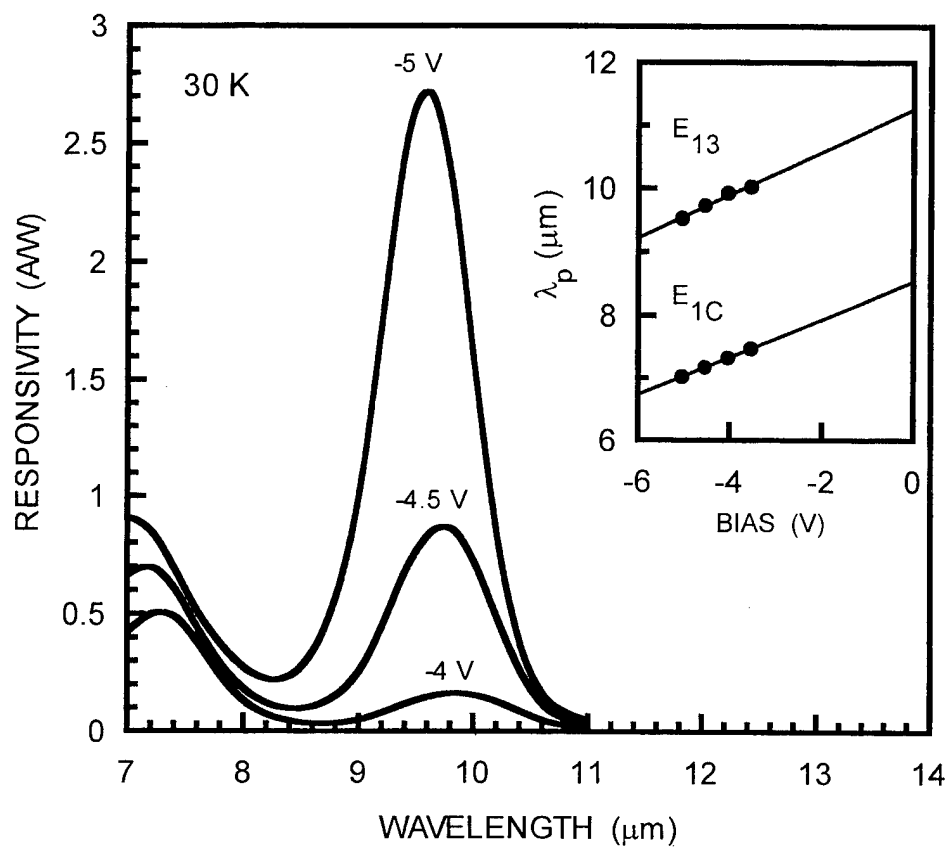
Figure 2.7 The spectral responsivities for the 10-period HS TC-QWIP with a 45° incidence measured at 30 K.
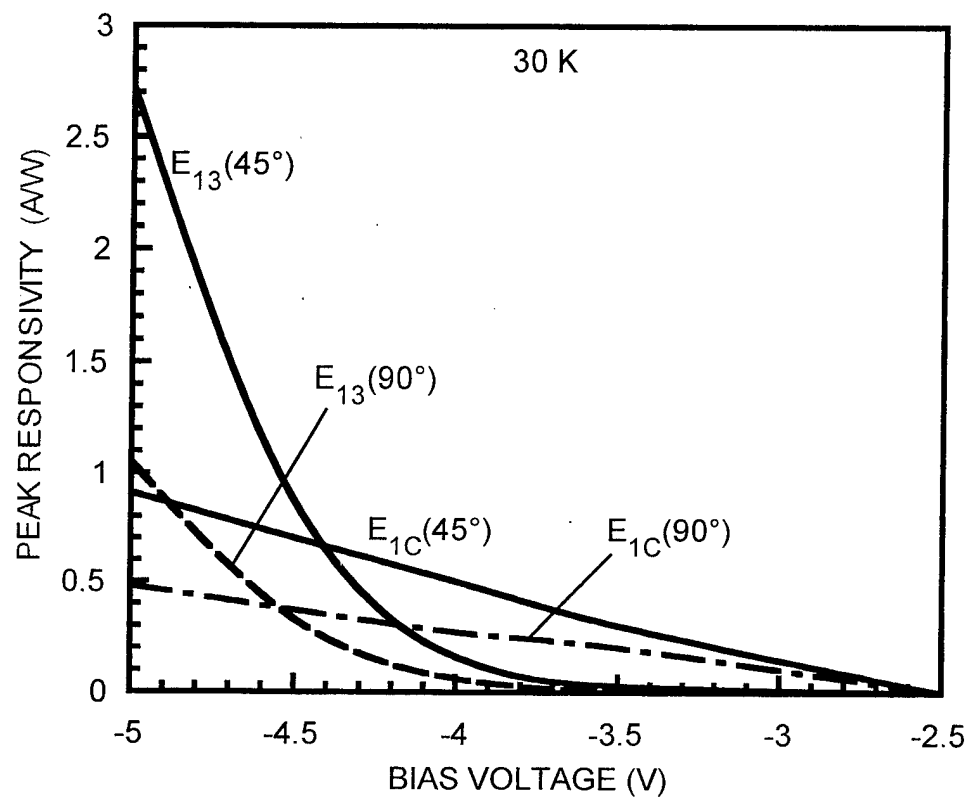
Figure 2.8 The peak responsivity versus bias for the 10-period HS TC-QWIP with 45°
incidence and normal incidence measured at 30 K.
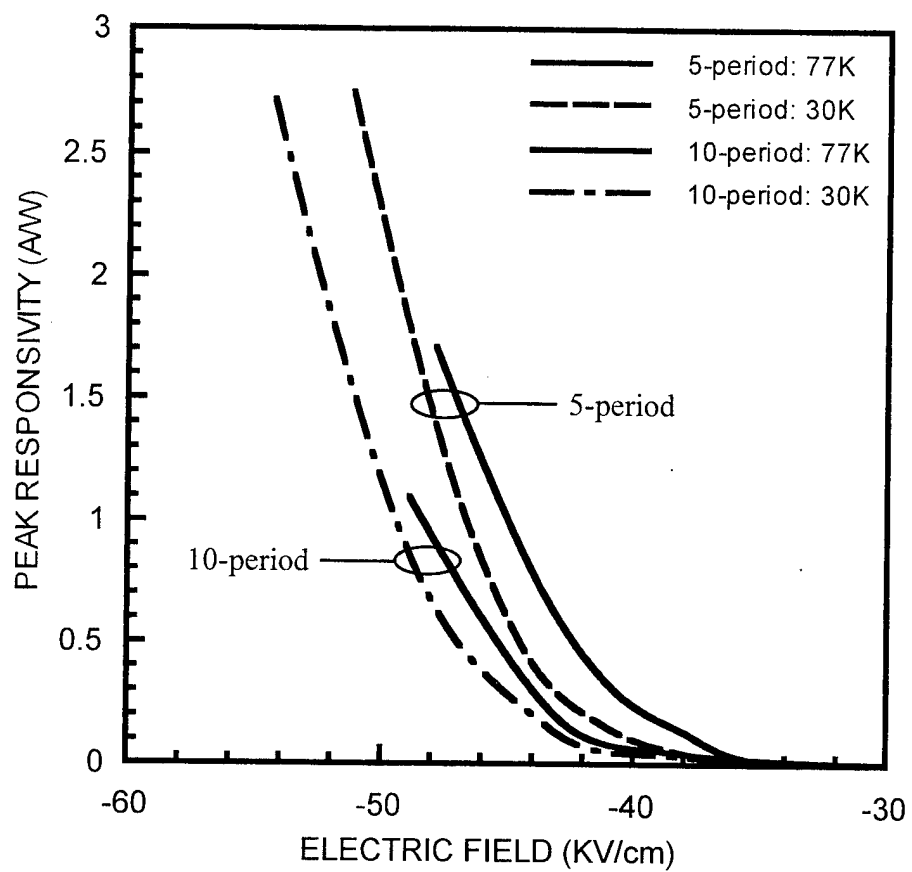
Figure 2.9 The temperature dependence of the peak responsivities for the $E_1 \rightarrow E_3$ transition versus electric field with a 45° incidence.
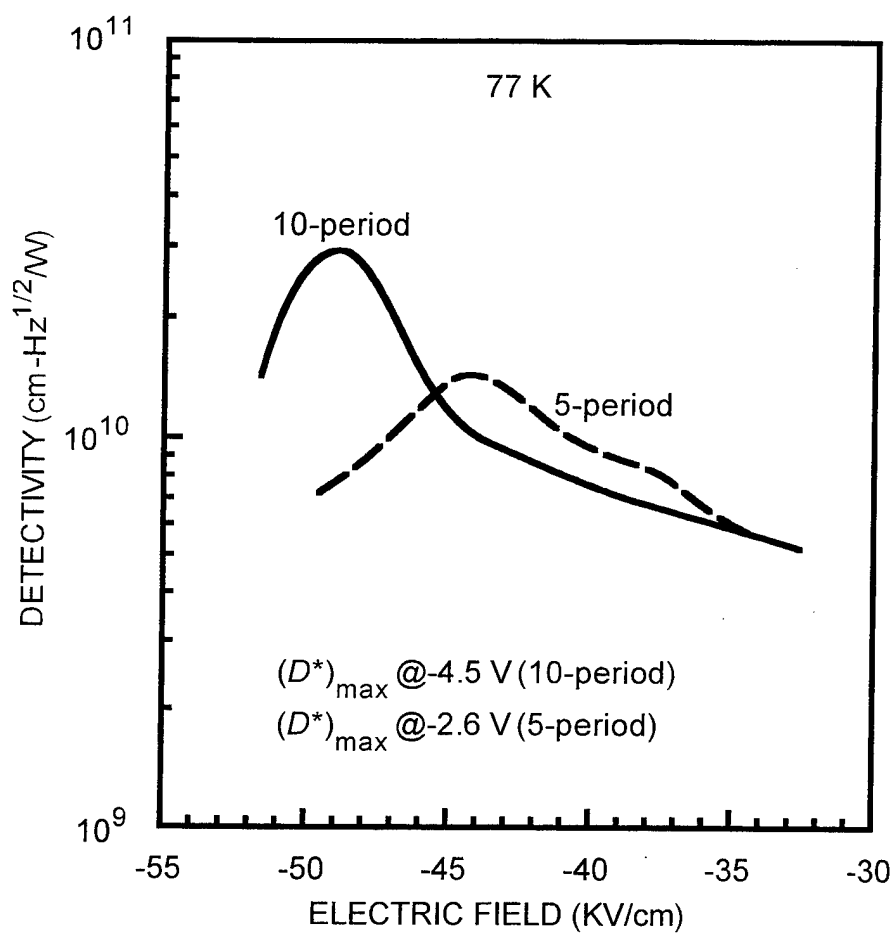
Figure 2.10 The peak detectivity versus electric field for the HS TC-QWIPs at 77 K.
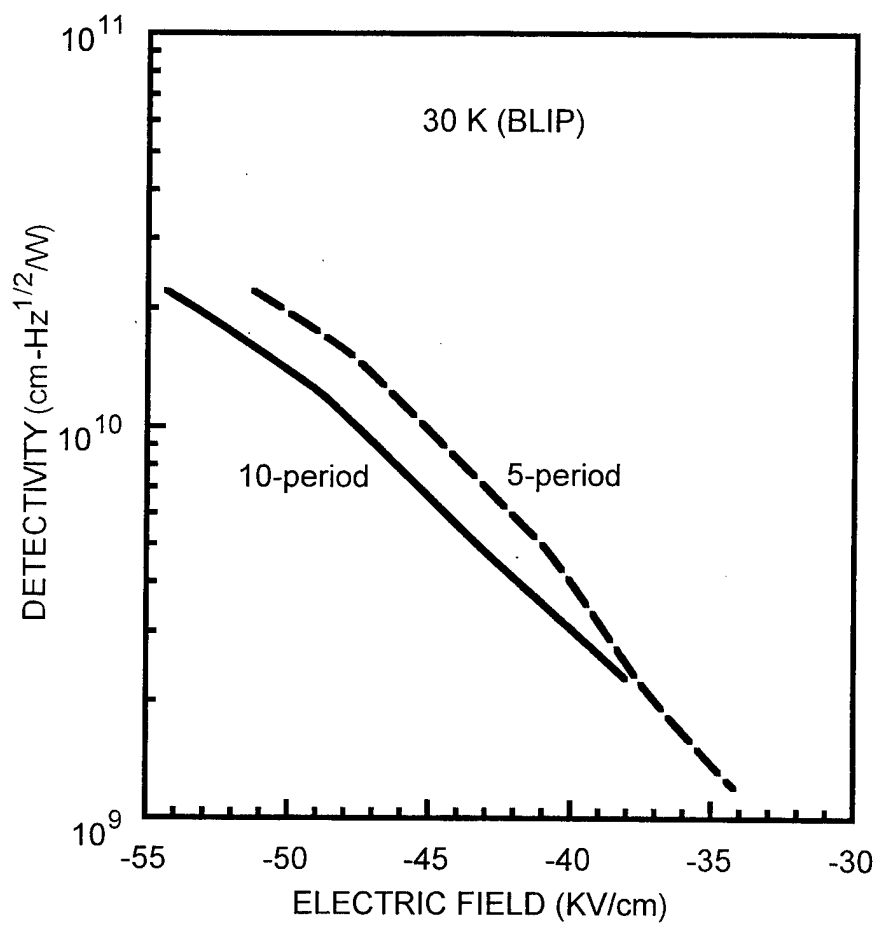
Figure 2.11 The BLIP detectivity versus electric field for the HS TC-QWIP at 30 K.

3 A THREE-STACK InGaAs/AlGaAs/InGaAs BROADBAND TRIPLE-COUPLED QUANTUM WELL INFRARED PHOTODETECTOR

3.1 Introduction

Multi-color quantum well infrared photodetectors (QWIPs) using different transition schemes and structures have been widely investigated recent year [10]. Theoretical studies of quantum-confined Stark effect in two- and three-coupled-quantum-well (TCQW) structures have been reported for voltage tunable infrared detection [11,12], and voltage-tunable multicolor triple-coupled QWIPs (TC-QWIPs) using InGaAs/GaAs/AlGaAs and high-strain (HS) InGaAs/AlGaAs/InGaAs material systems grown on GaAs for 8-12 μm long-wavelength detection have been demonstrated recently [8,13]. The high-strain InGaAs/AlGaAs/InGaAs TC-QWIP has shown excellent performance and wavelength tunability in the LWIR spectral range [8]. Most QWIP devices were developed with sensitivity in the 3-5 μm mid-wavelength infrared (MWIR) or 8-12 μm long-wavelength infrared (LWIR) region. The multi-color QWIPs were also investigated by using multi-stack quantum well structure for both the mid-wavelength and long-wavelength detection or voltage tuning of peak wavelength such as TC-QWIP, which usually has narrow bandwidth due to bound-to-bound state transition [8,13]. In order to broaden the detection bandwidth, the bound-to-miniband (BTM) QWIP [14] and asymmetrical quantum well structure with graded barrier [15] were proposed. Recently, several broadband (BB-) QWIPs have been demonstrated using three- or four-well structure in a unit cell that has different well widths and barrier heights by varying the barrier layer composition [16].

In this chapter, we report a high performance InGaAs/AlGaAs/InGaAs broadband triple-coupled quantum well infrared photodetector (BB TC-QWIP) for voltage tunable

multicolor detection in the 7-12 μm long-wavelength band. This BB TC-QWIP was formed by using three-stack structure without contact layers between the stacks.

3.2 Device Design and Fabrication

This BB TC-QWIP device was formed by using a three-stack structure without contact layers between the stacks. The device structure of each stack consists of an asymmetrical triple coupled quantum wells (TCQWs) with one deep $In_{0.25}Ga_{0.75}As$ quantum well Si-doped to $N_d = 7.0 \times 10^{17}$ cm^{-3} and two undoped $In_{0.12}Ga_{0.88}As$ shallow quantum wells separated by two 2 nm thin inner barriers ($Al_xGa_{1-x}As$) between the 50 nm thick barriers ($Al_xGa_{1-x}As$). Each TC-QWIP stack has different quantum well widths, periods, and barrier heights by varying Al composition so that each stack has different peak detection wavelengths. The different periods were used to evenly distribute the bias voltage drop across each stack, which are 3 periods for the bottom stack, 5 periods for the middle stack, and 6 periods for the top stack, respectively. The quantum well widths and barrier material of the TC-QWIP stacks are given as 5.5/4/3.5 nm and $Al_{0.11}Ga_{0.89}As$ for the bottom stack, 5.5/4/4 nm and $Al_{0.08}Ga_{0.92}As$ for the middle stack, and 5/4/4 nm and $Al_{0.06}Ga_{0.94}As$ for the top stack, respectively. Two 0.1 μm thick undoped GaAs layers were grown on both sides of this TC-QWIP to reduce the dark current. Finally, the TC-QWIP surrounded by the top and bottom ohmic contact layers (Si-doped to $n = 2.0 \times 10^{18}$ cm^{-3}) was grown on the semi-insulating GaAs substrate. Table 3.1 shows the layer structure of the stacked TC-QWIP. A mesa structure with 216 x 216 μm^2 active area was fabricated to characterize the device performance by using standard wet chemical etching. AuGe/Ni/Au was evaporated on the top and bottom of the mesa structure for ohmic contacts. The 45° polished facet was processed for the back-illumination and IR radiation coupling. The device was mounted at the edge of the hole on the 16-pin TO-8 socket. The

23

silver-filled epoxy with low thermal resistance was used to bond the device onto the package.

3.3 Results and Discussion

Figure 3.1 shows the schematic conduction band diagram and the calculated intersubband transition energy levels of this stacked TC-QWIP at zero bias voltage. Each TC-QWIP stack can detect specific peak wavelength and then the whole three-stack TC-QWIP structure can cover the broad wavelength range by overlapping the detection wavelength of each stack. The $E_1 \rightarrow E_c$ bound-to-continuum (BTC) transition was mainly detected at lower bias voltages while both $E_1 \rightarrow E_c$ and $E_1 \rightarrow E_3$ bound-to-bound (BTB) transitions were observed at higher bias voltages.

Figure 3.2 shows the dark current versus bias voltage (I-V) measured at T = 40, 52, 60, and 77 K with a 180° field of view (FOV) 300 K background photocurrent of the device. The dark current curves show the asymmetric behavior due to the asymmetric layer structure and the normal feature of n-type QWIPs. The device is under background limited perfromance (BLIP) between -5.5V and 4.2V at T = 40 K, and between -1.8V and 1.2V at T = 77 K.

The photo response was measured at T = 40 and 77 K by using an 1/8 monochromator and blackbody light source (T = 1273 K) at a chopped frequency (200 Hz). Figure 3.3 shows the spectral responsivity of the TC-QWIP at T = 40 K, (a) lower bias, and (b) higher bias voltages. The applied bias voltage was first distributed across the bottom TC-QWIP because of the highest resistance by the highest barrier. When the applied bias voltage was further increased the middle stack and the top stack can be biased one after another. As clearly shown in Fig. 3.3, only $E_1 \rightarrow E_c$ transitions of the bottom and middle stacks were observed at lower bias voltages ($V_b \leq$ -3.75V). The $E_1 \rightarrow E_c$ transition of the

24

top stack can also be observed with the increasing bias voltage ($V_b \geq -4V$). The peak responsivity and full-width half-maximum (FWHM) at $\lambda_p = 8.7$ μm and $V_b = -3.75V$ was 0.48 A/W and $\Delta\lambda/\lambda_p = 21$ %, respectively. When a higher bias voltage ($V_b \geq -4V$) was applied to the device, the thick AlGaAs barrier was tilted to the thin triangle barrier so that the $E_1 \rightarrow E_3$ transitions can be detected by the tunneling through E_3 bound state. At the bias voltage of -4.5V, the spectral responsivities at $\lambda_{p1} = 8.4$ μm and $\lambda_{p2} = 10.8$ μm were almost the same (0.82 A/W and 0.81 A/W, respectively). Therefore, a very broad responsivity curve was achieved with $\Delta\lambda/\lambda_{p1} = 21$ % and $\Delta\lambda/\lambda_{p2} = 20$ % for this stacked TC-QWIP. It is noted that this $\Delta\lambda/\lambda_{p2} = 20$ % is much broader than that of the one stack high-strain TC-QWIP ($\Delta\lambda/\lambda_p = 10$ %). The $E_1 \rightarrow E_3$ transition becomes the dominant response peak at $V_b = -4.75V$. In particular, the peak spectral responsivity at $\lambda_p = 10.6$ μm and $V_b = -5.2V$, which was primarily due to the $E_1 \rightarrow E_3$ transition of the bottom stack, was found to be 2.75 A/W. The tunable wavelength for $E_1 \rightarrow E_3$ transition was 10.6-10.8 μm between -5.2V and -4.75V. Figure 3.4 shows the measured and the calculated 300K background window current I-V curves with 180° field of view (FOV), which was in good agreement with each other. Figure 3.5 shows the spectral responsivity of the BB TC-QWIP measured at T = 77 K and different bias voltages. The peak responsivity at T = 77 K and $V_b = -4.25V$ was 0.62 A/W at $\lambda_p = 10.3$ μm. The T = 40 K and 77 K spectral responsivity curves were different at the same bias voltage. For example, the $E_1 \rightarrow E_3$ transition at $V_b = -4.25V$ and T = 77 K was more dominant than that at T = 40 K, that is, the spectral responsivity by $E_1 \rightarrow E_3$ transition was larger than that of $E_1 \rightarrow E_c$ transition at T = 77 K, but this was reversed at T = 40 K, which was attributed to the more

dominant thermionic-assisted tunneling (TAT) conduction through E_3 bound state at higher temperature.

We have calculated the detectivity for the BB TC-QWIP at T = 40 K and 77 K by using our noise model. The background limited performance (BLIP) detectivity (D^*_{BLIP}) at λ_p = 10.6 μm was found to be 1.98 x 10^{10} cm-Hz$^{1/2}$/W at T = 40 K and V_b = -5.2V. The peak detectivity (D^*) under non-BLIP condition was 5.54 x 10^9 cm-Hz$^{1/2}$/W at T = 77 K, λ_p = 10.3 μm, and V_b = -4.25V.

3.4 Conclusions

We have fabricated and characterized a new InGaAs/AlGaAs/InGaAs broadband triple-coupled quantum well infrared photodetector (BB TC-QWIP) for 8-14 μm long-wavelength detection. In order to detect the broad wavelength range, the three-stack structure that has three different peak wavelength was created as a three-color QWIP. The $E_1 \rightarrow E_c$ transition was obtained at lower bias voltages (V_b < -3.75V) and both $E_1 \rightarrow E_3$ and $E_1 \rightarrow E_c$ transitions were detected simultaneously at higher bias voltages ($V_b \geq$ -4V). The broader wavelength range can be detected by modifying the layer structure. The positive temperature dependence of the responsivity was found from the measured results at T = 40 K and 77 K.

Table 3.1 The layer structure of the BB TC-QWIP.

Layer		Thickness (Å)	Dopant	Concentration (cm^{-3})
n GaAs (top contact)		5000	Si	2×10^{18}
i GaAs		1000	none	none
i Al$_{0.06}$Ga$_{0.94}$As		500	none	none
i In$_{0.12}$Ga$_{0.88}$As		40	none	none
i Al$_{0.06}$Ga$_{0.94}$As		20	none	none
i In$_{0.12}$Ga$_{0.88}$As	X 6	40	none	none
i Al$_{0.06}$Ga$_{0.94}$As		20	none	none
n In$_{0.25}$Ga$_{0.75}$As		50	Si	7×10^{17}
i Al$_{0.06}$Ga$_{0.94}$As		500	none	none
i In$_{0.12}$Ga$_{0.88}$As		40	none	none
i Al$_{0.08}$Ga$_{0.92}$As		20	none	none
i In$_{0.12}$Ga$_{0.88}$As	X 5	40	none	none
i Al$_{0.08}$Ga$_{0.92}$As		20	none	none
n In$_{0.25}$Ga$_{0.75}$As		55	Si	7×10^{17}
i Al$_{0.08}$Ga$_{0.92}$As		500	none	none
i In$_{0.12}$Ga$_{0.88}$As		35	none	none
i Al$_{0.11}$Ga$_{0.89}$As		20	none	none
i In$_{0.12}$Ga$_{0.88}$As	X 3	40	none	none
i Al$_{0.11}$Ga$_{0.89}$As		20	none	none
n In$_{0.25}$Ga$_{0.75}$As		55	Si	7×10^{17}
i Al$_{0.11}$Ga$_{0.89}$As		500	none	none
i GaAs		1000	none	none
n GaAs (bottom contact)		10000	Si	2×10^{18}
S.I. GaAs substrate		625 ± 25 μm	none	none

Bottom stack ($In_{0.25}Ga_{0.75}As/Al_{0.11}Ga_{0.89}As/ In_{0.12}Ga_{0.88}As$)
Middle stack ($In_{0.25}Ga_{0.75}As/Al_{0.08}Ga_{0.92}As/ In_{0.12}Ga_{0.88}As$)
Top stack   ($In_{0.25}Ga_{0.75}As/Al_{0.06}Ga_{0.94}As/ In_{0.12}Ga_{0.88}As$)

< intersubband transition energy at zero bias voltage >
Bottom stack : $E_1 - E_c$ (140 meV), $E_1 - E_3$ (114 meV)
Middle stack : $E_1 - E_c$ (123 meV), $E_1 - E_3$ (104 meV)
Top stack   : $E_1 - E_c$ (106 meV), $E_1 - E_3$ (98 meV)

Figure 3.1   The schematic conduction band diagram and the intersubband transition energy of the BB TC-QWIP.
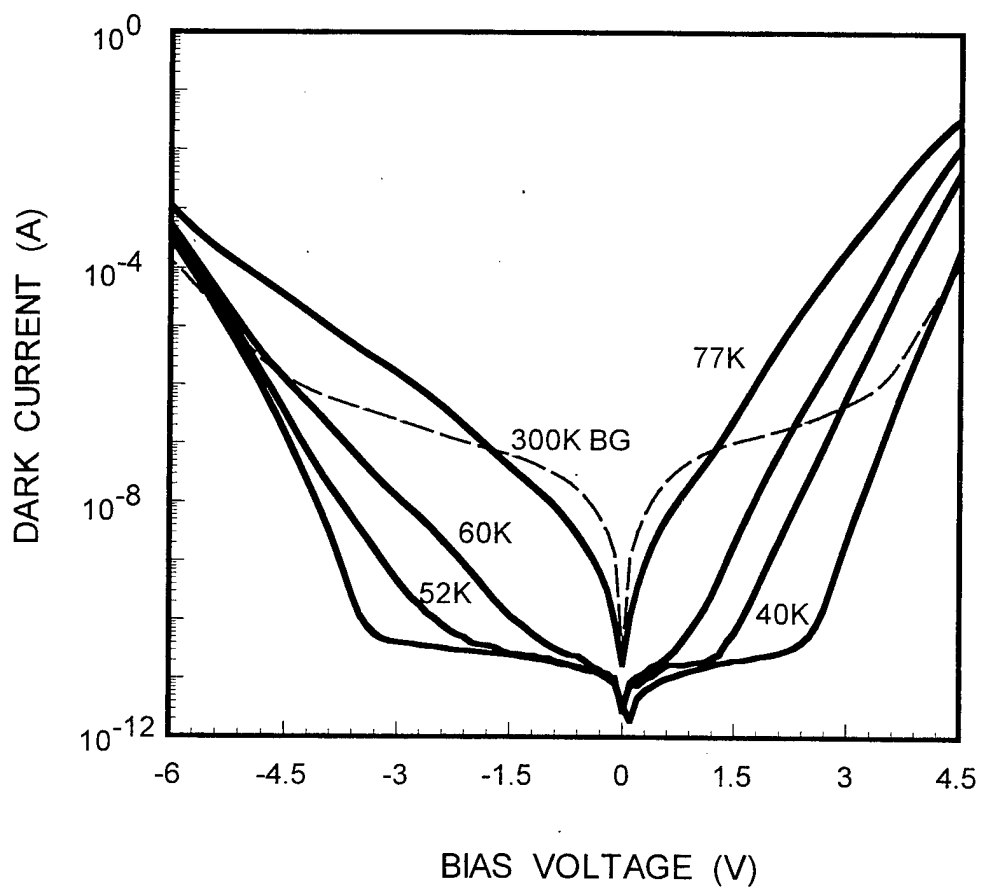
Figure 3.2 The dark current versus bias voltage (I-V) measured at T = 40, 52, 60 and 77K with the 180° field of view (FOV) 300K background window current of the BB TC-QWIP.
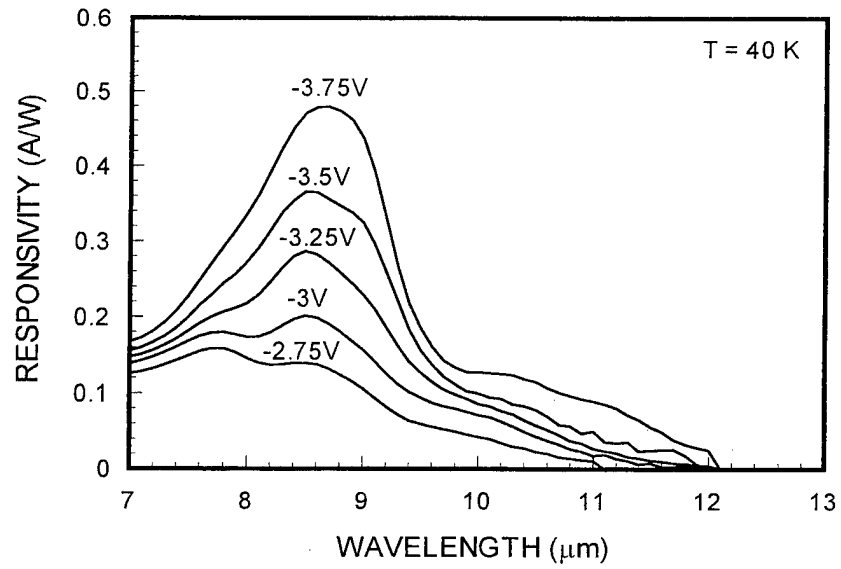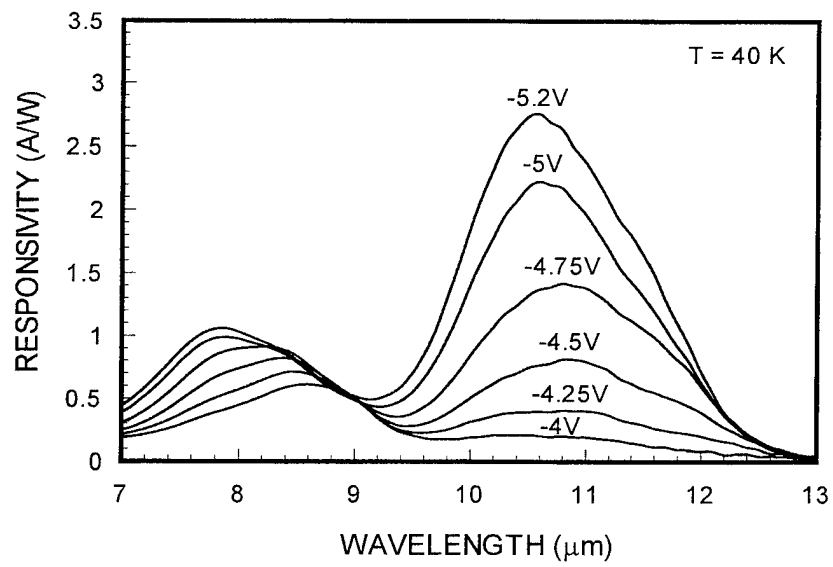
Figure 3.3 The spectral responsivity of the BB TC-QWIP measured at T = 40K, (a) lower bias voltage, and (b) higher bias voltage.
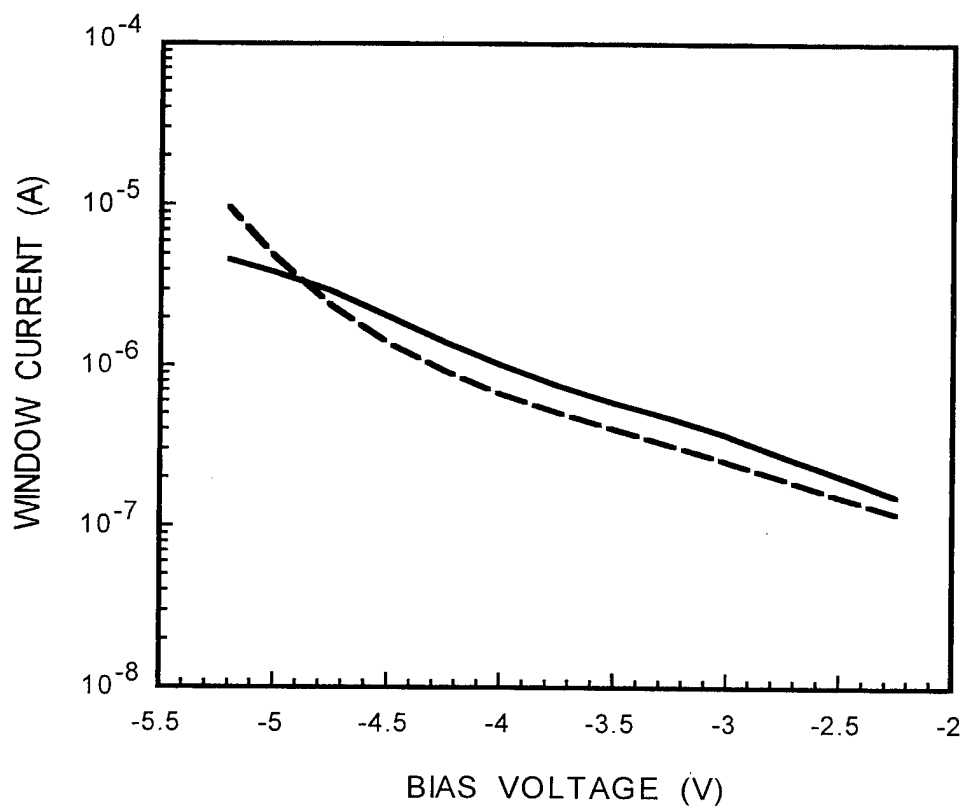
Figure 3.4 The 300K background window current with 180° field of view (FOV) of the BB TC-QWIP: the solid line (calculated) and the dashed line (measured).
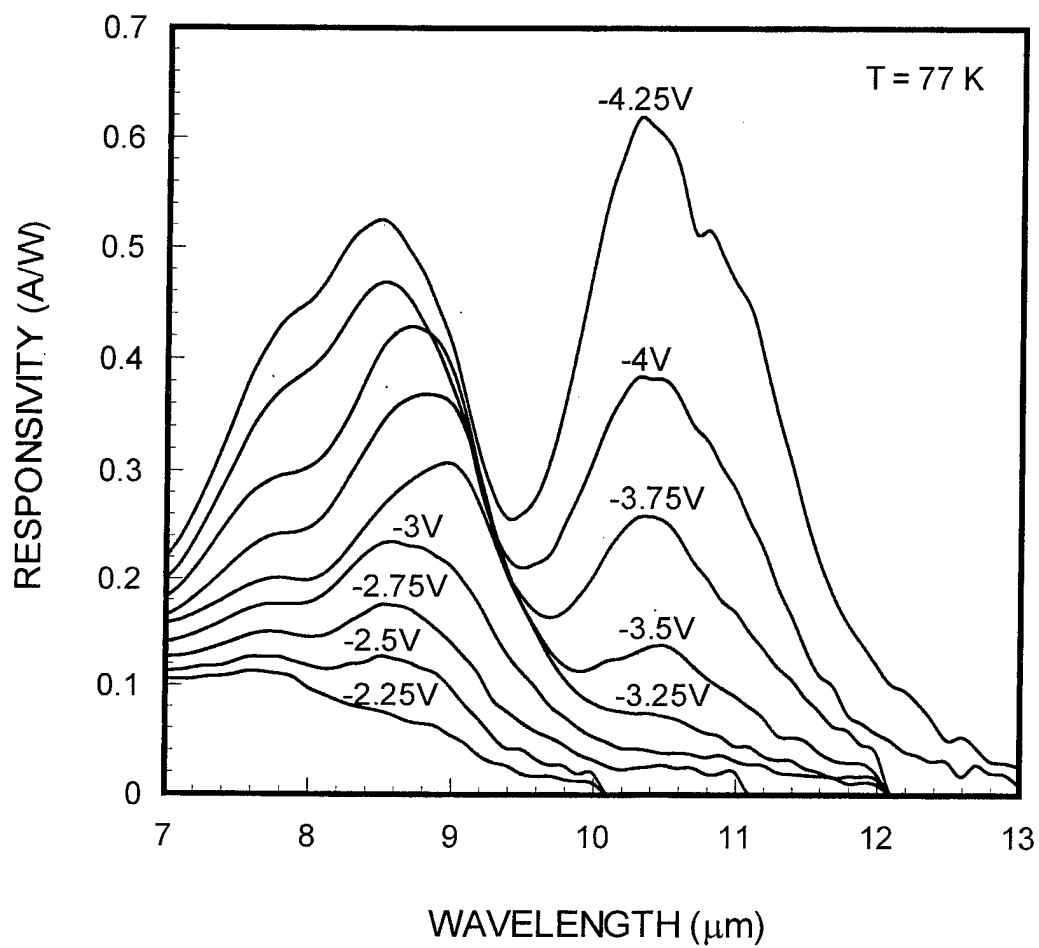
Figure 3.5 The spectral responsivity of the BB TC-QWIP measured at T = 77K.

4 A In$_{0.45}$Ga$_{0.55}$As/ In$_{0.45}$Ga$_{0.55}$As/ In$_{0.45}$Ga$_{0.55}$As TRIPLE-COUPLED QUANTUM WELL INFRARED PHOTODETECTOR FOR MWIR DETECTION

4.1 Introduction

The performance of the quantum well infrared photodetectors (QWIPs) have been enhanced by various intersubband transition schemes and material systems with the maturity of the molecular beam epitaxy (MBE) technology [10]. Different intersubband transition schemes such as bound-to-bound (BTB), bound-to-quasi-bound (BTQB), bound-to-miniband (BTM), and bound-to-continuum (BTC) can be chosen to improve the device performance. For example, the BTC transition can contribute to more sensitive QWIP by aligning the final state above the barrier and the BTQB transition mechanism can reduce the dark current because the dark current due to thermionic emission is exponentially decreased with the increasing barrier height. The asymmetrical QWIP structures such as the step well, the linear graded barrier, and the coupled quantum well can affect the device performance and detection wavelength due to the voltage tunable wavelength shift for multicolor detection and the broadband detection on bias polarity. Theoretical studies of the double- and the triple-coupled quantum well structures have been reported [11,12]. The strong quantum Stark shift by the applied bias is predicted in the triple- coupled quantum well (TCQW) structure for long wavelength infrared detection. Recently, the triple-coupled quantum well infrared photodetectors (TC-QWIPs) [8,13] using AlGaAs/InGaAs material systems grown on S.I. GaAs substrate have been demonstrated for 7-14 μm long-wavelength infrared (LWIR) detection in which a large voltage tunable wavelength shift and high responsivity were obtained. In addition to GaAs/AlGaAs, InGaAs/GaAs, and InGaAs/AlGaAs material systems grown on GaAs

substrate, $In_{0.53}Ga_{0.47}As/In_{0.52}Al_{0.48}As$ lattice-matched QWIP structures grown on InP substrate [13,17,18] have been extensively studied, which allows the shorter wavelength detection due to the large conduction band offset. The short- and mid-wavelength infrared regions are of important for imaging and communication applications [19-25]. In this chapter, we present a new mid-wavelength infrared triple-coupled quantum well infrared photodetector (MWIR TC-QWIP) using $In_{0.53}Ga_{0.47}As/In_{0.52}Al_{0.48}As/\ In_{0.3}Ga_{0.7}As$ material systems grown on InP substrate for 3-5 μm detection.

4.2 Device Design and Fabrication

The basic device structure of the MWIR TC-QWIP consists of a 4 nm $In_{0.45}Ga_{0.55}As$ quantum well Si-doped to $N_d = 2.5 \times 10^{18}$ cm^{-3} and two undoped 2.5 and 2 nm shallow $In_{0.3}Ga_{0.7}As$ quantum wells separated by two 1.2 nm thin $In_{0.52}Al_{0.48}As$ inner barriers, which were sandwiched by the 30 nm thick $In_{0.52}Al_{0.48}As$ barriers to form the unit cell. Ten periods of the unit cell were grown to form the absorber layer. Finally, InGaAs contact layers (Si-doped to 2.0×10^{18} cm^{-3}) on both the top and bottom of the 10- period QWIP structure were grown on the semi-insulating InP substrate. Table 3.1 shows the layer structure of this MWIR TC-QWIP. Figure 4.1 shows the schematic conduction band diagram and the intersubband transition schemes (a) at zero and (b) negative bias voltages. The first (E_2) and second (E_3) excited states were aligned due to the strong asymmetrical coupling effect of the three $In_xGa_{1-x}As$ quantum wells and two thin $In_{0.52}Al_{0.48}As$ inner barriers. As clearly shown in Figure 4.1(b), the thick $In_{0.52}Al_{0.48}As$ barrier turns into the thin triangle barrier at higher bias voltages so that the E_1-E_3

transition can be detected by tunneling mechanism of the photo-excited electrons through the E_3 excited state.

The test mesa structure with an active area of 216 x 216 μm^2 was created to characterize the device performance through the top contact layer and device active region down to the bottom contact layer by standard wet chemical etching using $1H_3PO_4:1H_2O_2:8H_2O$ chemical solution. AuGe/Ni/Au was evaporated to 50 x 50 μm^2 area on the mesa structure for the top ohmic contact and around the periphery of the mesa structures for the bottom contact. The test device was annealed at T = 450° C for two minutes after E-beam evaporation. The 45° facet was polished on the InP substrate for back-illumination IR radiation coupling. The silver-filled epoxy cement was used to attach the device to a package, which provides a low thermal resistance between the device and the package. The device can be mounted on a round TO-type package with 16 pins, which is one of the earliest IC packages. The ultrasonic wire- bonding through a combination of pressure and rapid mechanical vibration was used with gold wires for making electrical connection between the device and the package.

4.3 Results and Discussion

Figure 4.2 shows the dark current versus bias voltage (I-V) curves measured at T = 77, 97, and 116K with a 180° field of view (FOV) 300K background photocurrent of MWIR TC-QWIP. The device is under background limited performance (BLIP) when the applied bias voltage is between -4.8V and 3.3V at T = 77K while the device is background limited between -2V and 0.8V at T = 116K.

The photocurrent was measured at T = 77 and 116K by using 1/8 monochromator and blackbody light source (T = 1273°K) at 200 Hz chopped frequency. The photocurrent from the device was amplified by transimpedance amplifier (TIA) with 10^6 V/A gain and measured using lock-in-amplifier. The spectral responsivity can be calculated using input power measured by pyroelectric detector. Figure 4.3 and 4.4 show the spectral responsivity of MWIR TC-QWIP at different temperatures and bias voltages. Only bound-to-continuum (BTC) transitions were observed at positive and lower negative bias voltages ($V_b < -3.5V$ at T = 77 and 116K). The bound-to-bound (BTB) transitions were enabled at higher negative bias voltages ($V_b > -4V$ at T = 77 and 116K). Moreover, the BTB transition was dominant at biases higher than $V_b = -4.5V$. The peak spectral responsivity for this MWIR TC-QWIP was 0.31 A/W at $\lambda_p = 4.6$ μm, $V_b = -5.5V$, and T = 77K. The BTB transitions at a fixed bias voltage and different temperatures for the MWIR TC-QWIP were much less sensitive to the temperature increase because of the very high barrier height as shown in Figure 4.3 and 4.4. The background limited performance (BLIP) detectivity (D^*_{BLIP}) at $\lambda_p = 4.6$ μm was found to be 2.65 x 10^{10} cm-$Hz^{1/2}$/W at T = 77K and $V_b = -4.5V$. The peak detectivity (D^*) under non-BLIP condition was 1.44 x 10^{10} cm-$Hz^{1/2}$/W at T = 116K, $\lambda_p = 4.6$ μm, and $V_b = -4V$.

4.4 Conclusions

We have demonstrated a new $In_{0.45}Ga_{0.55}As/In_{0.52}Al_{0.48}As/In_{0.3}Ga_{0.7}As$ mid-wavelength infrared triple-coupled quantum well infrared photodetector (MWIR TC-QWIP) grown on the InP substrate. This device can be operated up to T = 116K and the spectral responsivity was almost independent of the temperature. The BTC transition was

observed under both the negative and positive bias voltage conditions, while the BTB transition was detected at higher negative bias voltages. The responsivity due to BTB transition was found to increase dramatically with increasing bias voltage. It is noted that this device has better performance under negative bias voltages because both the BTB and BTC transitions can be detected with higher responsivity and lower dark current.

Table 4.1 The layer structure of the MWIR TC-QWIP grown on the InP substrate.

Layer		Thickness (Å)	Dopant	Concentration (cm^{-3})
n In$_{0.53}$Ga$_{0.47}$As		10000	Si	2x10^{18}
i In$_{0.52}$Al$_{0.48}$As		300	none	none
i In$_{0.3}$Ga$_{0.7}$As	X 10	20	none	none
i In$_{0.52}$Al$_{0.48}$As		12	none	none
i In$_{0.3}$Ga$_{0.7}$As		25	none	none
i In$_{0.52}$Al$_{0.48}$As		12	none	none
n In$_{0.45}$Ga$_{0.55}$As		40	Si	2.5x10^{18}
i In$_{0.52}$Al$_{0.48}$As		300	none	none
n In$_{0.53}$Ga$_{0.47}$As		10000	Si	2x10^{18}
S.I. InP substrate		625 $\pm$ 25 µm	none	none

$$(In_{0.45}Ga_{0.55}As/In_{0.52}Al_{0.48}As/In_{0.3}Ga_{0.7}As)$$
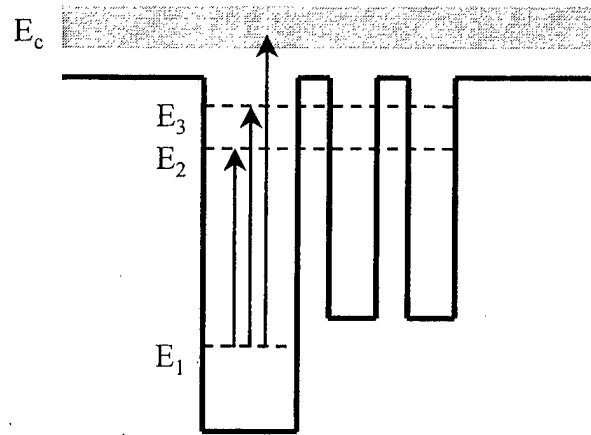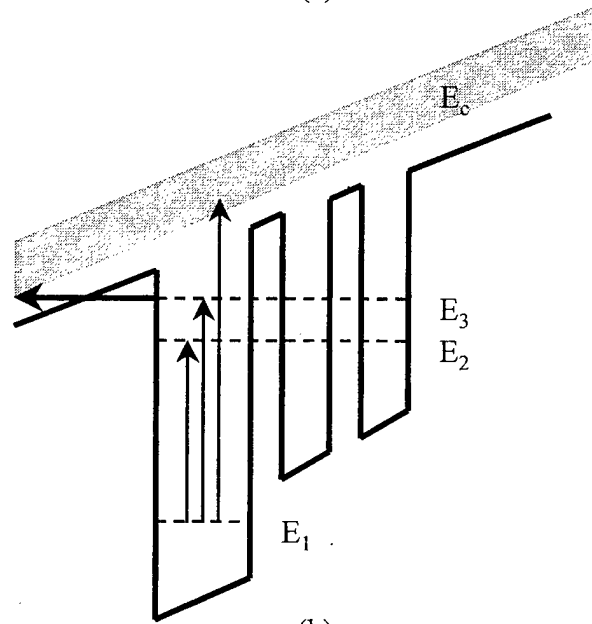
Intersubband transition energy at zero bias voltage: E_1-E_c (335 meV), E_1-E_3 (270 meV)

Figure 4.1 The schematic conduction band diagram and the bound state energy of the MWIR TC-QWIP grown on the InP substrate under a) zero bias voltage and (b) negative bias conditions.
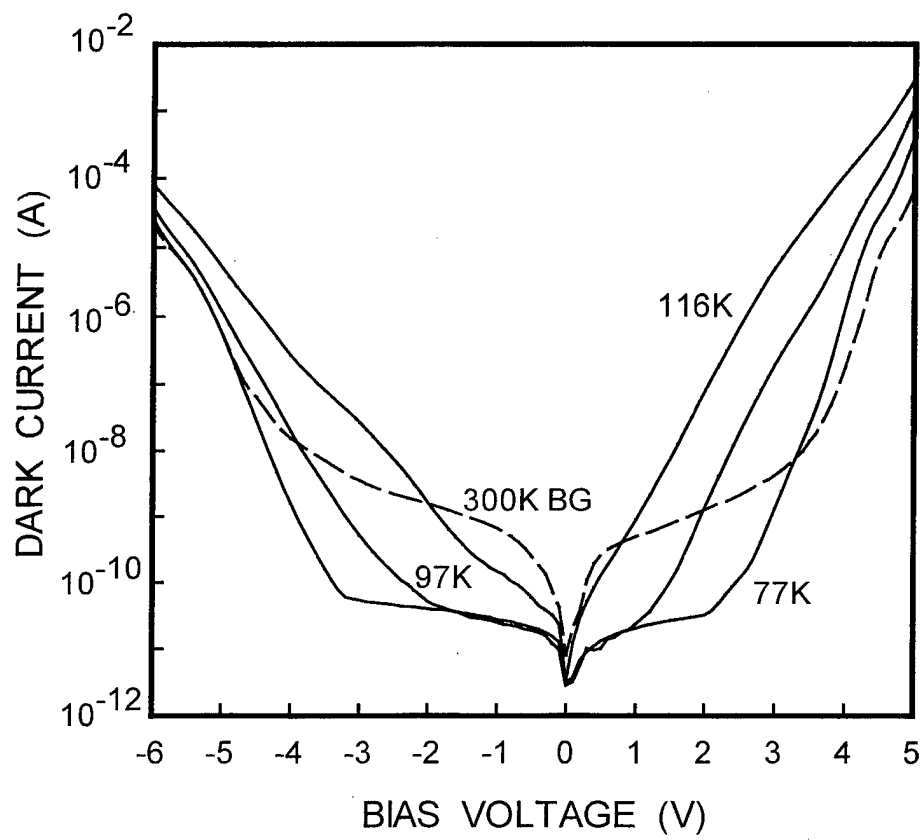
Figure 4.2 The dark current versus bias voltage (I-V) curves measured at T = 77, 97, and 116K along with the 180° field of view (FOV) 300K background photocurrent of the MWIR TC-QWIP grown on the InP substrate.
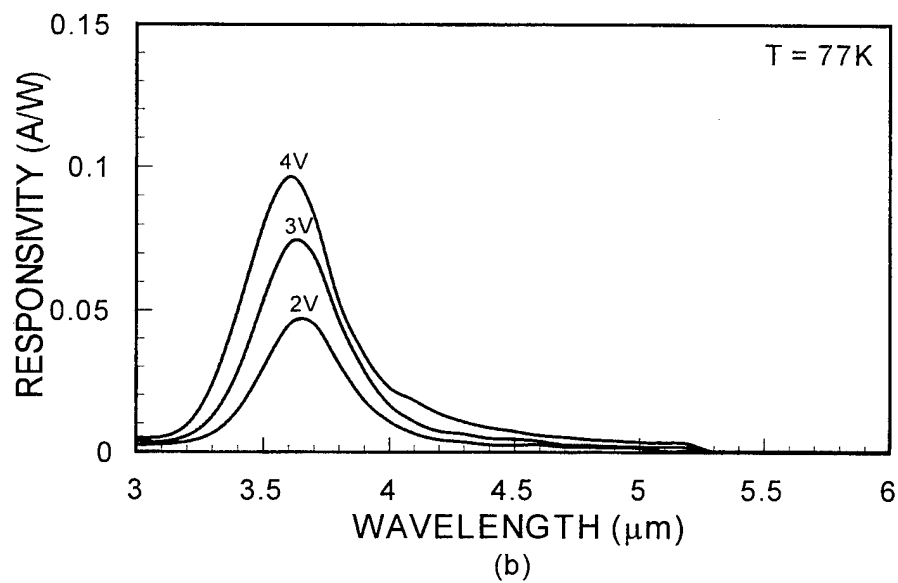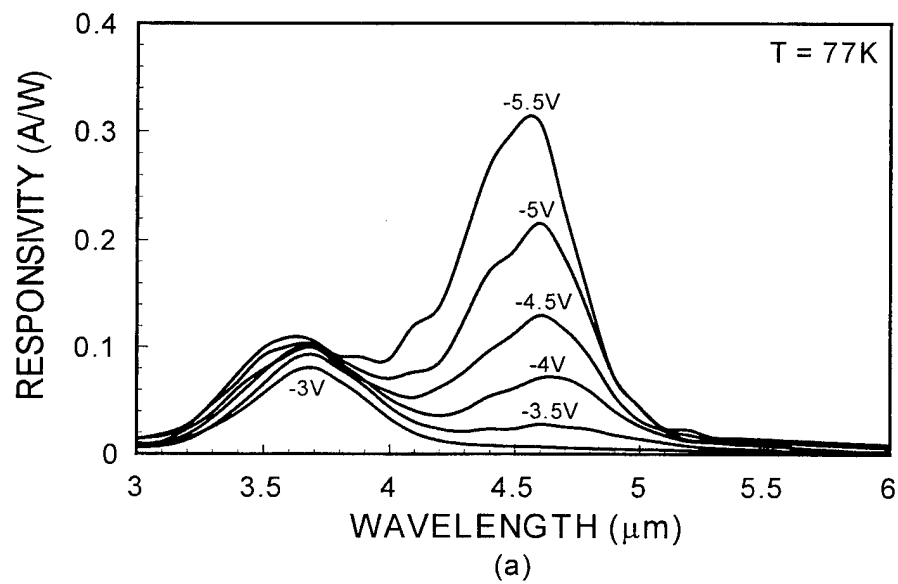
Figure 4.3 The spectral responsivity of the MWIR TC-QWIP grown on the InP substrate measured at T = 77K, under (a) negative bias and (b) positive bias conditions.
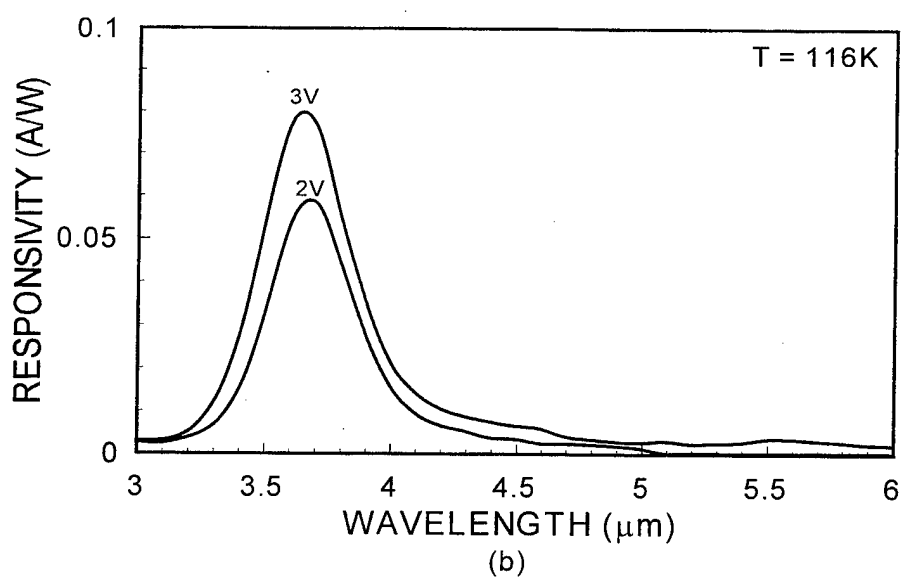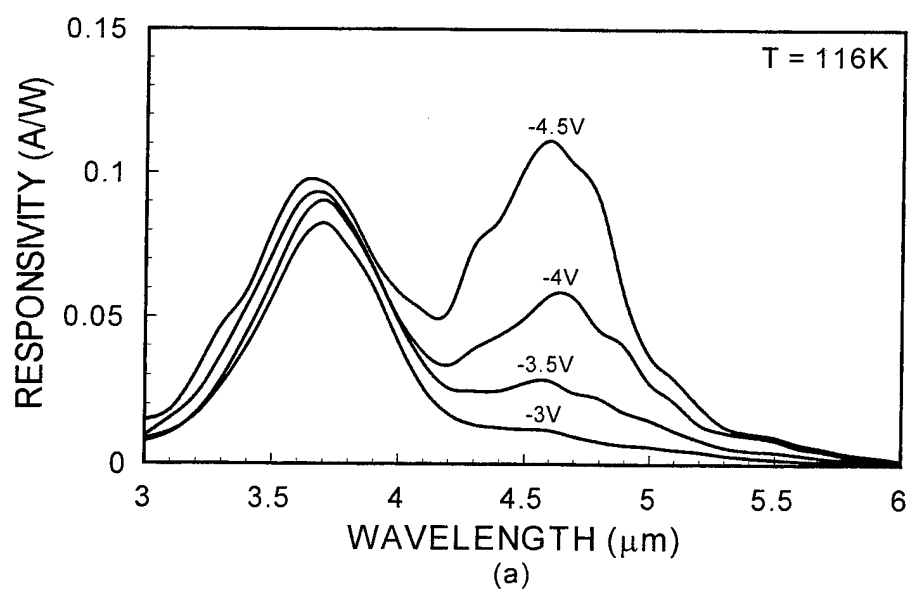
Figure 4.4 The spectral responsivity of the MWIR TC-QWIP grown on the InP substrate measured at T = 116K, under (a) negative bias and (b) positive bias conditions.

5 A HIGH-STRAIN MULTI-COLOR, TWO-STACK InGaAs/AlGaAs/InGaAs TC- QWIP AND AN InGaAs/AlGaAs BC- QWIP FOR THE LWIR AND MWIR DUAL- BAND DETECTION

5.1 Introduction

Quantum well infrared photodetectors (QWIPs) have been developed for 3-5 μm mid-wavelength infrared (MWIR) and 8-14 μm long-wavelength infrared (LWIR) spectral regimes in the past decade [6,10,26-34]. The matured III-V compound semiconductor growth technology and the flexibility of the device structure enable the rapid development of various QWIP structures. In particular, the multi-color IR detectors for practical imaging applications such as target discrimination, remote sensing system, medical imaging, and tracking system have been widely investigated by using the multi-stack QWIP and voltage-tunable asymmetrical coupled quantum well structures. A high-strain triple-coupled quantum well infrared photodetector (TC-QWIP) [8,13] grown on the semi-insulating GaAs substrate has been demonstrated for 8-14 μm long-wavelength infrared detection, which has high performance due to the very high sensitivity, large normal incidence absorption without grating coupler, and the large voltage tunable wavelength for two LWIR peak detection wavelengths. In addition, the simplified (short-period) quantum well infrared photodetector (S-QWIP) [35] offers a number of advantages over the conventional QWIP structure with 40 to 50 periods due to the reduced growth time, low bias operation, low power consumption, and simple processing. In this chapter, we report a high-strain, multi-color, two-stack InGaAs/AlGaAs/InGaAs asymmetrical triple-coupled (TC-) and an InGaAs/AlGaAs bound-to-continuum (BC)

quantum well infrared photodetector for long-wavelength infrared (LWIR) and mid-wavelength infrared (MWIR) dual band detection grown on the GaAs substrate.

5.2 Device Design and Fabrication

The top stack is for the LWIR detection, which composes of a 5.5 nm deep $In_{0.25}Ga_{0.75}As$ quantum well Si-doped to $N_d = 7x10^{17}$ cm^{-3}, two undoped 4 nm shallow $In_{0.12}Ga_{0.88}As$ quantum wells, and two 2 nm $Al_{0.08}Ga_{0.92}As$ inner barriers between 50 nm thick $Al_{0.08}Ga_{0.92}As$ barriers as a unit cell. The unit cell was repeated 20 times, and was sandwiched between two undoped 100 nm GaAs spacer layers to reduce the tunneling current from the contacts to the QWs. The bottom stack for the MWIR QWIP consists of 3-period of symmetrical $In_{0.3}Ga_{0.7}As/Al_{0.3}Ga_{0.7}As$ BC-QWIP structure. Finally, the ohmic contact layers (Si-doped to n = $2x10^{18}$ cm^{-3}) were grown on the top of the LWIR stack and on the bottom of the MWIR stack, and between the two stacks. Table 5.1 lists the layer structure of this high- strain multi-color two-stack QWIP structure.

Figure 5.1 shows the schematic conduction band diagram and the intersubband transition scheme for the stacked LWIR TC-QWIP and MWIR BC-QWIP. For the LWIR TC-QWIP, the 50 nm thick $Al_{0.08}Ga_{0.92}As$ barrier will turn into a triangular barrier for the conduction of the photo-generated carriers through them when the negative bias voltage is large enough. Therefore, both the bound-to-bound (B-B) and bound-to-continuum (B-C) transitions can be detected at higher negative bias voltages. The photo-excited electrons from the E_1 to E_c (bound-to-continuum) states contribute to the photocurrent for the MWIR BC-QWIP.

The test mesa structure with an active area of 216x216 μm² was fabricated to characterize the device performance by using standard photolithography and wet chemical etching procedure. The LWIR TC- and stacked-QWIP test devices were etched from the top contact layer onto the middle and the bottom contact layers, respectively. The MWIR BC-QWIP was etched from the middle contact layer onto the bottom contact layer after both the top contact layer and the LWIR stack were completely removed. The LWIR TC- and stacked-QWIP test devices were annealed at T = 450 °C for two minutes after AuGe/Ni/Au (300Å/100Å/1000Å) evaporation. The MWIR BC-QWIP test device was annealed at T = 450 °C for 10 seconds after AuGe/Ag/Au (300Å/1000Å/1500Å) evaporation. The 45° facet was polished on the GaAs substrate for IR illumination.

5.3 Results and Discussion

5.3.1 Dark Current Measurements

Figure 5.2 shows the dark current versus bias voltage (I-V) curves of the LWIR TC-QWIP measured at T = 40, 60, and 77K along with the 300 K background window current at 180° field of view (FOV). The LWIR TC-QWIP is under background limited performance (BLIP) when the applied bias is between –8V and 7V at T_{BLIP} = 40K, and between –4V and +2.5V at T_{BLIP} = 60K. Figure 5.3 shows the dark current versus bias voltage (I-V) curves of the MWIR BC-QWIP measured at T = 40, 77, 100, and 120 K along with the 300 K background window current at 180° field of view (FOV). The MWIR BC-QWIP is under background limited performance (BLIP) when the applied bias is between –0.95V and 0.9V at T = 77 K. The BLIP temperature is around T = 90 K

for $-0.5V < V_b < 0.4V$. Figure 5.4 shows the dark current versus bias voltage (I-V) curves for the stacked-QWIP measured at T = 40, 60, and 77K. The 300K window current with 180° field of view (FOV) is also shown in Figure 5.4. The stacked-QWIP is also under BLIP in the entire range of the applied bias voltages ($-9V < V_b < 8V$) at T = 40K while this device is under BLIP for biases between $-5V$ and $3V$ at T = 60K.

5.3.2 Photoresponse Measurements

The spectral response was measured at T = 40 K for the LWIR TC-QWP, T = 40, 77, 100, and 120 K for the MWIR BC-QWIP, and T = 40 and 77K for the stacked-QWIP by using an 1/8 monochromater, a calibrated blackbody IR source (T = 1273 K), and Oxford CCC1204 closed cycle liquid helium cryostat at 200 Hz chopped frequency. Figure 5.5 shows the spectral responsivity of the LWIR TC-QWIP measured at different bias voltages and T = 40K. As shown in Chapter 2, 3, and 4 on TC-QWIP structures, the bound-to-continuum (B-C) transitions can be detected under the positive and lower negative bias voltages while the bound-to-bound (B-B) transitions were observed at higher negative bias voltages. At T = 40K, the peak responsivity at $-7.8V$ was found to be 2.63 A/W at $\lambda_p = 10.3$ μm. The E_1 to E_3 bound-to-bound (B-B) transition at T = 40K was observed for bias voltages greater than -6V. The shift of peak wavelength with applied bias for the B-B and B-C transitions is due to the quantum confined Stark effect, which were found to be about 0.4 μm (10.7 ~ 10.3 μm) and 0.3 μm (7.9 ~ 7.6 μm) between $-6V$ and $-7.8V$ at T = 40K, respectively. The extrapolated peak wavelengths at zero bias voltage were found to be 9.1 μm and 12.2 μm for the E_1-E_C and E_1-E_3

transitions, respectively. The background limited performance (BLIP) detectivity (D^*_{BLIP}) at $\lambda_p = 10.3$ μm and $V_b = -7.8$V was found to be 2.0×10^{10} cm-Hz$^{1/2}$/W at T = 40K.

Figure 5.6 (a), (b), (c), and (d) show the spectral responsivity of the MWIR BC-QWIP measured at different bias voltages and temperatures. The bound-to-continuum (B-C) transition was obtained for MWIR detection. At T = 77 K, the peak responsivities under negative biases were found to increase with bias voltage up to −1.3V, and the maximum peak responsivity was 0.27 A/W at $\lambda_p = 5.1$ μm and $V_b = -1.3$V. The peak responsivity was found to be 0.46 A/W at $\lambda_p = 5.1$ μm, $V_b = 1.1$V and T = 77 K. The peak wavelength at $\lambda_p = 5.1$ μm was found to be nearly independent of the bias voltage and temperature. Figure 5.7(a), (b), (c), and (d) show the peak responsivity versus bias voltage for the MWIR BC-QWIP measured at different temperatures. The peak responsivity at $\lambda_p = 5.1$ μm was initially increased up to the maximum value and then dropped slightly with applied bias voltage. At higher bias voltages, the photoresponse was saturated due to the large thermionic emission dark current. Figure 5.8 (a) and (b) show the peak responsivity versus temperature at negative and positive bias voltages, respectively. The responsivity at higher bias voltage was slightly decreased with increasing temperature. However, the responsivities at lower bias voltage were found to first increase and then decrease with increasing temperature in which the responsivity at higher biases can reach the maximum value at lower temperature. Finally, the peak detectivity and the collection quantum efficiency under background limited performance (BLIP) were found to be $D^*_{BLIP} = 1.187 \times 10^{10}$ cm-Hz$^{1/2}$/W and $\eta g = 6.5$ % at $\lambda_p = 5.1$ μm, T = 77 K, and $V_b = -1.3$V, respectively.

Figure 5.9 (a) and (b) show the spectral responsivity of the MWIR and LWIR stacked-QWIP measured at different temperatures and bias voltages. The MWIR detection peak wavelengths were found to be of λ_p = 5.1 μm and were independent of bias voltage. The peak responsivity at V_b = -9V and λ_p = 5.1 μm was 0.2 A/W at T = 40K. The two peak detection wavelengths due to the E_1-E_C and E_1-E_3 transitions were also observed in the LWIR region. The peak responsivity was 1.76 A/W at V_b = -9V, λ_p = 10.3 μm, and T = 40K. The wavelength tunability for the E_1-E_3 and E_1-E_C transitions at T = 40K was about 0.4 μm from 10.7 μm to 10.3 μm and 0.3 μm from 7.9 μm to 7.6 μm between -7V and -9V, respectively. The tuning peak wavelengths at T = 77K were found to be 0.2 μm from 11.0 μm to 10.8 μm between –6V and –7V. The responsivity at the same bias voltage was decreased with increasing temperature as a common result for the large period QWIPs (more than 20 periods). The background limited performance (BLIP) detectivity (D^*_{BLIP}) at λ_p = 10.3 μm was found to be 1.63 x 10^{10} cm-$Hz^{1/2}$/W at V_b = -9V and T = 40K.

5.4 Conclusions

We have demonstrated a high performance high-strain multi-color, two-stack, InGaAs/AlGaAs/InGaAs TC-QWIP and InGaAs/AlGaAs BC-QWIP for LWIR and MWIR dual band detection. A maximum responsivity of 2.63 A/W was obtained at λ_p = 10.3 μm, V_b = -7.8V, and T = 40K for the LWIR TC-QWIP. The strong quantum confined Stark shift and the rapid increase of the peak responsivity with applied bias for the E_1-E_3 transition were observed in both the LWIR TC- and stacked- QWIPs. The peak responsivity at λ_p = 5.1 μm due to bound-to-continuum (B-C) transition was obtained up to T = 120 K for the MWIR BC-QWIP. The peak responsivity for this device at higher

bias voltages was less sensitive to temperature while the peak responsivity at lower bias voltages was found to first increase and then decrease with increasing temperature. The responsivity at higher bias voltages was saturated due to the saturation of the optical gain at high bias. The peak wavelength for the MWIR BC-QWIP was found to be at $\lambda_p = 5.1$ μm, which was found to be independent of the bias voltage and temperature.

Since the LWIR TC-QWIP reported here used 20 periods of QWs, a large bias voltage (up to 9 V) has to be applied to this device in order to obtain gain-quantum efficiency product and high responsivity. For the low background and low bias applications, short period (3-5 period) TC-QWIP structure should be used so that high peak responsivity and detectivity can be achieved in a TC-QWIP under low bias conditions.

Table 5.1 The layer structure of a high-strain multi-color, two-stack InGaAs/AlGaAs/InGaAs TC-QWIP and an InGaAs/AlGaAs BC-QWIP grown on the GaAs substrate for the LWIR and MWIR dual band detection.

Layer		Thickness (Å)	Dopant	Concentration (cm^{-3})
n GaAs (top contact)		5000	Si	$2x10^{18}$
i GaAs		1000	none	none
i $Al_{0.08}Ga_{0.92}As$		500	none	none
i $In_{0.12}Ga_{0.88}As$		40	none	none
i $Al_{0.08}Ga_{0.92}As$		20	none	none
i $In_{0.12}Ga_{0.88}As$	X 20	40	none	none
i $Al_{0.08}Ga_{0.92}As$		20	none	none
n $In_{0.25}Ga_{0.75}As$		55	Si	$7x10^{17}$
i $Al_{0.08}Ga_{0.92}As$		500	none	none
i GaAs		1000	none	none
n GaAs		5000	Si	$2x10^{18}$
i $Al_{0.3}Ga_{0.7}As$		300	none	none
n $In_{0.3}Ga_{0.7}As$	X 3	43	Si	$2.5x10^{18}$
i $Al_{0.3}Ga_{0.7}As$		300	none	none
n GaAs (bottom contact)		10000	Si	$2x10^{18}$
S.I. GaAs substrate		625 ± 25 μm	none	none
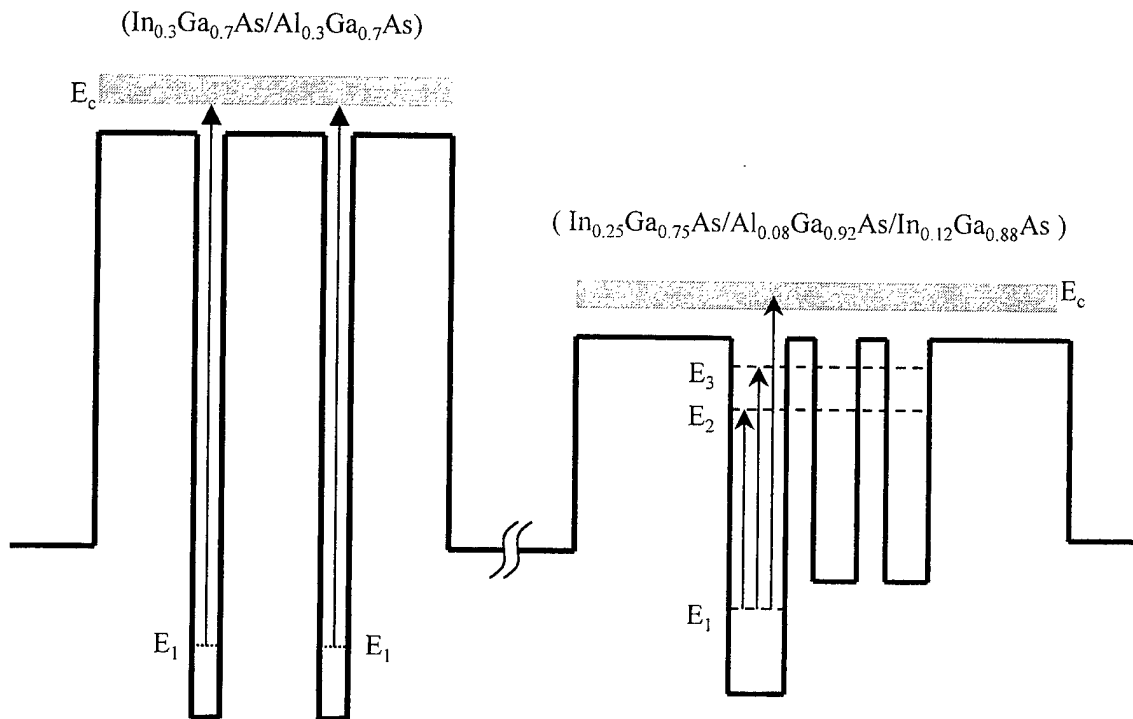
Figure 5.1 The schematic conduction band diagram of a high strain, multi-color, two-stack, InGaAs/AlGaAs/InGaAs LWIR TC- and GaAs/AlGaAs MWIR QWIPs grown on the GaAs substrate.
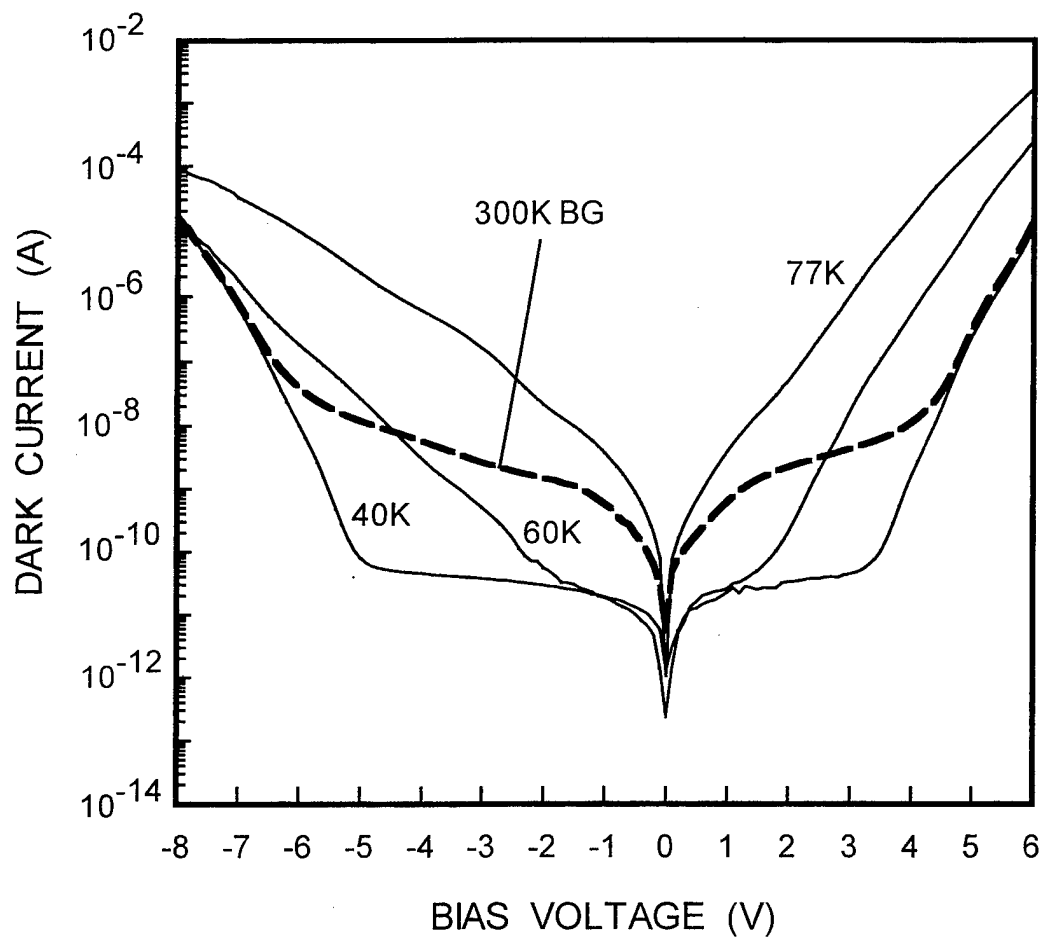
Figure 5.2 The dark current versus bias voltage (I-V) measured at T = 40, 60, and 77K along with the 180° field of view (FOV) 300 K background window current of the LWIR TC-QWIP.
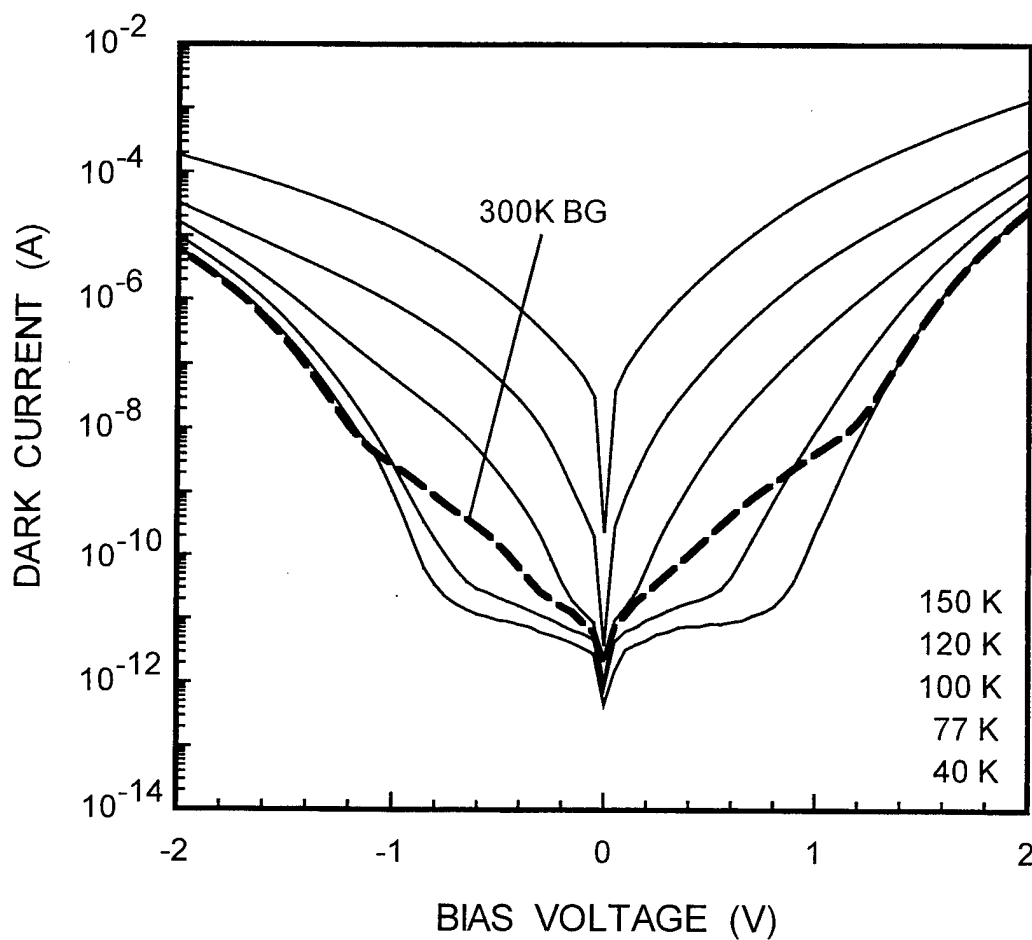
Figure 5.3 The dark current versus bias voltage (I-V) measured at T = 40, 77, 100, 120, and 150K along with the 180° field of view (FOV) 300 K background window current of the MWIR BC-QWIP.
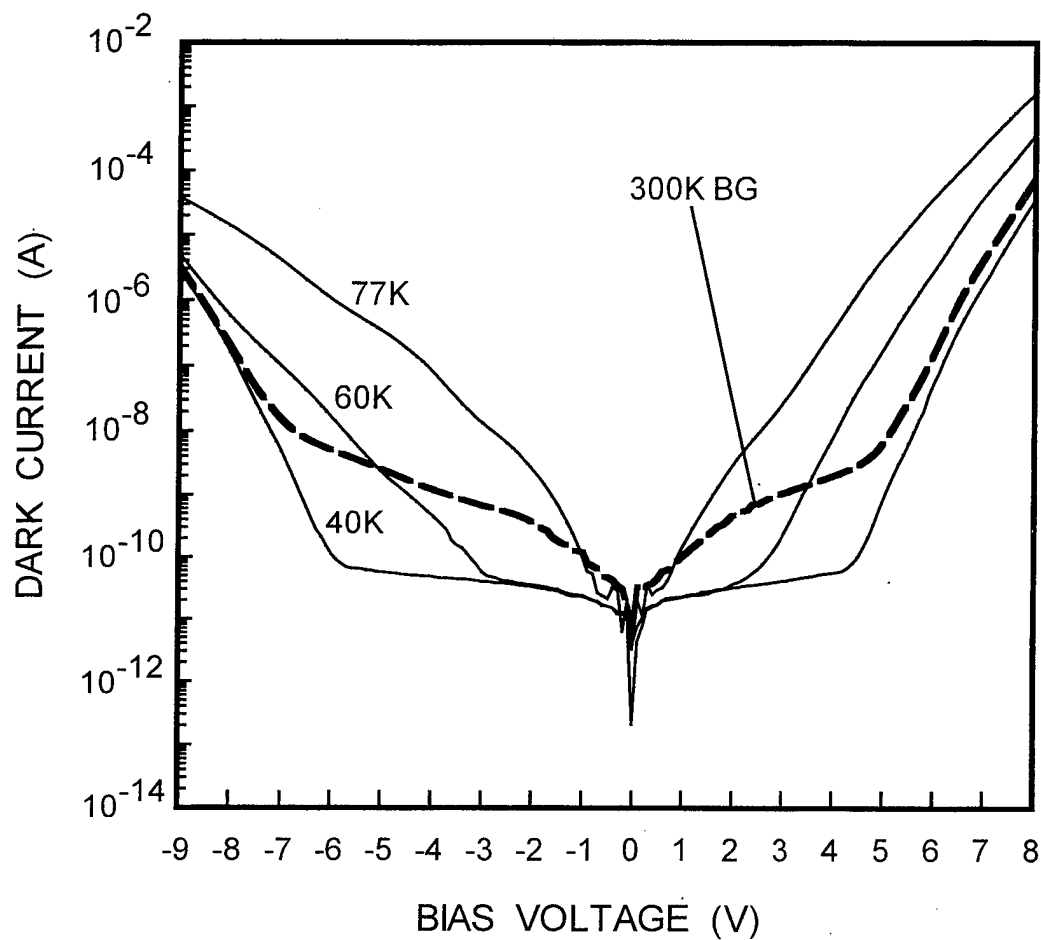
Figure 5.4 The dark current versus bias voltage (I-V) measured at T = 40, 60, and 77K along with the 180° field of view (FOV) 300°K background window current of the stacked-QWIP.
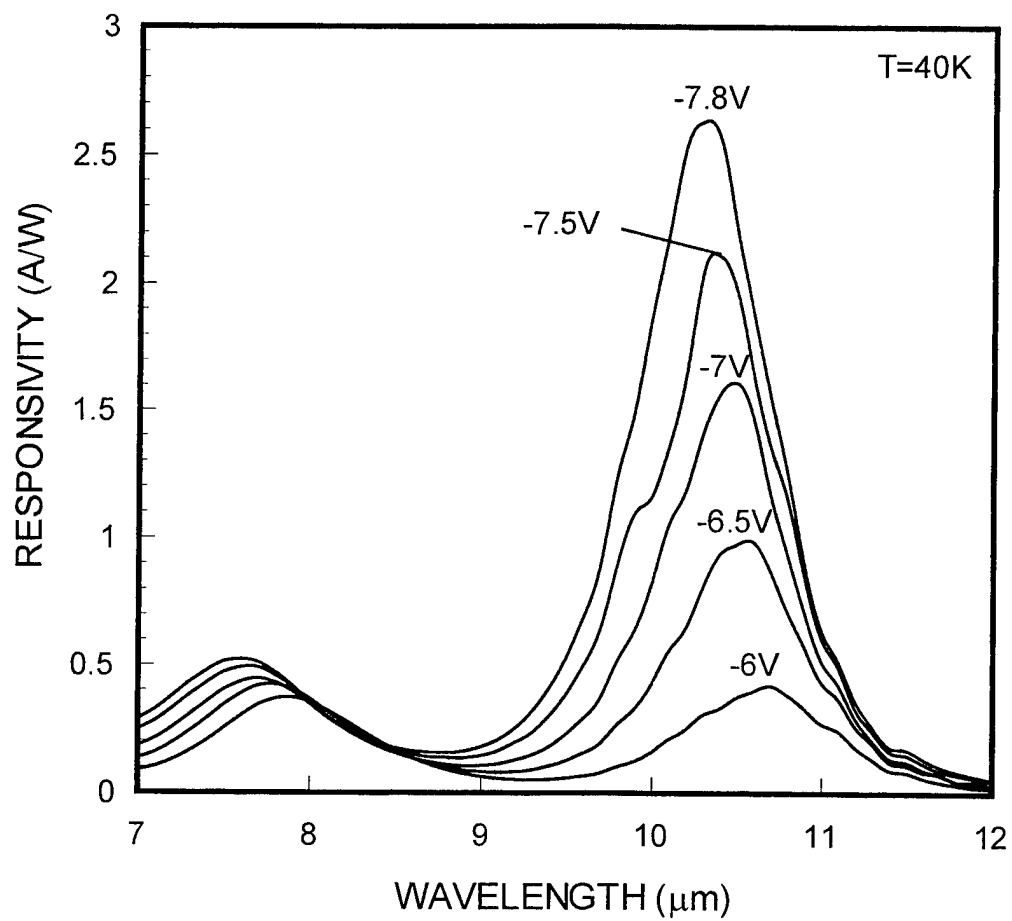
Figure 5.5 The spectral responsivity of the LWIR TC-QWIP measured at T = 40K
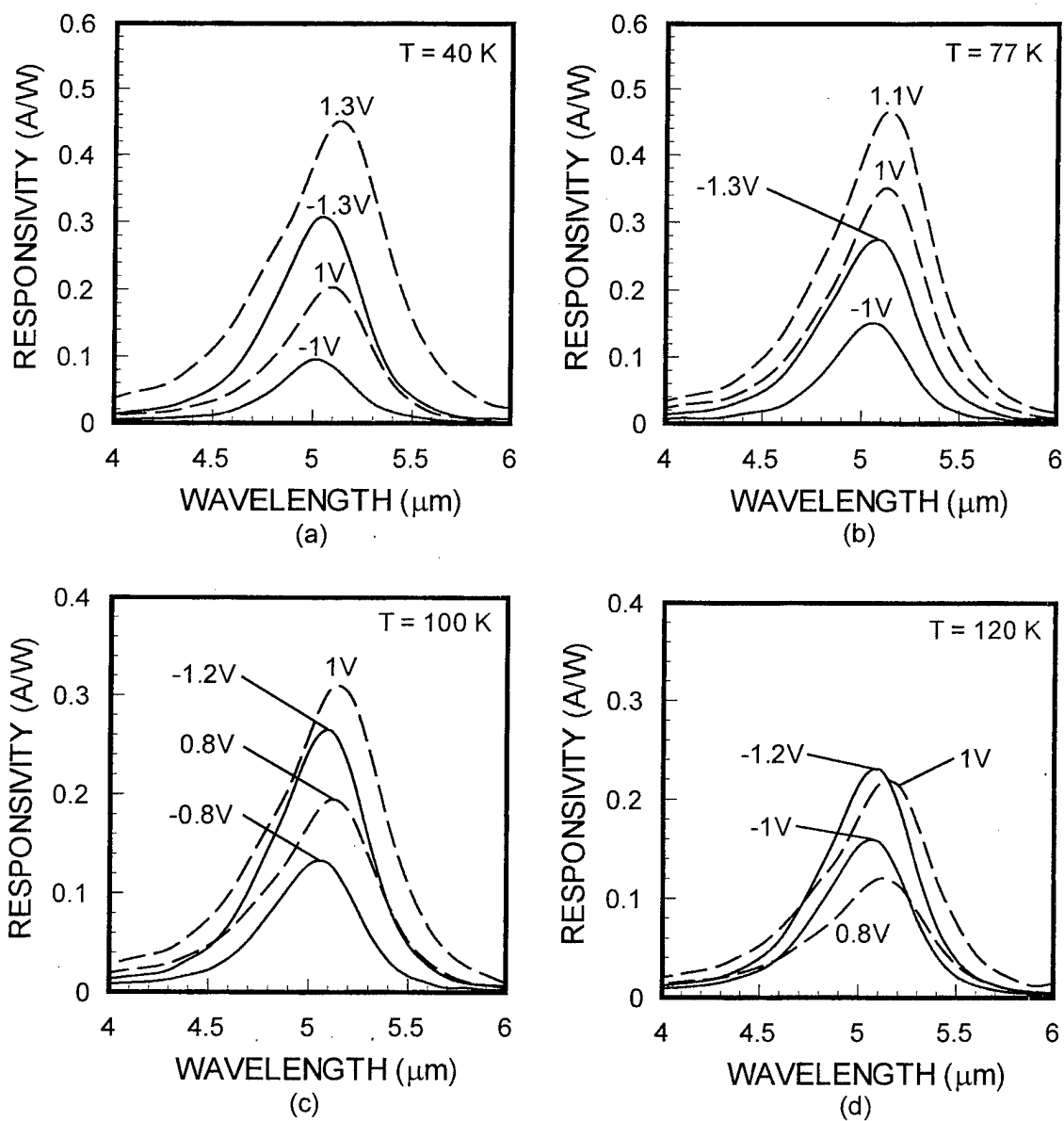
Figure 5.6 The spectral responsivity of the MWIR BC-QWIP measured at (a) 40, (b) 77, (c) 100, and (d) 120 K.
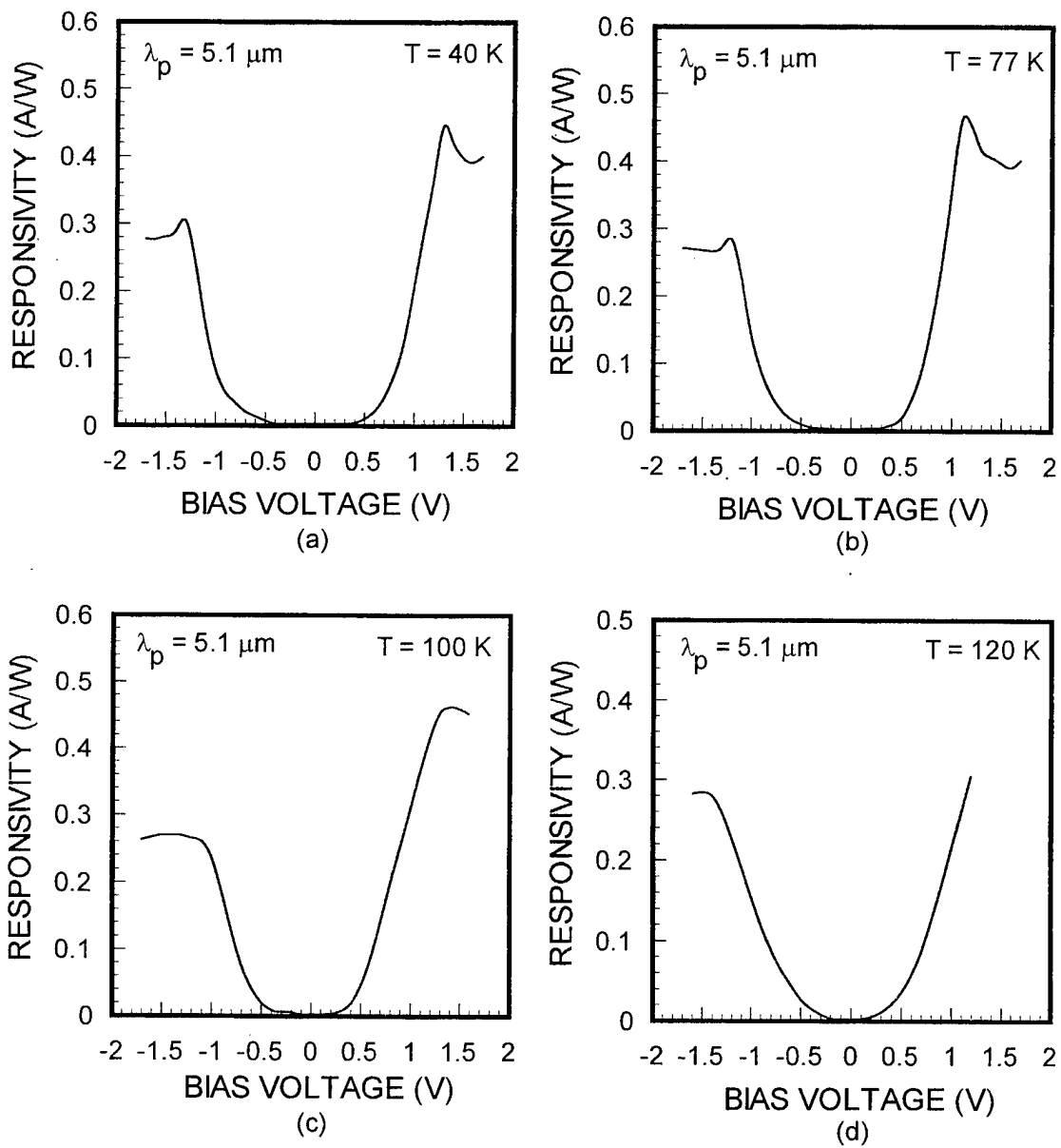
Figure 5.7 The peak responsivity at $\lambda_p = 5.1$ μm versus bias voltage for the MWIR BC-QWIP at (a) 40, (b) 77, (c) 100, and (d) 120 K.
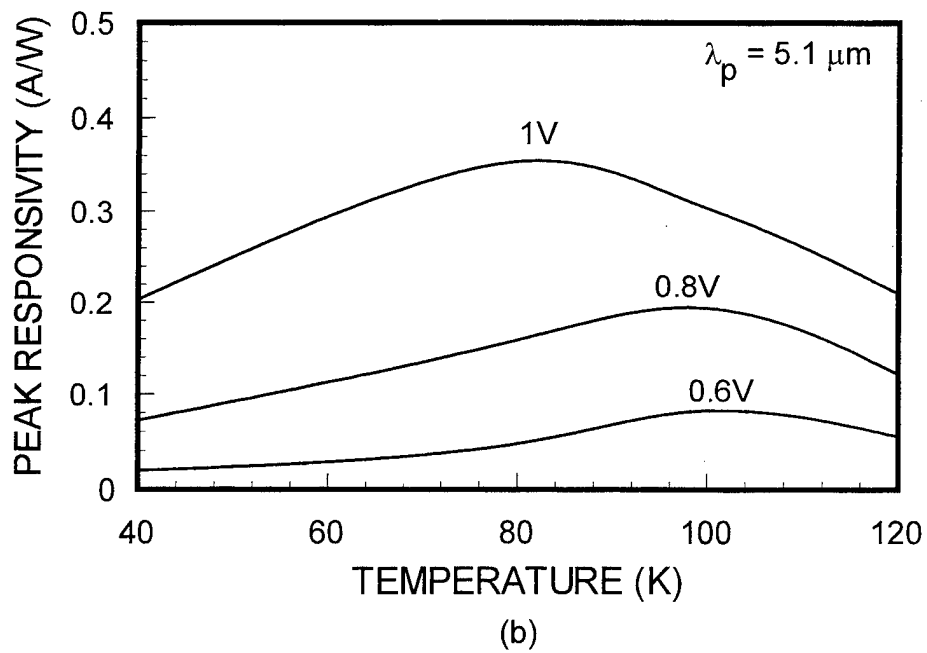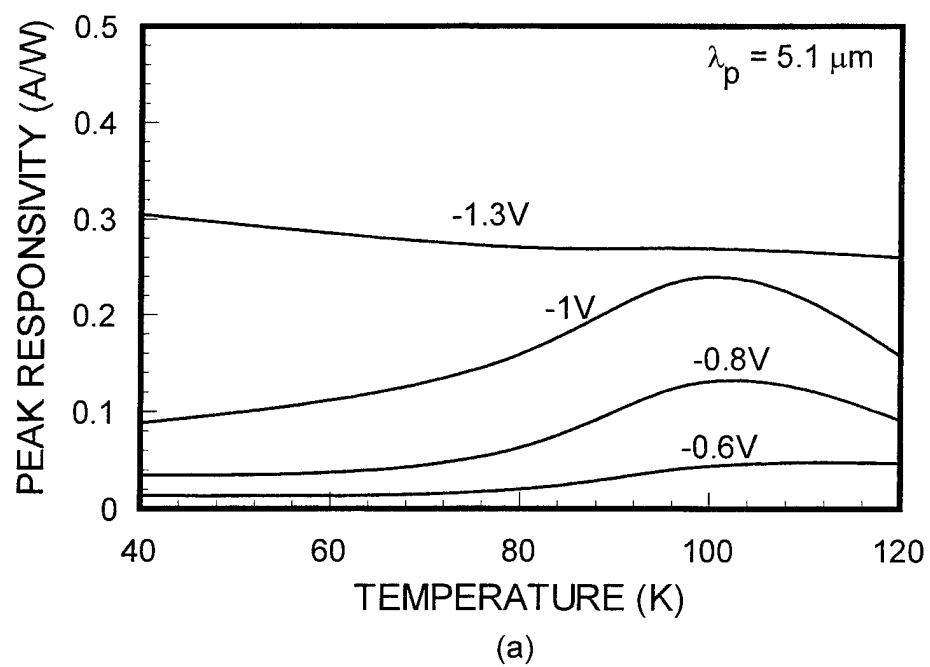
Figure 5.8 The peak responsivity versus temperature for the MWIR BC-QWIP under (a) negative and (b) positive bias voltages
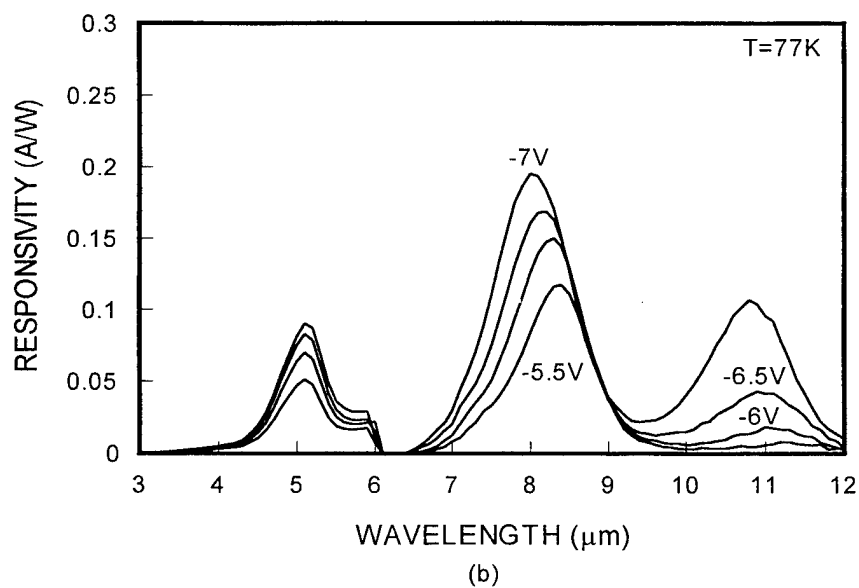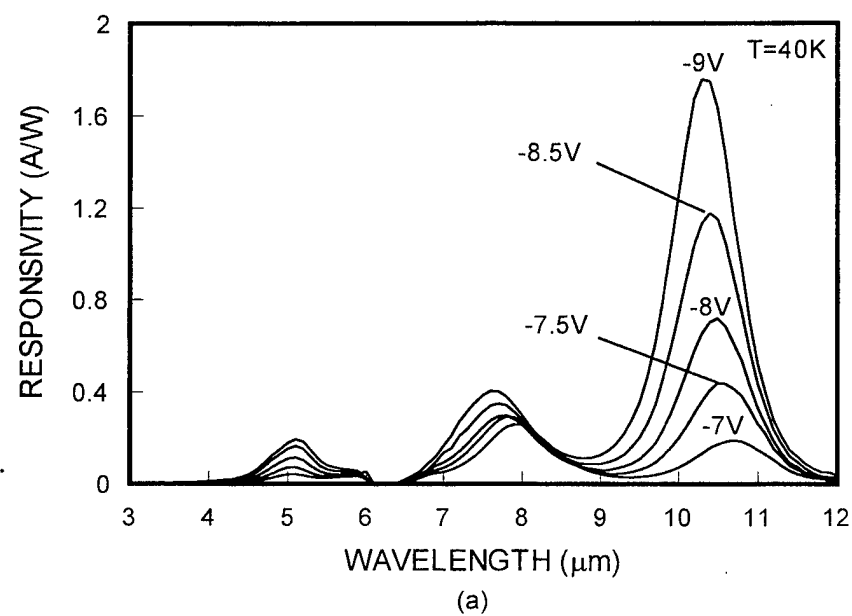
Figure 5.9 The spectral responsivity of the stacked-QWIP measured at (a) T = 40K and (b) T = 77K.

6 A HIGH-STRAIN $In_{0.27}Ga_{0.73}As$/GaAs QUANTUM WELL INFRARED PHOTODETECTOR FOR LWIR DETECTION

6.1 Introduction

Recently, the quantum well infrared photodetectors (QWIPs) using strain layer structure has been extensively investigated [10]. The strain layers induced by the lattice mismatched can take advantage of the ability to control the electronic and optical properties of the heterostructure by modifying the energy band structure. In the design of the strain structure, the critical thickness is of great importance because below the critical thickness the thermodynamically stable quality of the pseudomorphic layers can be obtained and beyond the critical thickness, the misfit dislocations can be produced and then the strain relaxes. Therefore, the quantum well width should be decreased with the increasing In mole fraction in $In_xGa_{1-x}As$/GaAs material system. When the incident light is perpendicular to the quantum well layers, the intersubband absorption is theoretically not allowed by the quantum mechanical selection rule. Therefore, the efficient light coupling scheme is required for normal incidence absorption, which is the geometry for the foacl plane array (FPA). The cross-grating (e.g., 2-D) coupler [7,36] can greatly improve the device performance up to 4 to 5 times higher than the 45° edge coupling. The main concern of the grating coupler is the optimization of the grating structure for a specific peak wavelength. The relationship between the peak detection wavelength and grating parameters for maximum coupling efficiency is given by [10]

$$\lambda_p^{'} = 4hg^2 / \left(4h^2 + g^2\right) \tag{6.1}$$

where λ'_p is the peak wavelength in the medium, h is the depth of the grooves, and g is the periodicity of the grating. In this chapter, a high- strain n-type GaAs/In$_{0.27}$Ga$_{0.73}$As BC-QWIP grown on the GaAs substrate has been fabricated and characterized for long-wavelength infrared (LWIR) detection.

6.2 Device Design and Fabrication

The HS BC-QWIP consists of 6 nm In$_{0.27}$Ga$_{0.73}$As quantum well (Si-doped to 7 x 10^{17} cm^{-3}) separated by 50 nm thick undoped GaAs barrier as a period, which was repeated 20 times and then sandwiched by two undoped 100 nm GaAs spacer layers to reduce the tunneling current from the contacts to quantum wells. The ohmic contact layers (Si-doped to 2 x 10^{18} cm^{-3}) were grown on the top (300 nm) and bottom (500 nm) of this HS BC-QWIP. Table 6.1 gives the layer structure of the sample #97-2N02 including this HS BC-QWIP structure. Figure 6.1 shows the schematic conduction band diagram and the intersubband transition scheme for this HS BC-QWIP.

Two batches of HS BC-QWIP test devices with an active mesa area of 216x216 μm^2 were fabricated by using standard photolithography and wet chemical etching procedure. One batch of devices without grating was polished to 45° facet on the GaAs substrate for IR back-illumination, and the other batch of devices was covered with the two-dimensional (2-D) square aperture mesh metal (Au) grating on the top of mesa structure. The period and the aperture width of this mesh metal grating were $g = 4$ μm and $a = 2$ μm, respectively. Figure 6.2 shows (a) the schematic diagram for the 2-D square mesh metal grating and (b) the side view under back-illumination, respectively. These devices were annealed at T = 450 °C for 10 seconds after AuGe/Ag/Au (300Å/1000Å/1500Å) E-

beam evaporation The test devices were bonded on the TO-8 header for electrical connection and then mounted in the closed cycle cryogenic system for low temperature measurements. The dark I-V measurements followed by the analysis of the thermal activation energy and the spectral responsivity measurement were accomplished to characterize the device performance. The results of this HS BC-QWIP device measurements are described follows:

6.3 Results and Discussion

6.3.1 Dark Current Measurements

Figure 6.3 shows the dark current versus bias voltage (I-V) curves of the HS BC-QWIP measured at T = 35, 40, 50, 60, and 77K along with the 300 K background window current at 180° field of view (FOV). The HS BC-QWIP is under background limited performance (BLIP) in the whole applied bias region at T = 35 and 40K, and between −1.4V and 0.5V at T = 50K.

6.3.2 Analysis of Thermal Activation Energy

The activation energy depending on bias voltage has been studied to understand the dark current transport mechanism of this HS BC-QWIP. It is well known that under dark condition the thermionic emission due to the electrons transferred out of the quantum wells is dominant at low biases and high temperatures while the thermally generated carriers tunneling through the barriers is more important at high biases and low temperatures. The dark current of QWIP is given by

$$I_d = Aevn, \tag{6.2}$$

where A is the detector area, e is the electronic charge, v is the average drift velocity, and n is the density of mobile carriers, which can be expressed as

$$v = \mu F / [1 + (\mu F / v_s)^2]^{1/2}, \tag{6.3}$$

$$n = (m^* / \pi \hbar^2 L_p) \int_{E_1}^{\infty} f(E) T(E, F) dE, \tag{6.4}$$

where μ is the electron mobility, F is the average electric field, v_s is the electron saturation velocity, m^* is the electron effective mass in the QW, L_p is the QWIP length, $f(E)$ is the Fermi-Dirac distribution function, and $T(E,F)$ is the bias-dependent tunneling current transmission coefficient for a single barrier. For the sake of simplicity, we can assume that $T(E) = 0$ for $E < E_b$ and $T(E) = 1$ for $E > E_b$. Therefore, n and I_d can be given by,

$$n = (m^* kT / \pi \hbar^2 L_p) \exp[-E_{ac} / kT], \tag{6.5}$$

$$I_d = A \left(\frac{m^* kT}{\pi \hbar^2 L_p} \right) \left(\frac{\mu F}{\left[1 + (\mu F / v_s)^2 \right]^{1/2}} \right) \exp \left[\frac{-E_{ac}}{kT} \right]. \tag{6.6}$$

where E_{ac} ($=E_b - E_1 - E_F$) is the activation energy and E_b, E_1, and E_F are the barrier energy, the ground state energy, and Fermi energy, respectively. The Fermi energy (E_F) can be calculated from

$$N_d = \frac{m^* kT}{\pi \hbar^2 L_w} \ln \left[1 + \exp \left(\frac{E_F}{kT} \right) \right]. \tag{6.7}$$

As a result, the dark current (I_d) is exponentially related to the activation energy (E_{ac}) as follows,

$$\frac{I_d}{T} \propto \exp \left[\frac{-E_{ac}}{kT} \right]. \tag{6.8}$$

63

The activation energy (E_{ac}) can be obtained from the slope of the normalized dark current (I_d/T) versus the inverse temperature ($1000/T$) straight line on a semilog scale. Figure 6.4(a) and (b) show the normalized dark current (I_d/T) versus the inverse temperature at negative biases and the activation energy (E_{ac}) versus the applied negative bias voltage, respectively. The excellent linearity was obtained at different negative biases as shown in Figure 6.4(a). The activation energy at $V_b = 0V$ was found to be $E_{ac} = 89$ meV by extrapolating the experimental curves. Therefore, the responsivity cutoff energy (E_b-$E_1 = 107$ meV) can be obtained with the Fermi energy ($E_F = 18$ meV) in which the ground state energy ($E_1 = 47$ meV) and the Fermi energy (E_F) was calculated from Transfer Matrix Method (TMM) and Eq. (6.7), respectively. The corresponding cutoff wavelength was $\lambda_c = 11.58$ μm, which is in good agreement with the measured cutoff $\lambda_c = 11.4$ μm. As clearly shown in Figure 6.4(b), the activation energy was decreased with the increasing bias voltage, which was due to the electron tunneling conduction through the barriers at high biases.

6.3.3 Photoresponse measurements

The spectral response was measured at T = 35 K for the HS BC-QWIP by using an 1/8 monochromater, a calibrated blackbody IR source (T = 1273 K), and Oxford CCC1204 closed cycle liquid helium cryostat at 200 Hz chopped frequency. Figure 6.5(a) and (b) show the spectral responsivity of 45° facet back illumination for the HS BC-QWIP at different bias voltages and T = 35K. The peak wavelength was found to be 10.5 μm independent of the increasing bias voltage and the bias polarity. The spectral responsivity was dramatically increased with the increasing bias voltage. The maximum spectral

responsivity at λ_p = 10.5 μm was achieved as much as 8.16 A/W at V_b = -3V and T = 35K. The highly compressive strain can induce the better photoresponsivity due to the reduction of the electron effective mass as proven in this HS BC-QWIP device. It is noted that this responsivity is three times larger than that of high strain triple-coupled QWIP (TC-QWIP) in chapter 2 and 5. The responsivity of normal incidence back illumination with the 2-D square mesh metal grating coupler was also measured at T = 35K. The results of the spectral responsivity measurement of the HS BC-QWIP with grating coupler are shown in Figure 6.6(a) and (b). The peak responsivity was found to be 2.8 A/W at λ_p = 10.5 μm, V_b = -3V and T = 35K, which was much smaller than that of the 45° facet back illumination because the grating parameters with g = 4 μm and a = 2 μm was not optimized for 10.5 μm peak. The proper selection of the grating parameters is most important to obtain the maximum grating coupling efficiency. The spectral responsivity under negative bias was higher than that under positive bias as shown in Figure 6.5 and 6.6. It indicates that the better device characteristic can be obtained under negative biases due to the higher responsivity and lower dark current. The background limited performance (BLIP) detectivities (D^*_{BLIP}) for both the 45° facet and grating HS BC-QWIPs were found to be 3.44 x 10^{10} cm-Hz$^{1/2}$/W and 2.02 x 10^{10} cm-Hz$^{1/2}$/W at λ_p = 10.5 μm, V_b = -3V and T = 35K, respectively.

6.4 Conclusions

We have demonstrated a GaAs/$In_{0.27}Ga_{0.73}As$ n-type high strain bound-to-continuum quantum well infrared photodetector (HS BC-QWIP) for 7 – 13 μm long-wavelength infrared (LWIR) detection grown on the GaAs substrate. The activation energy was

calculated from the dark current measurement to observe the actual barrier height and the current transport mechanism. Furthermore, the spectral responsivity was measured with 45° facet back illumination and with 2-D square mesh metal grating back illumination. The maximum responsivities for both the 45° facet and grating HS BC-QWIPs were 8.16 A/W and 2.8 A/W at λ_p = 10.5 μm, V_b = -3V and T = 35K, respectively. The background limited performance (BLIP) detectivities (D^*_{BLIP}) for the 45° facet HS BC-QWIPs was found to be 3.44 x 10^{10} cm-Hz$^{1/2}$/W at λ_p = 10.5 μm, V_b = -3V and T = 35K.

Table 6.1 The layer structure of a n-type $In_{0.27}Ga_{0.73}As$/GaAs high strain bound-to continuum quantum well infrared photodetector (HS BC-QWIP) grown on GaAs substrate for LWIR detection: the top stack is this HS BC-QWIP.

Layer		Thickness (Å)	Dopant	Concentration (cm^{-3})
n GaAs (top contact)		3000	Si	2×10^{18}
i GaAs		1000	none	none
i GaAs		500	none	none
n $In_{0.27}Ga_{0.73}As$	20-period	60	Si	7×10^{17}
i GaAs		500	none	none
i GaAs		1000	none	none
n GaAs (middle contact)		5000	Si	2×10^{18}
i $Al_{0.3}Ga_{0.7}As$		300	none	none
n $In_{0.35}Ga_{0.65}As$	3-period	45	Si	2.5×10^{18}
i $Al_{0.3}Ga_{0.7}As$		300	none	none
n GaAs (bottom contact)		1000	Si	2×10^{18}
S.I. GaAs substrate		625 ± 25 μm	none	none
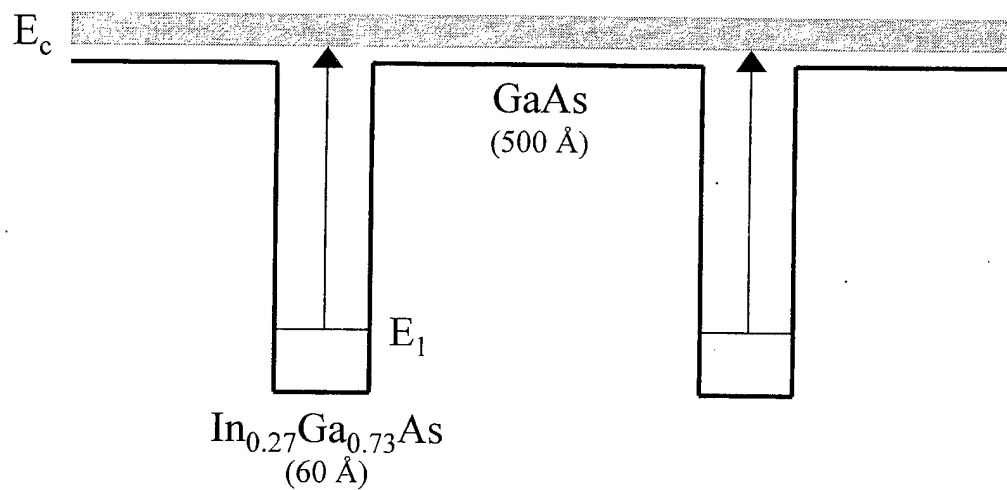
Figure 6.1   The schematic conduction band diagram of a InGaAs/GaAs high strain bound-to-continuum quantum well infrared photodetector (HS BC-QWIP) for long-wavelength detection range grown on GaAs substrate.

(a)

(b)
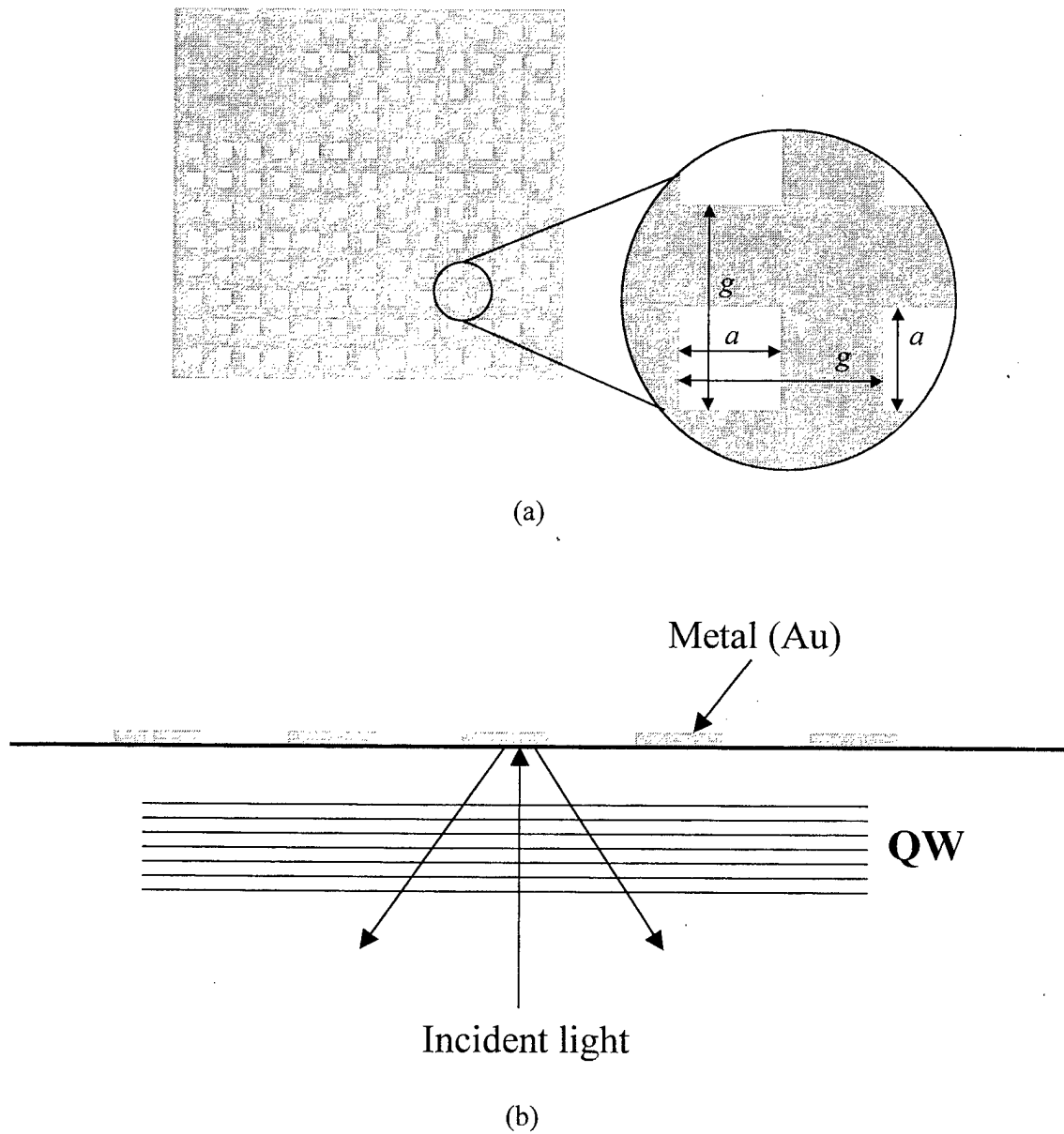
Figure 6.2 (a) The structure of square aperture mesh metal grating and (b) side view under back-illumination: the dark area is metal.
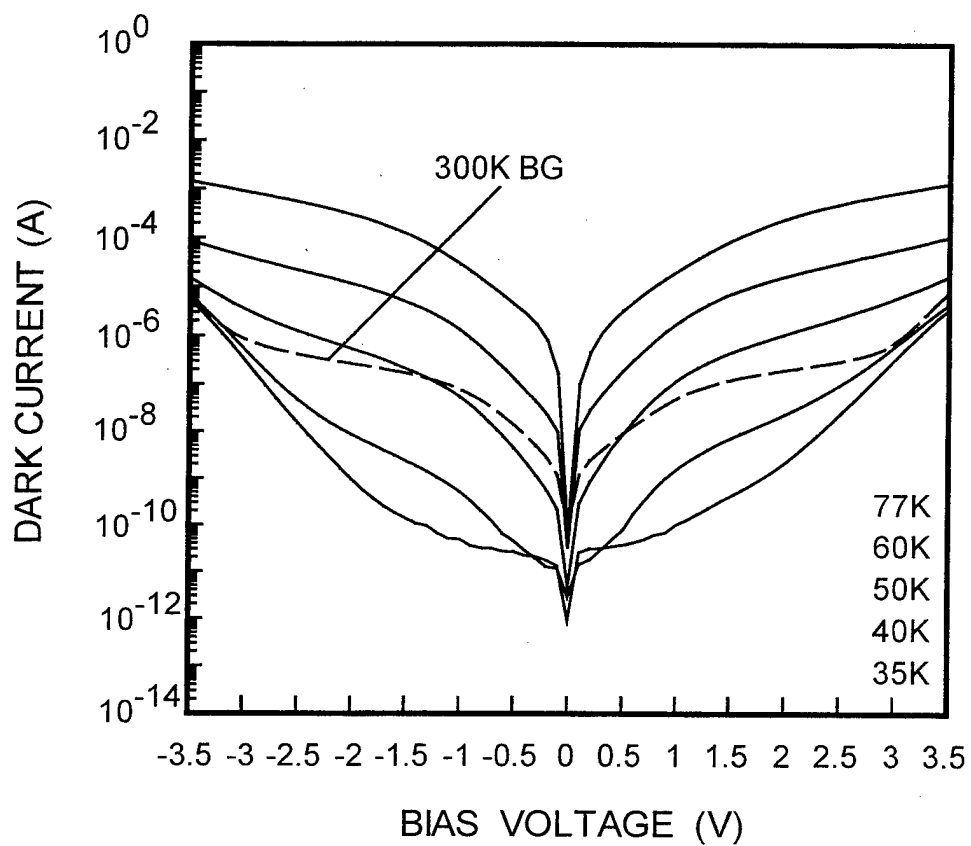
Figure 6.3 The dark current versus bias voltage (I-V) measured at T = 35, 40, 60, and 77K along with the 180° field of view (FOV) 300K background window current of the HS BC-QWIP.
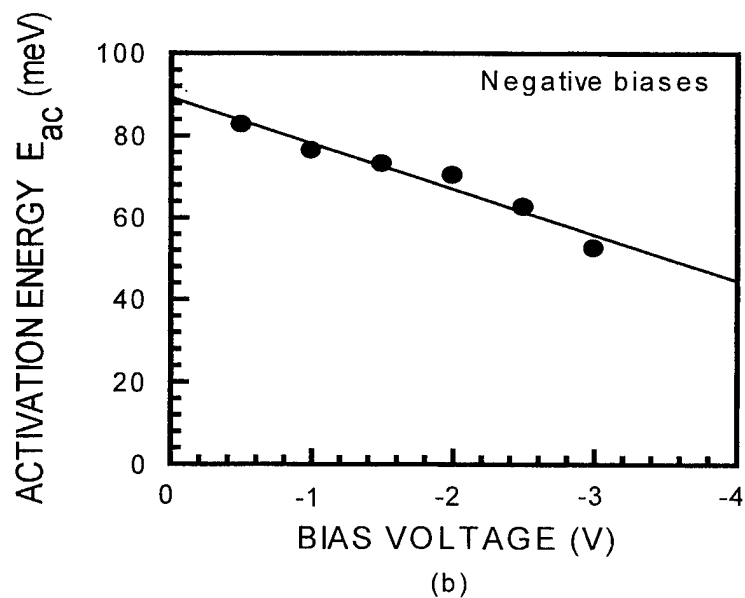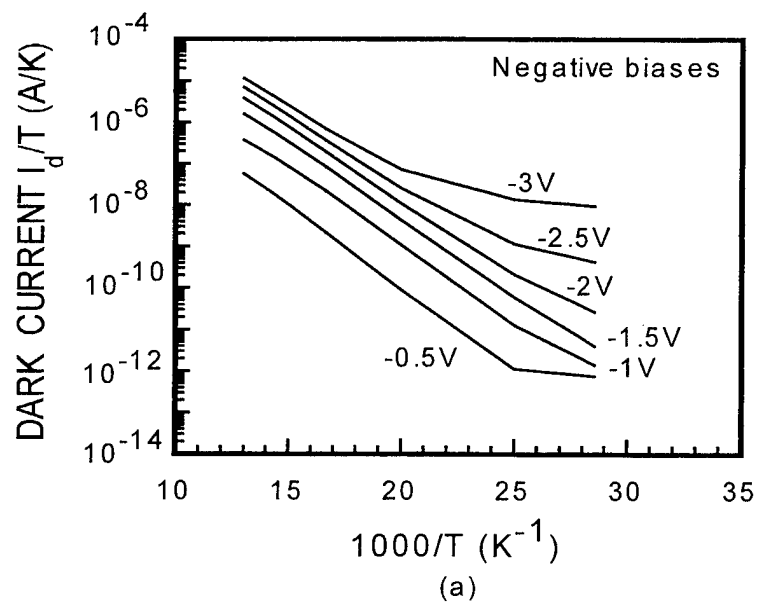
Figure 6.4 (a) The normalized dark current (I_d/T) versus inverse temperature (1000/T) and (b) the activation energy (E_{ac}) versus the applied negative bias voltage (the dots are the experimental data) for the HS BC-QWIP.

71
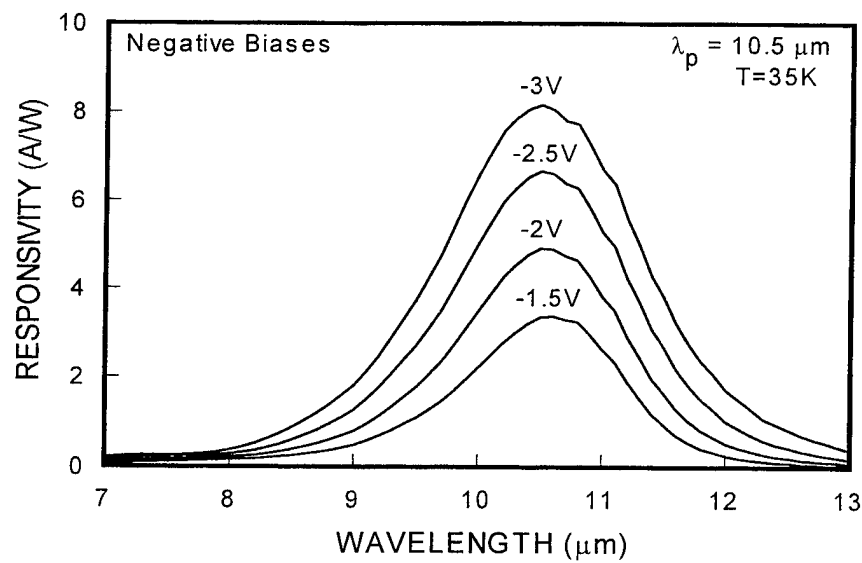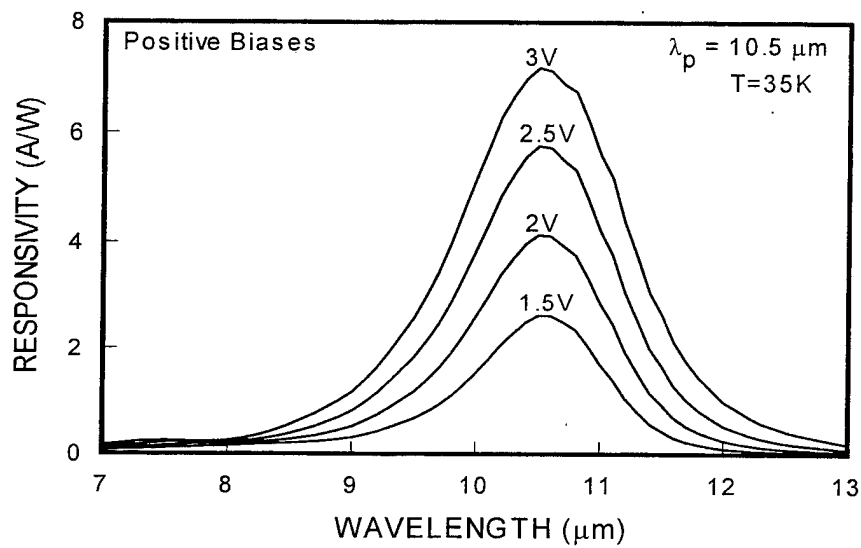
Figure 6.5 The spectral responsivity of HS BC-QWIP measured at T = 35K, (a) negative and (b) positive biases.
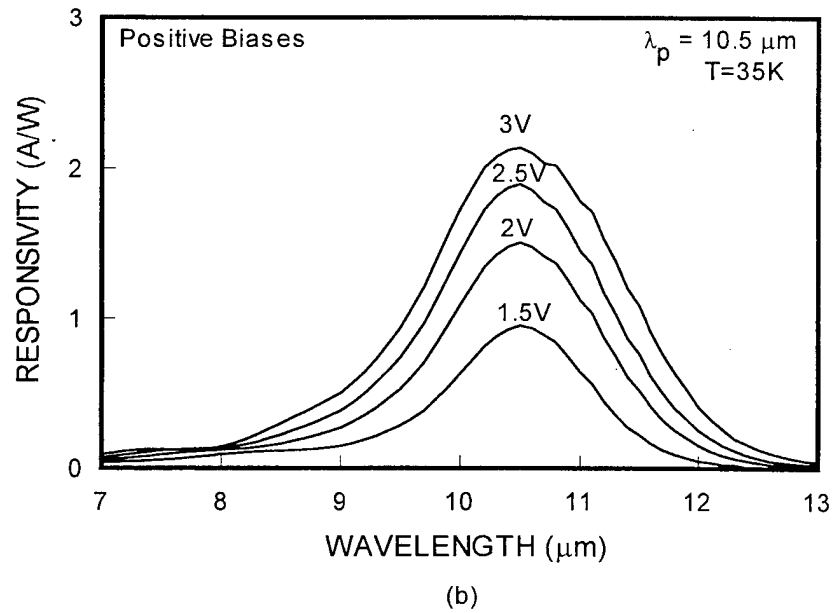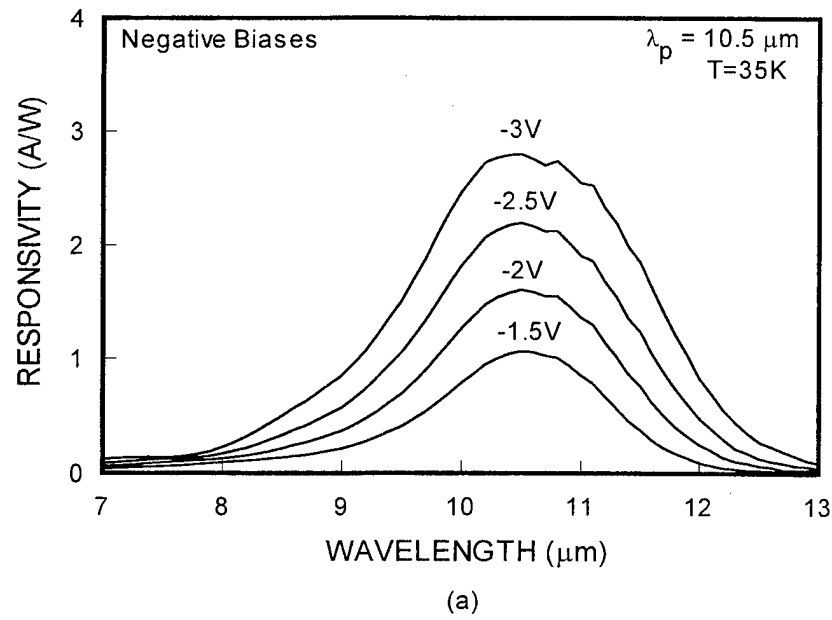
Figure 6.6 The spectral responsivity of HS BC-QWIP with 2-D square mesh metal grating coupler measured at T = 35K, (a) negative and (b) positive biases.

7 BROADBAND QUANTUM WELL INFRARED PHOTODETECTORS

7.1 Introduction

In the last few years, considerable interest has been directed towards the development of multicolor infrared photodetectors based on quantum well infrared photodetectors (QWIPs) for the 3-5 μm mid-wavelength infrared (MWIR) and 8-14 μm long-wavelength infrared (LWIR) applications [8,10,13,37,43-47]. Typical quantum well infrared photodetectors (QWIPs) exhibit rather narrow spectral bandwidths of one or two microns. However, for certain applications such as spectroscopy, it calls for the sensing of a broad range of infrared photons. Most multicolor QWIPs are composed of various QWIP layers with different detection peaks in series; which are sometimes separated by ohmic contact layers [13,39-41,44,45]. Recently, Bandara et al. [38] reported a broadband n-type QWIP sensitive in the 7-14 μm LWIR spectral range. In addition, the asymmetrical quantum well structure with the linear graded barrier has been reported for the broadband detection [41,42]. In this chapter, we report five new broadband (BB) QWIP designs for the broadband detection of LWIR radiation. This was achieved by using three to five quantum wells that have varying layer thickness or composition as a unit cell and repeating the unit cell to make up the BB-QWIP.

7.2 Layer Composition and Device Processing

The three well n-type BB-QWIP consists of an $In_{0.2}Ga_{0.8}As$ quantum well of 6.5 nm, an $In_{0.15}Ga_{0.85}As$ quantum well of 6.5 nm and an $In_{0.1}Ga_{0.9}As$ quantum well of 7.0 nm each separated by a 45 nm thick undoped $Al_{0.07}Ga_{0.93}As$ barrier. Each quantum well is Si-doped

to 7×10^{17} cm^{-3}. The complete unit cell of three quantum wells and barriers is then repeated 20 times and surrounded by a 300 nm thick of GaAs (Si doped to 3×10^{18} cm^{-3}) ohmic cap and a bottom buffer layer of similarly doped GaAs 500 nm thick. The schematic band diagram and complete layer structure for this QWIP are shown in Figure 7.1 (a) and (b), respectively. Figure 7.2 (a) and (b) show the schematic energy band diagram and complete layer structure of the four-well n-type BB-QWIP. This four-well n-type BB-QWIP consists of an In$_{0.3}$Ga$_{0.7}$As quantum well of 6.5 nm, an In$_{0.25}$Ga$_{0.75}$As quantum well of 6.5 nm, an In$_{0.2}$Ga$_{0.8}$As quantum well of 7.5 nm and an In$_{0.17}$Ga$_{0.85}$As quantum well of 8.5 nm all separated by 45 nm thick undoped barriers of GaAs. The quantum wells are doped with Si to a density of 7×10^{17} cm^{-3}, and the complete structure is then surrounded by extra undoped GaAs barriers 35 nm thick (to form an 80 nm thick blocking barrier) and 0.3 μm and 0.5 μm thick GaAs ohmic contacts doped with Si to 3×10^{18} cm^{-3}. The four-quantum well and barrier unit was repeated 20 times to create the whole stack. The five-well n-type BB-QWIP consists of an In$_{0.07}$Ga$_{0.93}$As quantum well (QW) of 8.5 nm, an In$_{0.1}$Ga$_{0.9}$As QW of 7.5 nm, an In$_{0.15}$Ga$_{0.85}$As QW of 6.5 nm, an In$_{0.18}$Ga$_{0.82}$As QW of 6.5 nm, and an In$_{0.22}$Ga$_{0.72}$As QW of 6.2 nm separated by a 45 nm thick undoped Al$_{0.07}$Ga$_{0.93}$As barrier in a unit cell. The first three In$_{0.07}$Ga$_{0.93}$As, In$_{0.1}$Ga$_{0.9}$As, and In$_{0.15}$Ga$_{0.85}$As QWs were Si-doped to 7×10^{17} cm^{-3} while the In$_{0.18}$Ga$_{0.82}$As and In$_{0.22}$Ga$_{0.72}$As QWs were Si-doped to 1×10^{18} cm^{-3}. The complete unit cell was repeated 3 times (top stack) and 7 times (bottom stack) in series to form a two-stack BB-QWIP structure on the same GaAs substrate. Finally, the ohmic contact layers (Si-doped to 3×10^{18} cm^{-3}) were grown on the top of the 3-period stack, on the bottom of the 7-period stack, and between

the two stacks. Figure 7.3 (a) and (b) show the schematic energy band diagram and complete layer structure of the five-well n-type BB-QWIP.

The variable composition p-type BB-QWIP is very similar to the three- well n-type BB-QWIP in operating principle, with variable material and layer thickness of the quantum well and barriers. The variable composition p-type BB-QWIP consists of an $In_{0.3}Ga_{0.7}As$ quantum well 5.0 nm thick, an $In_{0.25}Ga_{0.75}As$ quantum well 5.5 nm thick and an $In_{0.2}Ga_{0.8}As$ quantum well 6.0 nm thick each separated by a 40 nm thick undoped GaAs barrier. Each quantum well is Be-doped to $4x10^{18}$ cm^{-3}. The complete unit cell of the three- well and barriers is repeated 20 times and surrounded by an ohmic cap layer 300 nm thick of Be-doped GaAs ($p=4x10^{18}$ cm^{-3}) and a bottom buffer layer of similarly doped GaAs 500 nm thick. Figure 7.4 (a) and (b) show the schematic energy band diagram and the complete layer structure of the variable composition p-type BB-QWIP, respectively. Unlike the n-type devices, we were able to design another three- well p-type BB-QWIP to explore the effects of only varying the well thickness in the device design. This variable thickness p-type BB-QWIP design consists of three quantum wells of 4.5, 5.5 and 6.2 nm thick $In_{0.25}Ga_{0.75}As$ with Be- doped to $4x10^{18}$ cm^{-3}. The unit cell was separated by 40 nm thick undoped GaAs barriers, which was then repeated 20 times to form the absorber layers. The whole stack was then sandwiched by the 0.3 μm and 0.5 μm thick GaAs ohmic contacts with Be- doped to $4x10^{18}$ cm^{-3}. The schematic energy band diagram and the complete layer structure are shown in Figure 7.5 (a) and (b).

In order to characterize the devices, a wet chemical etch was used to create a 216x216 $μm^2$ mesa structure for the test devices. The Cr/Au was used to form the top and bottom

ohmic contacts for the p-type BB-QWIP. The AuGe/Ni/Au annealed at 450°C for two minutes was used as the top and bottom ohmic contacts for the three- and four-well n-type BB-QWIPs, while AuGe/Ag/Au ohmic contacts were evaporated with 10 seconds annealing at T = 450 °C for the five-well n-type BB-QWIPs. To facilitate normal incidence illumination for both the p-type and n-type BB-QWIPs, a ring contact around the mesa edge was used to allow light to pass through to most of the mesa top surface with a 75% fill factor. A 45° polished edge was also lapped in the n-type BB-QWIP so that 45° incident IR radiation could be used in the test devices. All of the devices were mounted on TO-8 chip carriers and wire bonds were attached ultrasonically for electrical connection.

7.3 Design Consideration

When $In_xGa_{1-x}As$ with high indium content (i.e., x > 20 %) was chosen for the QWs in the BB-QWIP design, one must take into account the effects of compressive strain on the QWIP layer structure. One important aspect that must not be overlooked in the design of reliable and functional p-QWIPs is the limitation to the epilayer thickness imposed by the induced biaxial compressive strain. If the intentionally introduced biaxial stress between the QW layers and the barrier layers is less than the biaxial stress needed for the given well thickness to become a critically thick layer, then pseudomorphic or coherent interfaces can be grown without the introduction of defects between the layers. Based on the force balance model [48-51], the equilibrium critical layer thickness, L_c, for an epilayer with the lattice constant a, grown on a substrate with lattice constant, a_s, is given as

$$L_C = \left(\frac{a}{\sqrt{2}\delta_o}\right)\frac{1 - \nu\cos^2\Theta}{8\pi(1 + \nu)\cos\alpha}\left[1 + \ln\left(l_q\sqrt{2}/a\right)\right] \qquad (7.1)$$

where l_q is the epilayer thickness, Θ is the angle between the dislocation line and the Burges' vector, α is the angle between the slip direction and the layer plane direction, δ_o is the lattice mismatch or the in-plane strain, and ν is the Poisson ratio. The Poisson ratio is defined as $\nu = -C_{12}/C_{11}$. In order to determine the detection peak wavelength of the QWIP we must first perform theoretical calculations of the intersubband transition energy. This can be achieved by using the transfer matrix method (TMM) [48]. The energy levels of the bound states in the QWs and the transmission coefficients for each intersubband transition can be determined from the TMM calculations for the BB-QWIPs. Since all the BB-QWIPs studied in this work use $In_xGa_{1-x}As$ for the QWs, we must also take into consideration the shifting of the energy subbands in the conduction and valence bands as a function of applied strain. If the QWIP structure is grown along the [100] direction and the strained-layer thickness is within the critical thickness, L_C, then a coherent heterointerface can be obtained, and the components of the strain tensor [e] are simplified to the expressions given by

$$e_{xx} = e_{yy} = e_\parallel$$

$$e_{zz} = -e_\parallel\left(\frac{2C_{12}}{C_{11}}\right) \qquad (7.2)$$

$$e_{xy} = e_{yz} = e_{zx} = 0 .$$

In addition to altering the physical parameters of the QWIP, lattice strain can also induce energy band shifts, which can be used to alter the absorption characteristics of the QWIP.

The strain induced energy band shifts in the conduction band, the heavy-hole and light-hole subbands can be approximated as follows

$$\Delta E_C = 2c_1 \frac{C_{11} - C_{12}}{C_{11}} \delta_0 \qquad (7.3)$$

$$\Delta E_{hh} = b \frac{C_{11} + C_{12}}{C_{11}} \delta_0 \qquad (7.4)$$

$$\Delta E_{lh} = -\Delta E_{hh} + \frac{(\Delta E_{hh})^2}{2\Delta_0} \qquad (7.5)$$

where c_1 is the combined hydrostatic deformation potential which characterizes the splitting of the Γ_8 valence band under strain, and b is the shear deformation potential, and Δ_0 is the spin orbit split-off energy [52]. The total hydrostatic deformation potential $c_1 + V_v$, where V_v is the valence band deformation potential, can be expressed by [53]

$$c_1 + V_v = -\frac{1}{3}(C_{11} + 2C_{12})\frac{dE_g^0}{dP}, \qquad (7.6)$$

where dE^0_g/dP is the unstrained energy band gap change with respect to the unit pressure. The effect of strain on the energy band structure results in the splitting of the heavy-hole and light-hole band at the valence band zone center [54] (i.e., the in-plane wave vector $k_\parallel$ = 0), which is degenerate in the unstrained case. When tensile strain is applied between the QW and the barrier layers [55-57] along the superlattice growth z-direction, the strain can push the light-hole levels upwards and pull the heavy- hole levels downwards. We can therefore expect heavy- hole and light-hole states to invert at a specific lattice strain and QW thickness. This phenomenon will in turn cause the intersubband transitions in a QWIP structure to take place from the populated light-hole ground state to the upper

energy band states. Since the light- hole has a smaller effective mass (comparable to the electron effective mass), the optical absorption and spectral responsivity in the strained layer *p*-type QWIP can be greatly enhanced, as a result of introducing strain in the QW. In addition to the utilization of the light-hole states with small effective masses, certain heavy-hole states under the compressive-strain may also have similar characteristics, such as higher mobility, smaller effective mass, and longer mean free path, which in turn favorably alter the intersubband absorption and transport characteristics, as shown by Hirose, *et al.* [58]. This is achieved by distorting the heavy-hole valence band at and near the zone center via the introduction of compressive strain in the QW.

7.4 Characterization Results and Discussion

First, we will discuss the results of three-, four-, and five-well n-type BB-QWIPs. The next subsection will cover the two p-type BB-QWIPs in this order, the variable composition three- well p-type BB-QWIP and then the variable thickness p-type BB-QWIP. The responsivity was measured using a blackbody source set at 1273 K, running through a 1/8m monochrometer with the appropriate filters as the source of IR radiation, which is also chopped at a given frequency. The device is mounted in a closed cycle liquid helium cryo-system. The output of the device is then amplified by a trans-impedance amplifier (TIA) with a gain of 10^6 V/A. The output of the TIA is then sent to a lock-in amplifier to determine the phase and magnitude of the output signal. The relative responsivity curve is then normalized against the response of a pyroelectric detector to determine the absolute responsivity.

7.4.1 N-type Broadband QWIPs

As shown in Figure 7.6, the n-type three-well BB-QWIP exhibits a large responsivity peak at 10 μm. This is in excellent agreement with the predicted peak response by TMM [9] at 9.7 μm. As can be seen in this figure, when the bias is increased the absolute responsivity also increases rapidly. A maximum responsivity value of 1.90 A/W was obtained at T=40 K, V_b=+6 V, with 45° facet illumination. It is also interesting to note that the bandwidth of the responsivity increases with increasing bias voltage under negative bias condition. For example, the full-width half-maximum (FWHM) spectral bandwidth of the device at V_b=+4 V is $\Delta\lambda/\lambda_p$=13%, while the bandwidth at V_b=-4 V is $\Delta\lambda/\lambda_p$=18%. Figure 7.7 shows the responsivity of the n-type BB-QWIP at lower applied biases. Here we see that the bandwidth of the device at $|V_b|$<2 V, is very broad with a maximum value of $\Delta\lambda/\lambda_p$=21% at V_b=-2 V, and a responsivity of 58 mA/W at 10 μm. It is interesting to note that the relative responsivity of the shorter and the longer wavelength quantum wells covers a larger proportion of the peak responsivity at the low bias levels than at higher (*e.g.*, V_b>4 V) biases. Also note the very broad responsivity curve of the n-type BB-QWIP at V_b=-1 V. The calculated spectral bandwidth at V_b=-1 V is $\Delta\lambda/\lambda_p$=40%. The responsivity at λ_p=10 μm is 5 mA/W. However, due to the very low dark current (I_{dk}=50 nA) at this bias, the detectivity is expected to be on the order of 10^{10} cm-Hz$^{1/2}$/W. A normal incidence response of approximately 50% of the 45° value was found for this device under all of the biases tested. Figure 7.8 shows the dark current as a function of applied bias and device temperature, with the 300 K background photocurrent at a field-of-view of 180° superimposed. Note that at 60 K the device is under

background limited performance (BLIP) when the applied bias is between ±5V. The device is under BLIP at 70 K for -1 V<V_b<0 V. Comparing figures 7.9 (a) and (b), the most striking feature of the results of the four- well n-type BB-QWIP is that the FWHM bandwidth is drastically increased, especially in the negative bias case. In figure 7.9 (b), we find that $\Delta\lambda/\lambda_p$=29% with a λ_p=10.3 μm at V_b=-4 V. The spectral bandwidth achieved is almost twice that of the three - well n-type BB-QWIP. It is also interesting to note the increasing dominance of the 12 μm peak at higher negative biases, which significantly contributes to the flatness of the responsivity curve for V_b≥-4 V. As shown in Figure 7.10 (a), we also observed a normal incidence response of this device of up to 60% of the 45° facet values. Figure 7.10 (b) shows the measured dark *I-V* curves of the four- well n-type BB-QWIP. Note the nearly complete symmetry dark I-V characteristics under negative and positive biases. The larger dark current of the four - well device when compared to the three- well device is attributed to the lower barrier height of the longest wavelength well in the four- well n-type BB-QWIP, when compared with the longest wavelength well of the three- well BB-QWIP. Comparing with the three- well n-type BB-QWIP, the BLIP operating temperature of this device is predicted to be around 50 K. Figure 7.11 shows the dark current versus bias voltage (I-V) curves of the 3-period five-well BB-QWIP measured at T = 40, 50, 60,and 77K along with the 300 K background window current at 180° field of view (FOV). The 3-period five-well BB-QWIP is under background limited performance (BLIP) when the applied bias is between –3V and 3V at T = 40K, and between –1.2V and +1.2V at T = 50K. Figure 7.12 shows the measured dark current of the 7-period five-well BB-QWIP as a function of the applied bias voltage

at T = 40, 50, 60, and 77K along with the 300 K background window current at 180° field of view (FOV). The 7-period five-well BB-QWIP is under background limited performance (BLIP) between –2.2V and +2.1V at T = 50K. The dark I-V curves of the 7-period device show a similar behavior as those of the 3-period BB-QWIP.

The spectral response was measured at T = 40 K for both the 3-period and the 7-period five-well BB-QWPs. Figure 7.13 (a) and (b) show the spectral responsivity of the 3-period five-well BB-QWIP measured at different bias voltages and T = 40K. The detection scheme for this device is based on the bound-to-quasi-bound intersubband transition. As seen in Figure 7.13, the absolute responsivity was increased rapidly when the applied bias was increased. It is interesting to note that the relative responsivity of the shorter wavelength quantum well dominates a larger portion of the peak responsivity at smaller negative biases ($V_b \leq$ -1.75V) than at higher negative biases, while the detection of the longer wavelength quantum well is more noticeable at smaller positive biases ($V_b \leq$ 1.75V) than at higher positive biases. The maximum responsivity was 1.28 A/W at V_b = -2V and λ_p = 10.2 μm. The spectral responsivity of the 3-period five-well BB-QWIP was relatively flat at lower positive biases ($V_b \leq$ 1.5V). The full-width half-maximum (FWHM) spectral bandwidth of the 3-period five-well BB-QWIP was increased with increasing bias voltage at both negative and positive bias voltages. The calculated spectral bandwidth at V_b = 2V is $\Delta\lambda/\lambda_p$ = 28 % while the bandwidth at V_b = -2V is $\Delta\lambda/\lambda_p$ = 24 %. The 7-period five-well BB-QWIP photoresponse was also measured at different bias voltages and T = 40K. Figure 7.14 shows the spectral responsivity of the 7-period five-well BB-QWIP under (a) negative and (b) positive biases. Under negative biases, the

peak responsivity wavelength was shifted with the increasing bias voltage from the shorter wavelength range to the longer wavelength range while this trend was reversed under positive biases as observed in the 7-period five-well BB-QWIP. The maximum responsivity was 1.16 A/W at V_b = -4.5V and λ_p = 10.5 μm. The full-width half-maximum (FWHM) spectral bandwidth of the 7-period five-well BB-QWIP was increased with increasing bias voltage at both polarity biases and narrower under negative biases than under positive biases. The calculated spectral bandwidth at V_b = 4.5V is $\Delta\lambda/\lambda_p$ = 26 % while the bandwidth at V_b = -4.5V is $\Delta\lambda/\lambda_p$ = 23 %, which are nearly independent of the QW period. The dependence of responsivity on the QW period was studied as a function of the applied electric field. Figure 7.15 (a) and (b) show the peak responsivity versus electric field, and the responsivity versus electric field at a fixed wavelength (λ = 10.2 μm), respectively. The results reveal that the responsivity of the 3-period BB-QWIP was larger than that of the 7-period BB-QWIP at high electric field, while the responsivity at low electric field was found to be nearly independent of the device period. The background limited performance (BLIP) detectivities (D^*_{BLIP}) for both the 3-period and the 7-period five-well BB-QWIPs were found to be 1.36 x 10^{10} cm-$Hz^{1/2}$/W at λ_p = 9.6 μm, V_b = 2V and T = 40K, and 1.27 x 10^{10} cm-$Hz^{1/2}$/W at λ_p = 9.9 μm, V_b = 4.5V and T = 40K, respectively.

7.4.2 P-type Broadband QWIPs

Next, we will discuss the results of the p-type BB-QWIPs. Figure 7.16 shows the absolute responsivity as a function of applied bias and incident IR radiation wavelength. This p-type BB-QWIP has a response peak at 9.3 μm, with a maximum responsivity of

19 mA/W at T=40 K and V_b=-1.5 V. Also under the previously stated operating conditions, the FWHM spectral bandwidth is $\Delta\lambda/\lambda_p$=48%. The half peak range is from 7 to 11.2 μm. The peak responsivity was found to increase linearly with applied bias under negative bias condition. In contrast to the responsivity curve exhibited by the n-type BB-QWIP, the p-type BB-QWIP does not seem to have a large variation of spectral bandwidth as a function of applied bias. For example, the bandwidth of the device at low (V_b=-0.5 V) biases was found very broad with $\Delta\lambda/\lambda_p$=48%. However, this device does not exhibit the large increase in responsivity at high biases as in the case of the n-type BB-QWIP. All of the responsivity measurements were made by illuminating the top ring contact with IR light for normal incidence, and the IR radiation is considered to have only pass through the layer structure once. As can be seen in Figure 7.17, the dark current increases as the device temperature is increased, and there is dopant migration effect which is illustrated by the asymmetrical nature of the dark I-V characteristic. In Figure 7.18 (a) and (b) we see the variation of responsivity as a function of applied bias and incident radiation wavelength at T=40 K for the variable thickness p-type BB-QWIP. This p-type BB-QWIP has a response peak at λ_p=9.6 μm with a corresponding FWHM bandwidth of $\Delta\lambda/\lambda_p$=63% under all applied biases from 6.5 to 12.5 μm wavelength range. A maximum responsivity of 25 mA/W was obtained under normal incidence single pass illumination at V_b=+1.1 V. Also can be seen in these figures, there is a slight PV response with a peak at 10.2 μm. Figure 7.19 shows the dark I-V characteristic of the variable thickness p-type BB-QWIP as a function of device temperature. When comparing the two p-type BB-QWIPs, we see that the variable thickness p-type BB-QWIP has higher

responsivity with a longer peak wavelength and a significantly larger FWHM spectral bandwidth.

7.5 Conclusions

We have demonstrated five quantum well infrared photodetectors which exhibit broad spectral response bandwidths. The three- well n-type BB-QWIP was found to have a response peak at 10 μm, with a FWHM bandwidth that varies as a function of applied bias polarity and magnitude. The maximum bandwidth of $\Delta\lambda/\lambda_p$=21% was obtained at V_b=-2 V, with a peak responsivity of 58 mA/W, whereas the minimum bandwidth of $\Delta\lambda/\lambda_p$=12% was observed at V_b=6 V, with a peak responsivity of 1.90 A/W at this bias. It is interesting to note that the two other response peaks predicted and seen in this device do not seem to exhibit nearly as much responsivity as the 10 μm peak at higher biases ($|V_b|$>3 V). The four - well n-type BB-QWIP not only exhibits a very large responsivity of 2.35 A/W at 10.3 μm and V_b=+4.5 V, but also shows a broad bandwidth of $\Delta\lambda/\lambda_p$=29% which extended from 9.5 to 12.5 μm. It is possible to flatten out the responsivity curve of both n-type BB-QWIPs by tailoring the grating period and dimension used to couple normal incidence radiation so that the shorter wavelengths are enhanced. For the 3-period five-well BB-QWIP, the maximum bandwidth and the background limited performance (BLIP) detectivity (D*$_{BLIP}$) were found to be $\Delta\lambda/\lambda_p$ = 28 % and 1.36 x 10^{10} cm-Hz$^{1/2}$/W at V_b = 2V with a 1.05 A/W peak responsivity at λ_p = 9.6 μm. The peak responsivity for the 7-period five-well BB-QWIP was 1.16 A/W at V_b = -4.5V, λ_p = 10.5 μm, and T =40K. The corresponding D*$_{BLIP}$ was found to be 1.3 x 10^{10}

cm-Hz$^{1/2}$/W. It is noted that the device performance was found to be nearly independent of the BB-QWIP period. The variable composition p-type BB-QWIP was found to have a very large FWHM bandwidth of $\Delta\lambda/\lambda_p$=48% at T=40 K and V_b=-1.5 V. Under similar condition, the variable thickness p-type BB-QWIP was found to have an even larger FWHM bandwidth of $\Delta\lambda/\lambda_p$=63% at T=40 K and V_b=+1.1 V, with a corresponding peak responsivity of 25 mA/W at 10.2 μm. Comparing the two p-type BB-QWIPs, the variable thickness p-type BB-QWIP has better performance in terms of responsivity and FWHM bandwidth. When comparing the n- and p-type BB-QWIPs, we see that if the responsivity bandwidth is the dominant factor then a p-type BB-QWIP would be the detector of choice. But if the absolute responsivity is the most important consideration, then the obvious choice would be one of the n-type BB-QWIPs.

$In_{0.1}Ga_{0.9}As$ $In_{0.15}Ga_{0.85}As$ $In_{0.2}Ga_{0.8}As$
$Al_{0.07}Ga_{0.93}As$ $Al_{0.07}Ga_{0.93}As$

7.5 nm   6.5 nm   6.5 nm E_c

E1   E1   E1

11.8 um   9.7 um   8.2 um

(a)
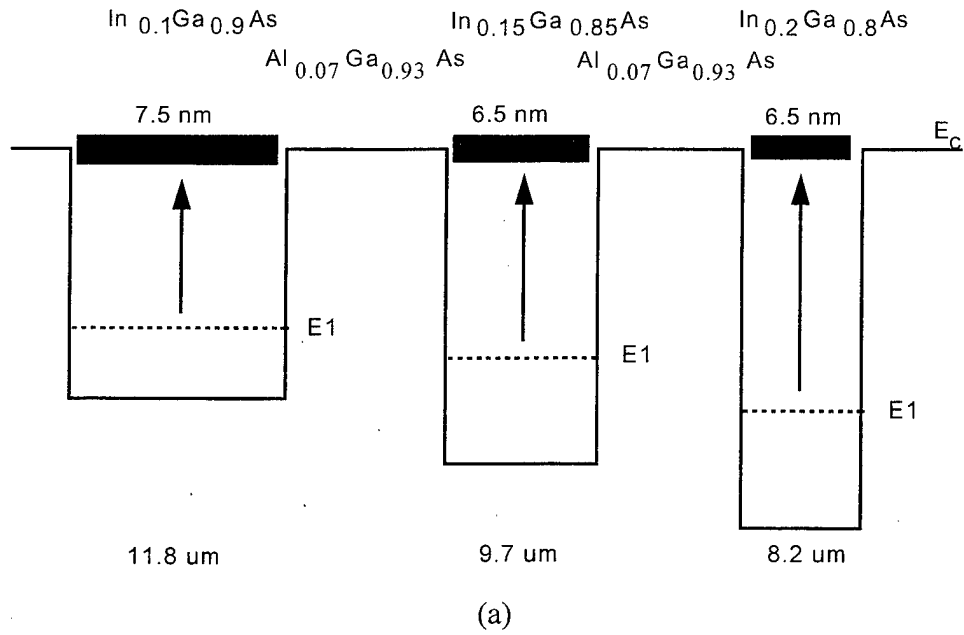
Layer		Thickness (Å)	Dopant	Concentration (cm^{-3})
n GaAs (top contact)		3000	Si	$3x10^{18}$
i $Al_{0.07}Ga_{0.93}As$		450	none	none
n $In_{0.2}Ga_{0.8}As$		65	Si	$7x10^{17}$
i $Al_{0.07}Ga_{0.93}As$		450	none	none
n $In_{0.15}Ga_{0.85}As$	X 20	65	Si	$7x10^{17}$
i $Al_{0.07}Ga_{0.93}As$		450	none	none
n $In_{0.1}Ga_{0.9}As$		70	Si	$7x10^{17}$
i $Al_{0.07}Ga_{0.93}As$		450	none	none
n GaAs (bottom contact)		5000	Si	$3x10^{18}$
S.I. GaAs substrate		625 ± 25 μm	none	none

(b)

Figure 7.1 (a) The schematic energy band diagram and (b) the complete layer structure for the three - well n-type InGaAs/AlGaAs BB-QWIP.

In$_{0.17}$Ga$_{0.83}$As   In$_{0.2}$Ga$_{0.8}$As   In$_{0.25}$Ga$_{0.75}$As   In$_{0.3}$Ga$_{0.7}$As

GaAs   GaAs   GaAs

8.5 nm   7.5 nm   6.5 nm   6.5 nm   E$_c$

E1

E1

E1

E1

(a)

Layer		Thickness (Å)	Dopant	Concentration (cm^{-3})
n GaAs (top contact)		3000	Si	3×10^{18}
i GaAs		350	none	none
i GaAs		450	none	none
n In$_{0.3}$Ga$_{0.7}$As		65	Si	7×10^{17}
i GaAs		450	none	none
n In$_{0.25}$Ga$_{0.75}$As	X 20	65	Si	7×10^{17}
i GaAs		450	none	none
n In$_{0.2}$Ga$_{0.8}$As		75	Si	7×10^{17}
i GaAs		450	none	none
n In$_{0.17}$Ga$_{0.83}$As		85	Si	7×10^{17}
i GaAs		800	none	none
n GaAs (bottom contact)		5000	Si	3×10^{18}
S.I. GaAs substrate		625 ± 25 μm	none	none

(b)

Figure 7.2 (a) The schematic energy band diagram and (b) the complete layer structure for the four- well n-type InGaAs/GaAs BB-QWIP.

$Al_{0.07}Ga_{0.93}As$

8.5 nm   7.5 nm   6.5 nm   6.5 nm   6.2 nm

E_c

E_1

$In_{0.07}Ga_{0.93}As$

E_1

$In_{0.1}Ga_{0.9}As$

E_1

$In_{0.15}Ga_{0.85}As$

E_1

$In_{0.18}Ga_{0.82}As$

E_1

$In_{0.22}Ga_{0.78}As$

(a)

Figure 7.3 (a) The schematic energy band diagram and (b) the complete layer structure for the five-well n-type InGaAs/GaAs BB-QWIP.

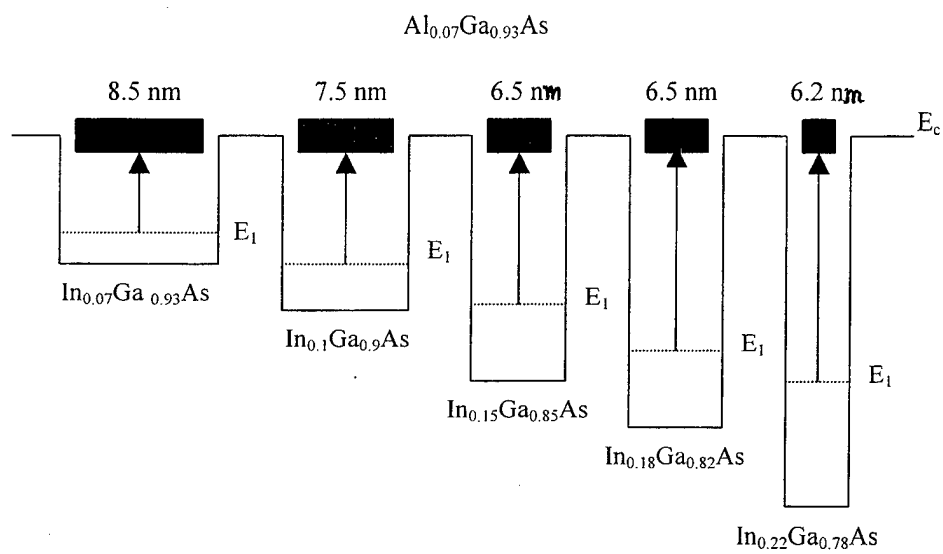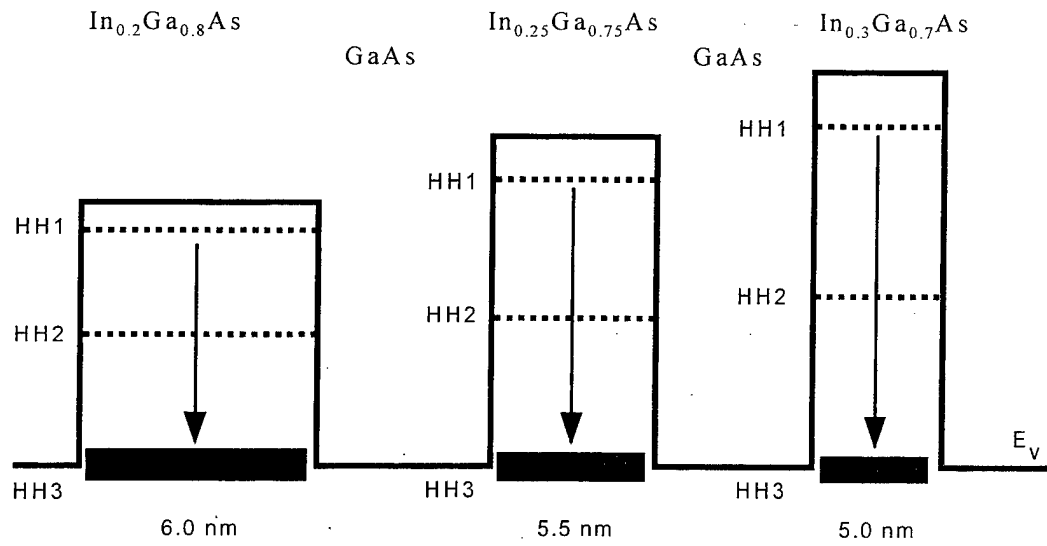| Layer		Thickness (Å)	Dopant	Concentration (cm^{-3})
n GaAs (top contact)		3000	Si	3×10^{18}
i Al$_{0.07}$Ga$_{0.93}$As		450	none	none
n In$_{0.22}$Ga$_{0.78}$As		62	Si	1×10^{18}
i Al$_{0.07}$Ga$_{0.93}$As		450	none	none
n In$_{0.18}$Ga$_{0.82}$As		65	Si	1×10^{18}
i Al$_{0.07}$Ga$_{0.93}$As	3-period	450	none	none
n In$_{0.15}$Ga$_{0.85}$As		65	Si	7×10^{17}
i Al$_{0.07}$Ga$_{0.93}$As		450	none	none
n In$_{0.1}$Ga$_{0.9}$As		75	Si	7×10^{17}
i Al$_{0.07}$Ga$_{0.93}$As		450	none	none
n In$_{0.07}$Ga$_{0.93}$As		85	Si	7×10^{17}
i Al$_{0.07}$Ga$_{0.93}$As		450	none	none
n GaAs		5000	Si	3×10^{18}
i Al$_{0.07}$Ga$_{0.93}$As		450	none	none
n In$_{0.22}$Ga$_{0.78}$As		62	Si	1×10^{18}
i Al$_{0.07}$Ga$_{0.93}$As		450	none	none
n In$_{0.18}$Ga$_{0.82}$As		65	Si	1×10^{18}
i Al$_{0.07}$Ga$_{0.93}$As	7-period	450	none	none
n In$_{0.15}$Ga$_{0.85}$As		65	Si	7×10^{17}
i Al$_{0.07}$Ga$_{0.93}$As		450	none	none
n In$_{0.1}$Ga$_{0.9}$As		75	Si	7×10^{17}
i Al$_{0.07}$Ga$_{0.93}$As		450	none	none
n In$_{0.07}$Ga$_{0.93}$As		85	Si	7×10^{17}
i Al$_{0.07}$Ga$_{0.93}$As		450	none	none
n GaAs		5000	Si	3×10^{18}
S.I. GaAs substrate		625 ± 25 μm	none	none

(b)

Figure 7.3 (continued)

$In_{0.2}Ga_{0.8}As$ $In_{0.25}Ga_{0.75}As$ $In_{0.3}Ga_{0.7}As$

GaAs   GaAs

HH1   HH1   HH1

HH2   HH2   HH2

E_v

HH3   HH3   HH3

6.0 nm   5.5 nm   5.0 nm

(a)

Layer		Thickness (Å)	Dopant	Concentration (cm^{-3})
n GaAs (top contact)		3000	Be	4×10^{18}
i GaAs	X 20	400	none	none
n $In_{0.3}Ga_{0.7}As$		50	Be	4×10^{18}
i GaAs		400	none	none
n $In_{0.25}Ga_{0.75}As$		55	Be	4×10^{18}
i GaAs		400	none	none
n $In_{0.2}Ga_{0.8}As$		60	Be	4×10^{18}
i GaAs		400	none	none
n GaAs (bottom contact)		5000	Be	4×10^{18}
S.I. GaAs substrate		625 ± 25 μm	none	none

(b)

Figure 7.4 (a) The schematic energy band diagram and (b) the complete layer structure for the variable composition p-type BB-QWIP.
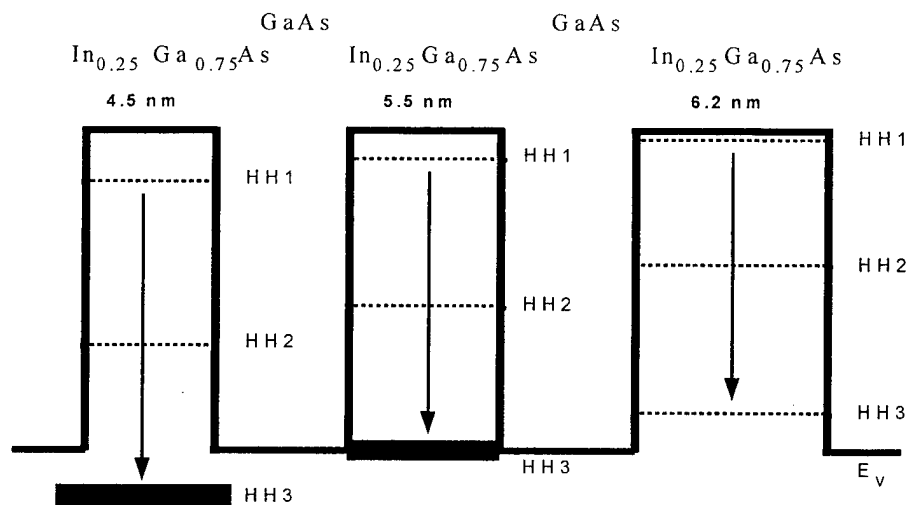
(b)

Layer		Thickness (Å)	Dopant	Concentration (cm^{-3})
n GaAs (top contact)		3000	Be	4×10^{18}
i GaAs		400	none	none
n In$_{0.25}$Ga$_{0.75}$As		45	Be	4×10^{18}
i GaAs	X 20	400	none	none
n In$_{0.25}$Ga$_{0.75}$As		55	Be	4×10^{18}
i GaAs		400	none	none
n In$_{0.25}$Ga$_{0.75}$As		62	Be	4×10^{18}
I GaAs		400	none	none
n GaAs (bottom contact)		5000	Be	4×10^{18}
S.I. GaAs substrate		625 ± 25 μm	none	none

(b)

Figure 7.5 (a) The schematic energy band diagram and (b) the complete layer structure for the variable thickness p-type BB-QWIP.
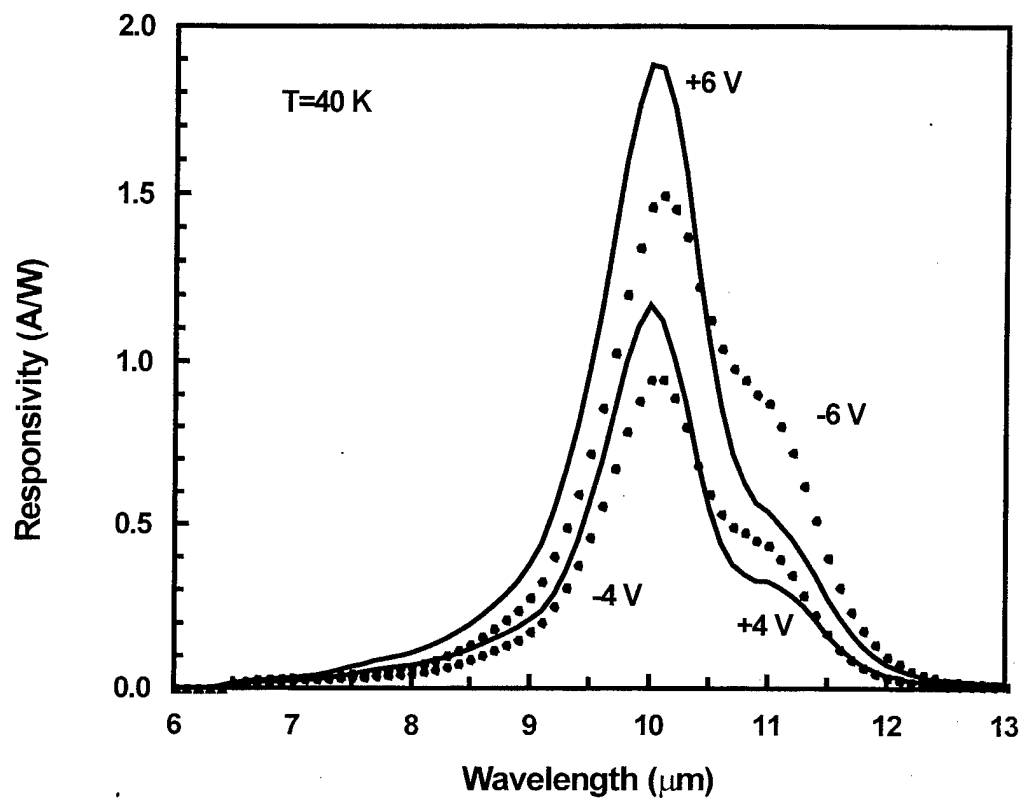
Figure 7.6 The measured absolute responsivity for the n-type three- well BB-QWIP as a function of applied bias and incident IR wavelength at T=40 K. The responsivity is measured through a 45° facet.
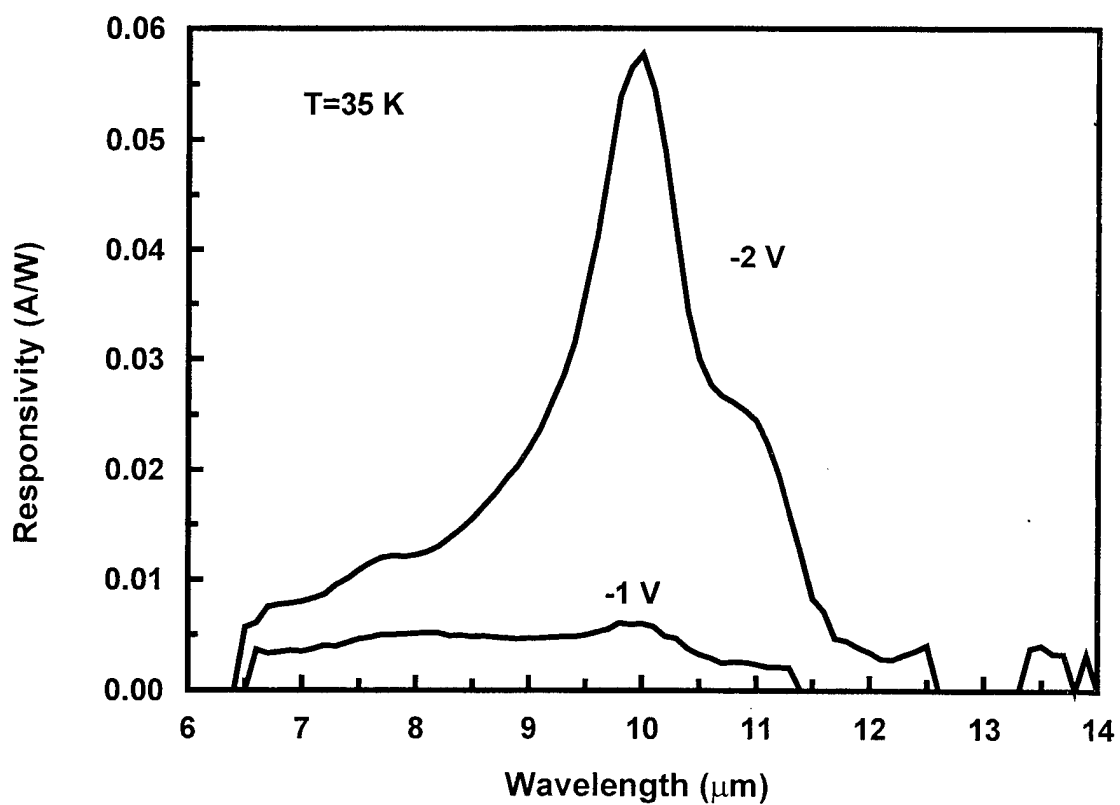
Figure 7.7   The responsivity of the n-type three- well BB-QWIP at low ($|V_b|{\leq}2$ V) applied biases.
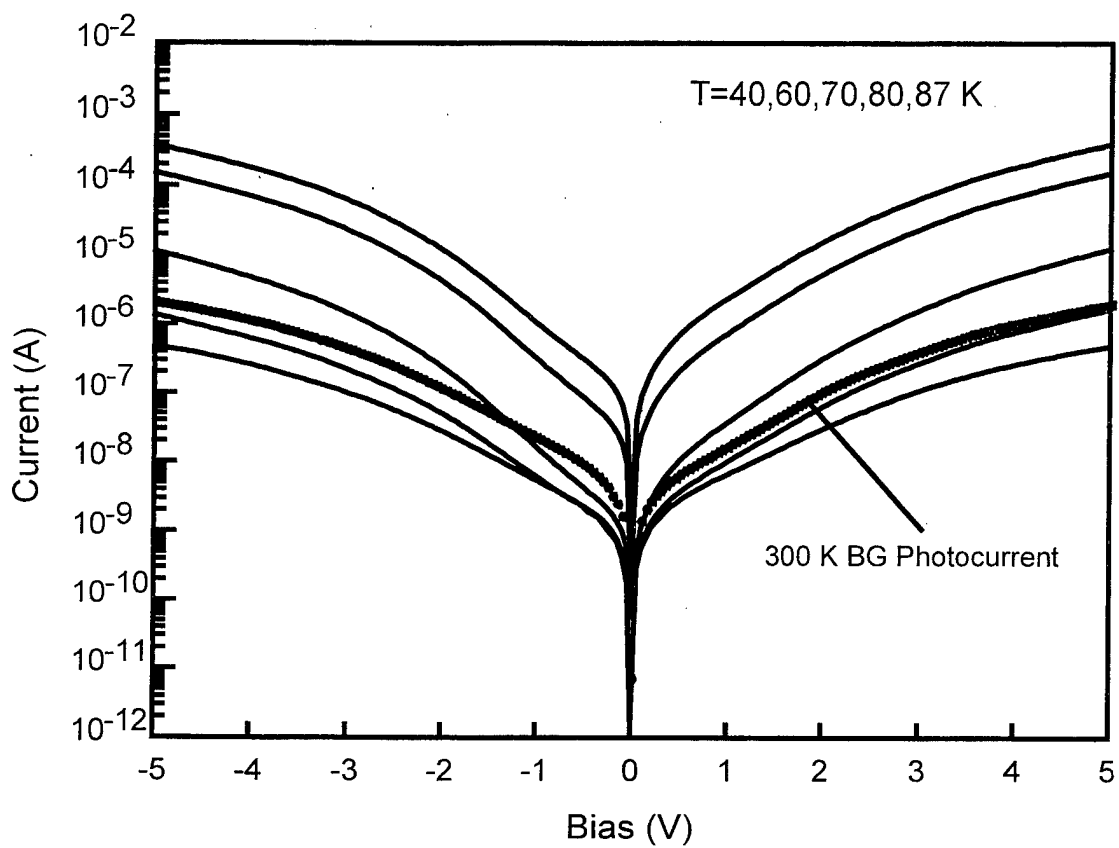
Figure 7.8 Measured dark I-V characteristics of the n-type three- well BB-QWIP with the 300 K background photocurrent superimposed. The FOV=180° for the 300K background photocurrent.
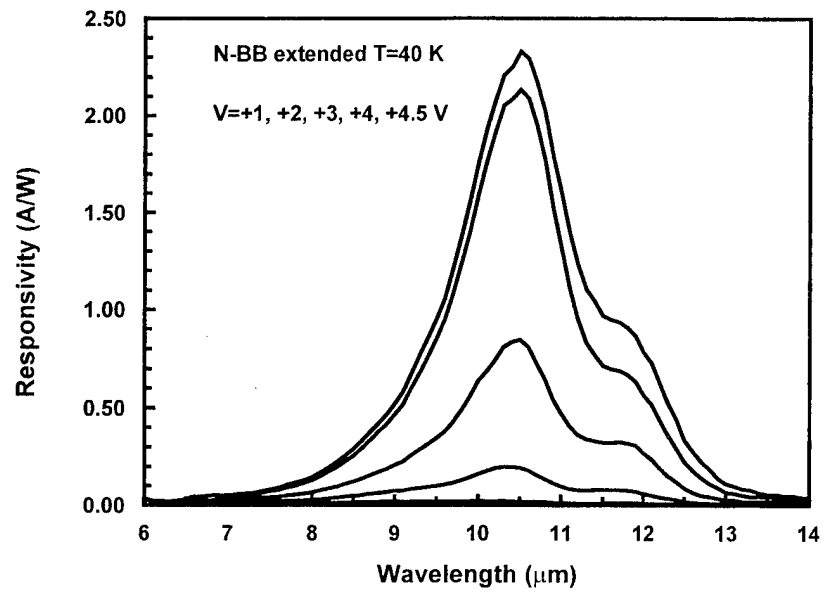
(a)
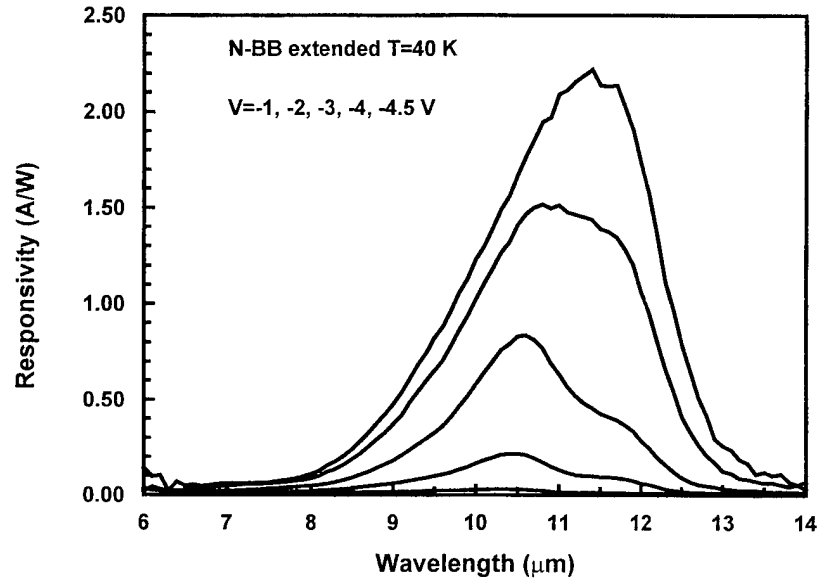
(b)

Figure 7.9 The measured 45° responsivity at (a) positive and (b) negative bias for the four - well n-type BB-QWIP.

97
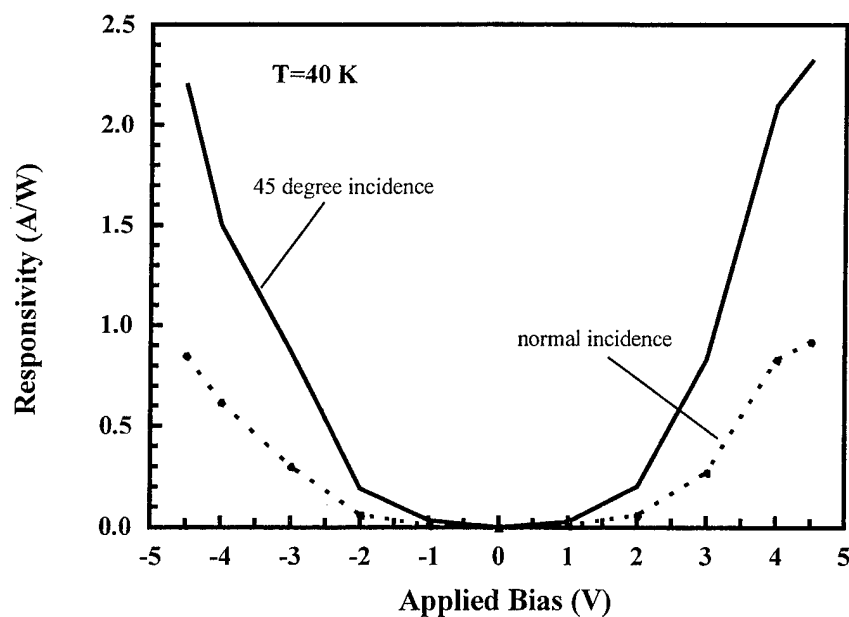
(a)
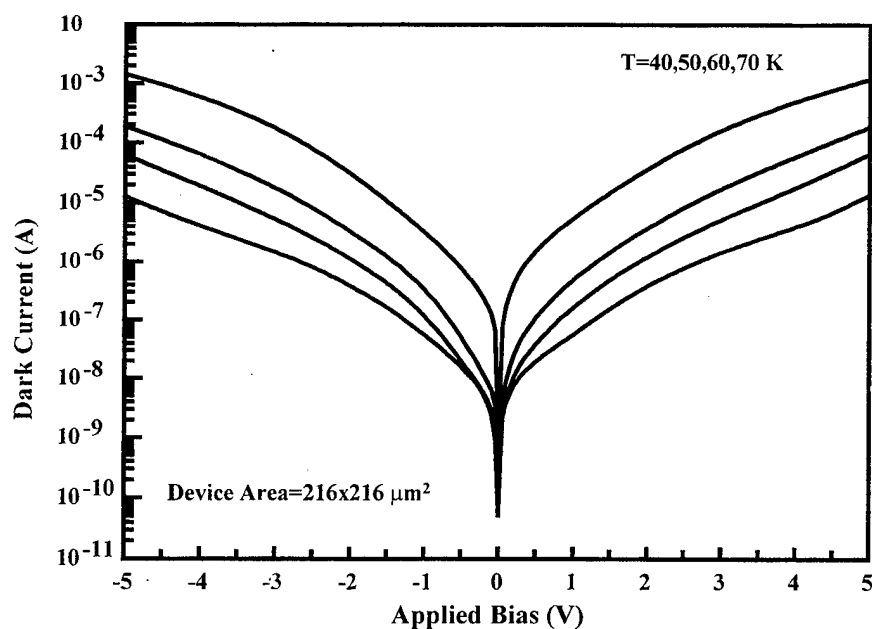
(b)

Figure 7.10 (a) The normal incidence responsivity as a function of applied bias compared with the 45° responsivity and (b) the measured dark I-V curves of the four -well n-type BB-QWIP.
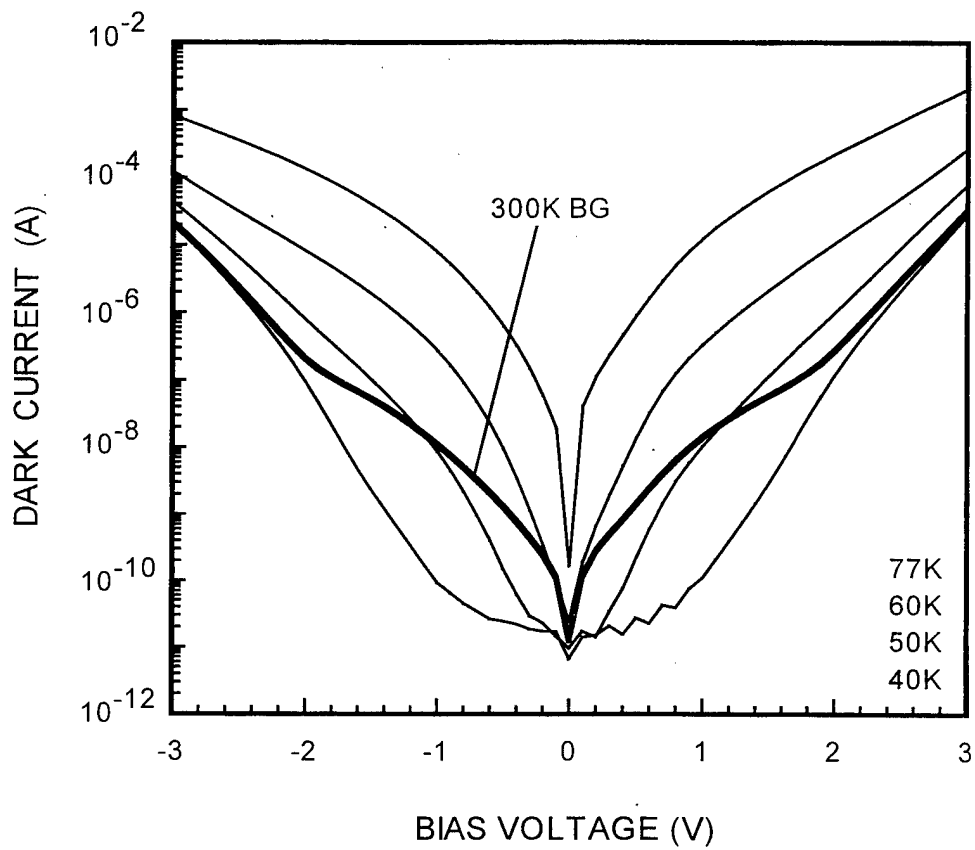
Figure 7.11 The dark current versus bias voltage (I-V) measured at T = 40, 50, 60, and 77K along with 180° field of view (FOV) 300K background window current of the 3-period BB-QWIP

99
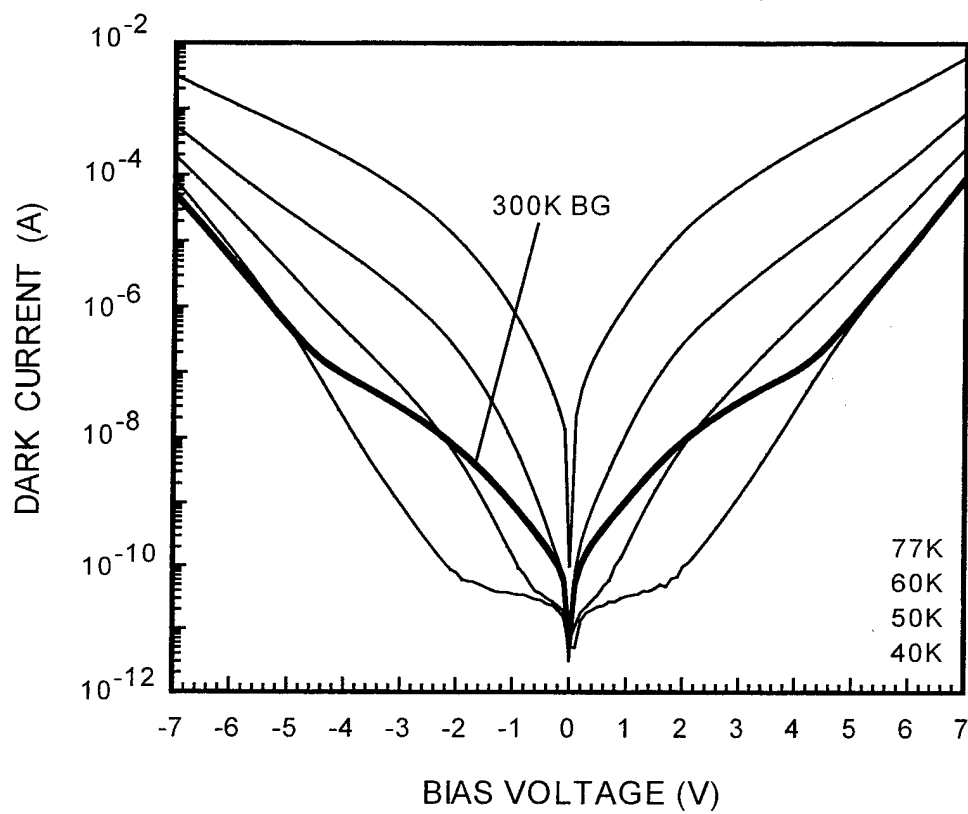
Figure 7.12 The dark current versus bias voltage (I-V) measured at T = 40, 50, 60, and 77K along with 180° field of view (FOV) 300K background window current for the 7-period BB-QWIP
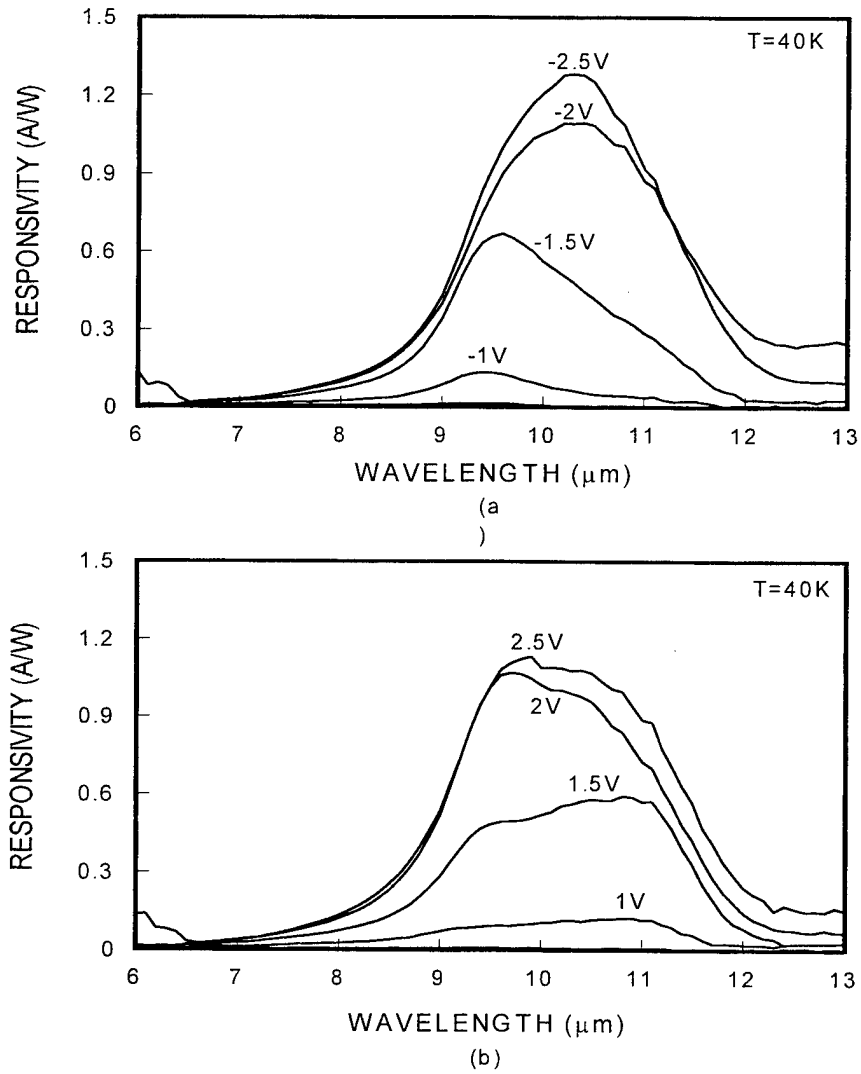
Figure 7.13 The spectral responsivity of the 3-period BB-QWIP measured at T = 40K, under (a) negative and (b) positive bias conditions.
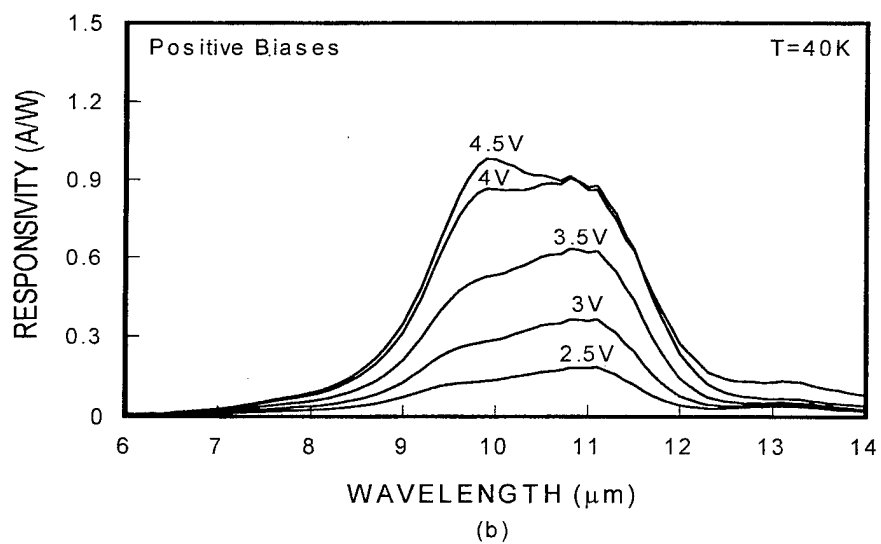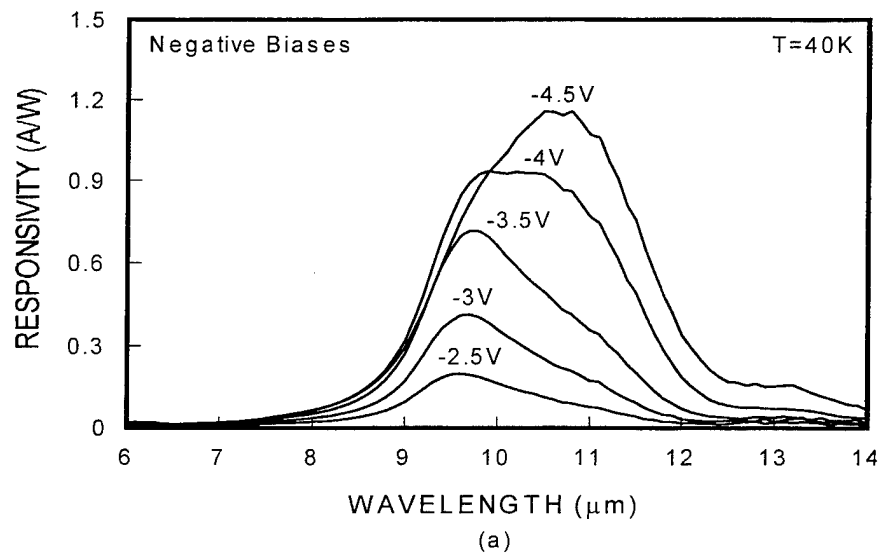
Figure 7.14 The spectral responsivity of the 7-period BB-QWIP measured at T = 40K, under (a) negative and (b) positive bias conditions.
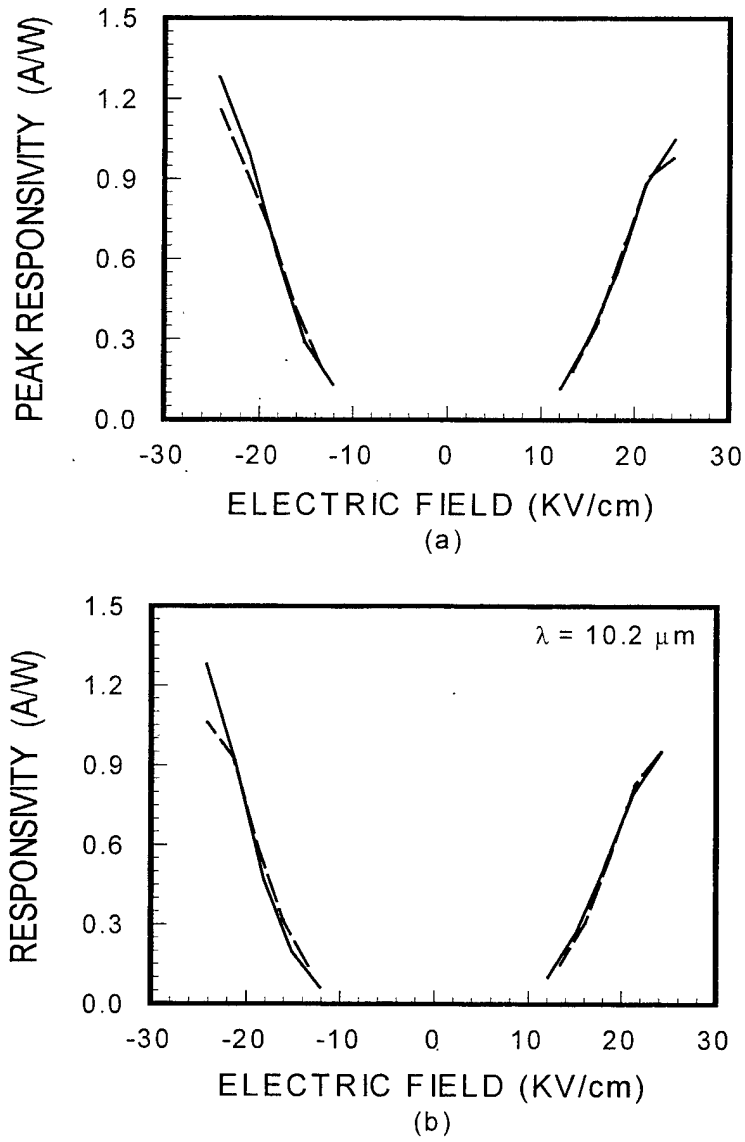
Figure 7.15 A comparison of the responsivity for the 3-period and 7-period BB-QWIPs as a function of the electric field: (a) the peak responsivity versus the electric field and (b) the responsivity versus the electric field at $\lambda = 10.2$ μm (the solid and the dashed lines are for the 3-period and the 7-period BB-QWIPs, respectively).

103
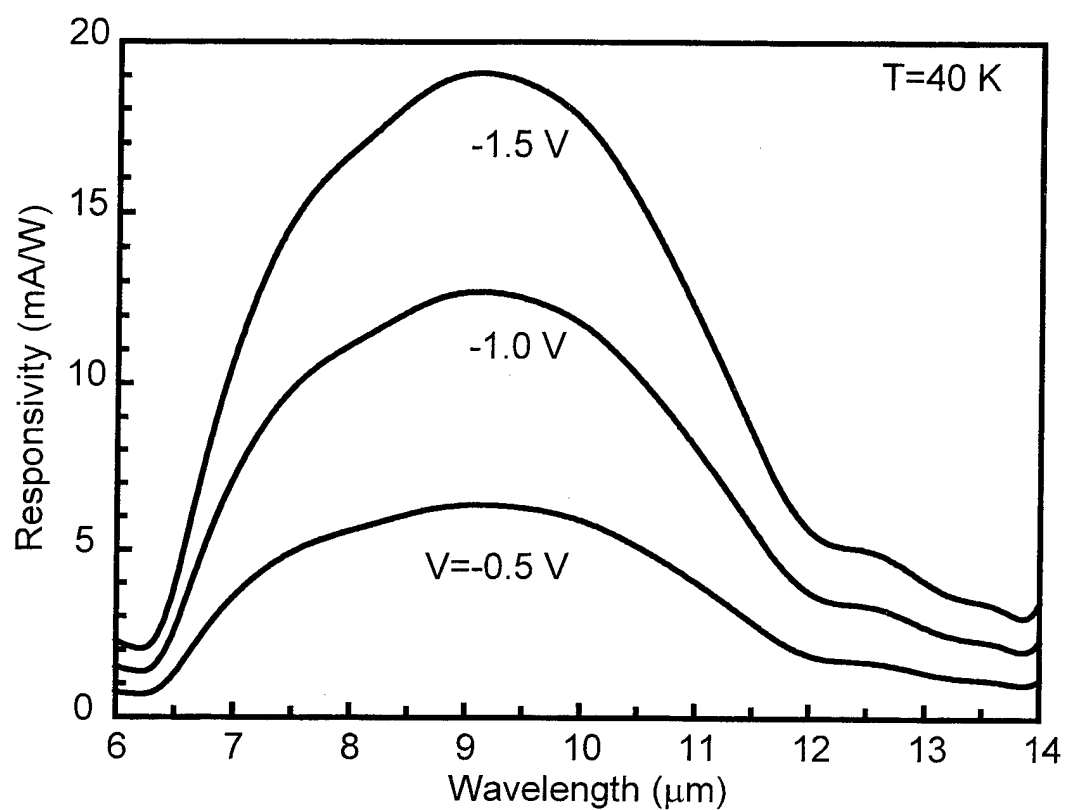
Figure 7.16 The responsivity versus wavelength of the p-type variable composition BB-QWIP under different applied biases and at T=40 K. The results were measured for a single pass at normal incidence.
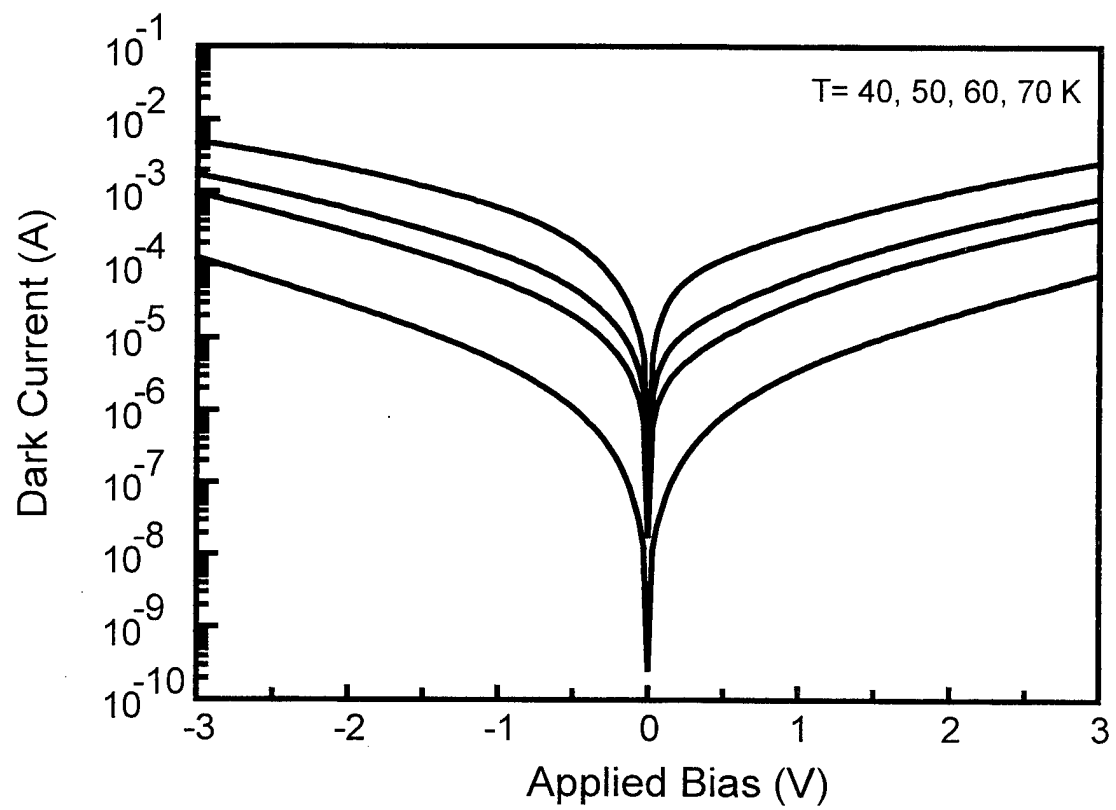
Figure 7.17 The measured dark I-V characteristics of the p-type variable composition BB-QWIP as a function of device temperature.
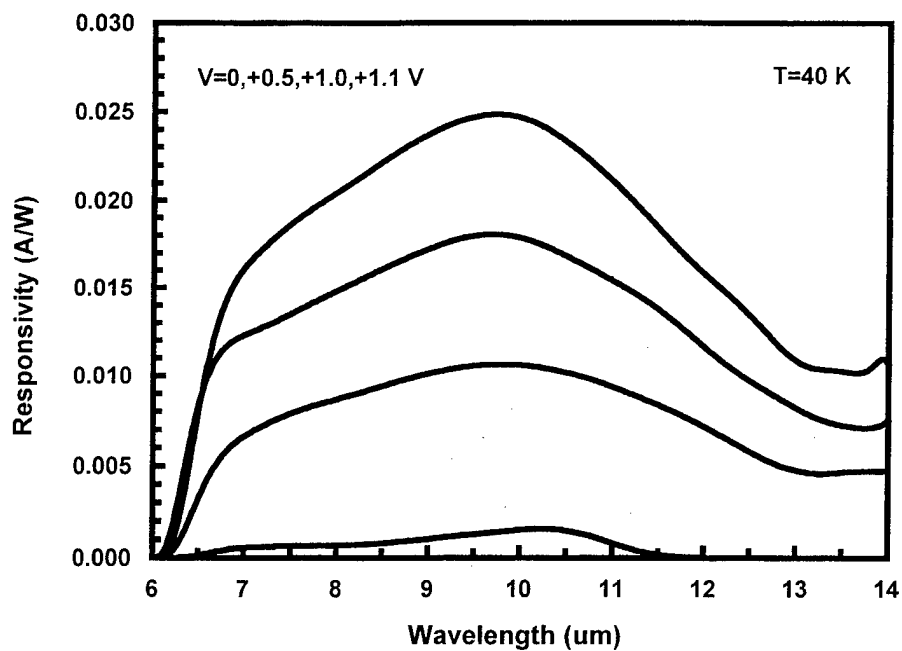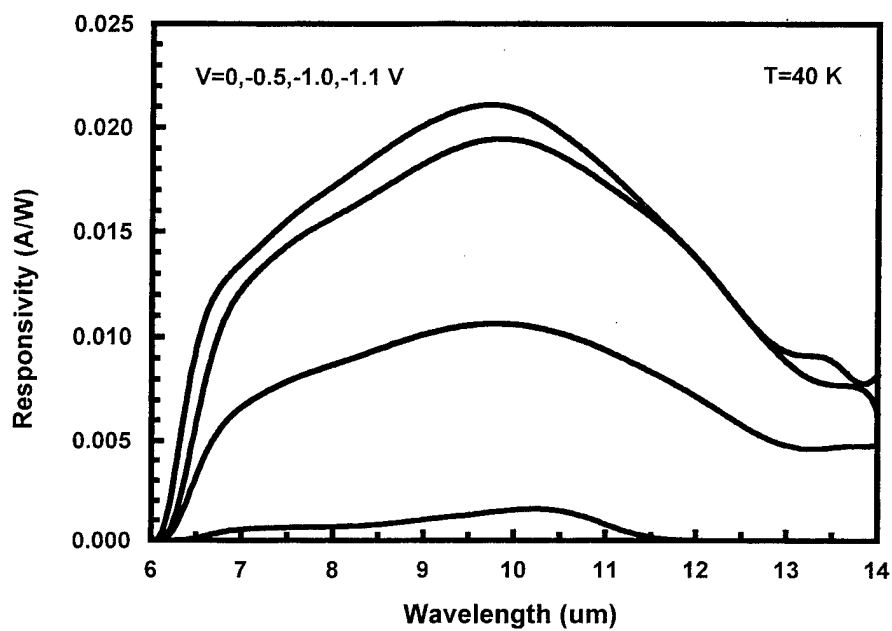
Figure 7.18 The responsivity versus wavelength of the p-type variable thickness BB-QWIP under (a) positive bias and (b) negative bias conditions.
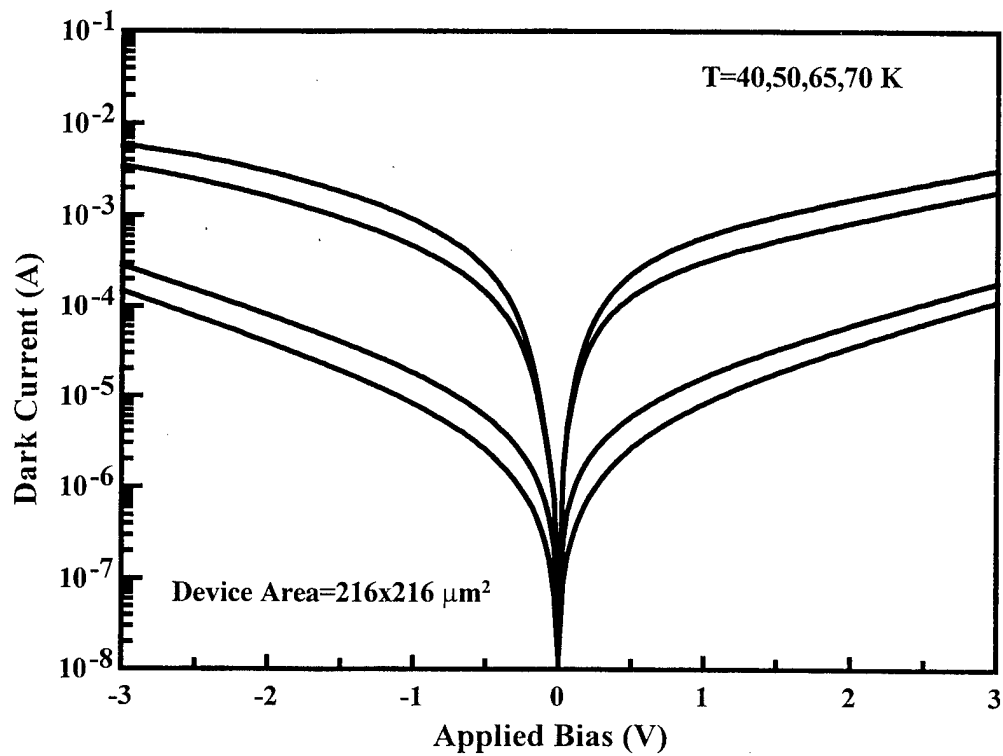
Figure 7.19 Measured dark I-V characteristics of the p-type variable thickness BB-QWIP at different temperatures.

8 CONCLUSIONS

In this report, we have presented several high performance and novel quantum well infrared photodetectors (QWIPs) for the 3-5 μm mid-wavelength infrared (MWIR) and 8-14 μm long-wavelength infrared (LWIR) detection. A high sensitivity high-strain InGaAs/AlGaAs/InGaAs triple-coupled (TC-) QWIP has been characterized for LWIR and low background applications. The broadband triple-coupled QWIP (BB-TC-QWIP) with high-strain three-stack TC-QWIP structure has been demonstrated for the LWIR detection. The three-, four-, and five-quantum well broadband QWIPs (BB-QWIPs) were also investigated for the LWIR detection. In addition, The high-strain, multi-color, two-stack QWIPs were developed for the MWIR and LWIR dual-band detection in which the top-stack was high-strain TC-QWIP for LWIR detection and the bottom-stack was bound-to-continuum (BC) QWIP for MWIR detection. The TC-QWIP grown InP substrate was also developed for MWIR detection. Finally, The high-strain InGaAs/GaAs QWIP with and without 2-D grating coupler has been characterized for LWIR detection. The results are described as follows:

- A very high sensitivity high-strain InGaAs/AlGaAs/InGaAs triple-coupled (TC-) QWIP has been developed in this work for LWIR and low background applications. The detector shows excellent responsivity, detectivity, and BLIP temperature. A linear wavelength tunability by applied bias is demonstrated in this TC-QWIP in the LWIR spectral window.

- A new InGaAs/AlGaAs/InGaAs broadband triple-coupled quantum well infrared photodetector (TC-QWIP) for 8-14 μm long-wavelength detection has been

fabricated and characterized. The three–stack structure was developed to detect the broader wavelength range, in which each stack has different peak wavelengths by varying Al composition and quantum well width. The peak responsivity and the BLIP detectivity (D^*) at $\lambda_p = 10.6$ μm, $V_b = -5.2$V, and T = 40K was found to be 2.75 A/W and 1.98 x 10^{10} cm-Hz$^{1/2}$/W, respectively.

- Design, fabrication, and characterization of a mid-wavelength infrared triple-coupled quantum well infrared photodetector (MWIR TC-QWIP) has been carried out. The peak responsivity at $\lambda_p = 4.6$ μm, $V_b = -5.5$V, and T = 77K was 0.31 A/W. The background limited performance (BLIP) detectivity (D^*) at $\lambda_p = 4.6$ μm was found to be 2.65 x 10^{10} cm-Hz$^{1/2}$/W at $V_b = -4.5$V, and T = 77K. This device can be operated up to T = 116K, and the spectral responsivity was insensitive to the temperature increase.

- A multi-color, two-stack, high-strain InGaAs/AlGaAs/InGaAs asymmetrical triple-coupled (TC-) and InGaAs/AlGaAs bound-to-continuum (BC) quantum well infrared photodetector (QWIP) for the LWIR and MWIR dual band detection has been demonstrated. For the LWIR TC-QWIP, the peak responsivity was 2.63 A/W at $\lambda_p = 10.3$ μm, $V_b = -7.8$V, and T = 40K. The corresponding BLIP detectivity was found to be 2.0 x 10^{10} cm-Hz$^{1/2}$/W. The spectral response of the MWIR BC-QWIP can be detected up to T = 120K, and the peak wavelength was at 5.1 μm. The three peak detection wavelengths at T = 40K and $V_b = -9$V were found to be at 5.1 μm, 7.6 μm, and 10.3 μm in this stacked- QWIP.

- An *n*-type GaAs/InGaAs high-strain bound-to-continuum quantum well infrared photodetector (HS BC-QWIP) for LWIR detection has been developed. The

activation energy depending on bias voltage has been analyzed to understand the dark current transport mechanism. A maximum responsivity of 8.16 A/W was obtained at $\lambda_p = 10.5$ μm, $V_b = -3V$ and $T = 35K$ for the $45°$ back-illumination. The HS BC-QWIP with the 2-D square mesh metal grating coupler was also measured at $T = 35K$. The bias voltage dependent activation energy has been analyzed to understand the dark current transport mechanism.

- Three-, four-, and five-well n-type and three-well p-type $In_xGa_{1-x}As/Al_yGa_{1-y}As$ broadband quantum well infrared photodetectors (BB-QWIPs) grown on the GaAs substrate for 7–14 μm long-wavelength detection have been demonstrated. For the n-type three-well BB-QWIP, a maximum bandwidth of $\Delta\lambda/\lambda_p = 21$ % was obtained at $V_b = -2V$ with the peak wavelength of $\lambda_p = 10$ μm. The n-type four-well BB-QWIP not only exhibits a very large responsivity of 2.31 A/W at $\lambda_p = 10.3$ μm and $V_b = 4.5V$, but also achieves a broader bandwidth of $\Delta\lambda/\lambda_p = 29$ % than the three-well device. For the 3-period five-well BB-QWIP, the maximum bandwidth and the background limited performance (BLIP) detectivity (D*$_{BLIP}$) were $\Delta\lambda/\lambda_p = 28$ % and 1.36×10^{10} cm-Hz$^{1/2}$/W at $V_b = 2V$ with a 1.05 A/W peak responsivity at $\lambda_p = 9.6$ μm. It is noted that the device performance was nearly insensitive to the QWIP period. The variable composition p-type BB-QWIP has a very large FWHM bandwidth of $\Delta\lambda/\lambda_p = 48$ % at $V_b = -1.5$ V and $T = 40$ K. The variable thickness p-type BB-QWIP was found to have an even broader FWHM bandwidth of $\Delta\lambda/\lambda_p = 63$ % at $V_b = 1.1$ V and $T = 40$ K, with a corresponding peak responsivity of 25 mA/W at $\lambda_p = 10.2$ μm.

The device performance for QWIPs developed in this project are summarized in Table 8.1, which lists the detection wavelength region, period, applied bias, operating temperature, peak wavelength, full-width half-maximum (FWHM) spectral bandwidth, spectral responsivity, and detectivity. The voltage tunable wavelength shift was obtained in both the LWIR and MWIR TC-QWIPs. A maximum spectral responsivity of 8.16 A/W was found in the high-strain InGaAs/GaAs BC-QWIP. The three-stack TC-QWIP can provide a broader bandwidth detection than that of the single-stack TC-QWIP. The multi-color detection covering both the MWIR and LWIR spectral regions was achieved in the stacked TC- and BC-QWIPs structure. In addition, the broadband detection for 8- 14 μm long-wavelength region was achieved in the 3-, 4-, and 5-well BB-QWIPs. In particular, a very broad FWHM spectral bandwidth of $\Delta\lambda/\lambda_p = 63$ % was obtained for the p-type 3-well BB-QWIP. The estimated BLIP detectivity (D^*_{BLIP}) was in the range of low to mid 10^{10} cm-Hz$^{1/2}$/W for QWIPs developed in this project. In view of the high responsivity, low dark current and high detectivity obtained in the high-strain TC-QWIPs developed in this project, it is recommended that further development of this detector for larger array focal plane array applications should be undertaken for LWIR and multi-color imaging array applications.

Table 8.1 Summary of the device performance for QWIPs developed in this project.

QWIP	Detection region	Period	Bias (V)	T(K)	λ_p (µm)	$\Delta\lambda/\lambda_p$ (%)	R_i (A/W)	D* (cm-Hz^{½}/W)
1 (n-type)	LW	10	-4.5	77	9.8	11	1.3	2×10^{10}(non-BLIP)
2 (n-type)	LW	14	-5.2	40	10.6	19	2.75	2×10^{10} (BLIP)
3 (n-type)	MW	10	-5.5	77	4.6	15	0.31	4.3×10^{9} (non-BLIP)
4 (n-type)	LW	20	-7.8	40	10.3	11	2.63	2×10^{10} (BLIP)
	MW	3	-1.3	77	5.1	16	0.27	1.2×10^{10} (BLIP)
5 (n-type)	LW 45°	20	-3	35	10.5	20	8.16	3.4×10^{10} (BLIP)
	LW grating					24	2.8	2×10^{10} (BLIP)
6	n-type LW 3-well	20	-4	40	10	18	1	3.1×10^{10} (BLIP)
	n-type LW 4-well		-4		10.3	29	1.5	2.3×10^{10} (BLIP)
	n-type LW 5-well	3	-2		10.2	24	1.28	1.4×10^{10} (BLIP)
		7	-4.5		10.5	23	1.16	1.3×10^{10} (BLIP)
	p-type LW 3-well*	20	-1.5		9.3	48	0.019	3.6×10^{9} (BLIP)
	p-type LW 3-well**		+1.1		9.6	63	0.025	9.5×10^{9} (BLIP)

Note:
1. High-strain (HS) TC-QWIP
2. Three-stack BB TC-QWIP.
3. MWIR TC-QWIP grown on InP substrate.
4. Two-stack, high-strain, multi-color, TC- and BC-QWIPs
5. High-strain InGaAs/GaAs BC-QWIP.
6. Three-, four-, and five-well BB-QWIPs.
* variable composition
** variable thickness

REFERENCES

1. K. L. Tsai, K. H. Chang, C. P. Lee, K. F. Huang, J. S. Tsang, and H. R. Chen, Appl. Phys. Lett. **62**, 3504 (1993).

2. A. Foire, E. Rosenchen, P. Bois, J. Nagle, and N. Laurent, Appl. Phys. Lett. **64**, 478 (1994).

3. L. H. Peng, and C. G. Fonstad, J. Appl. Phys. **77**, 747 (1995).

4. G. Karunasri, J. S. Park, J. Chen, R. Shih, J. F. Scheihing, and M. A. Dodd, Appl. Phys. Lett. **67**, 2600 (1995).

5. S. Y. Wang and C. P. Lee, Appl. Phys. Lett. **71**, 119 (1997).

6. L. S. Yu and S. S. Li, Appl. Phys. Lett. **59**, 1332 (1991).

7. J. Y. Anderson and L. Lundqvist, Appl. Phys. Lett., **59**, 857 (1991).

8. J. C. Chiang, Sheng S. Li, and A. Singh, Appl. Phys. Lett., **71**, 3546 (1997).

9. Daniel C. Wang, Gijs Bosman, Yeng H. Wang, and Sheng S. Li, J. Appl. Phys. **77**, 1107 (1995).

10. B. F. Levine, J. Appl. Phys. **74**, R1 (1993).

11. Yimin Huang and Chenhsin Lien, J. Appl. Phys. **78**, 2700 (1995).

12. Yimin Huang, Chenhsin Lien, and Tan-Fu Lei, J. Appl. Phys. **74**, 2598 (1993).

13. Jung-Chi Chiang, Sheng S. Li, M. Z. Tidrow, P. Ho, M. Tsai, and C. P. Lee, Appl. Phys. Lett. **69**, 2412 (1996).

14. Y. H. Wang, Sheng S. Li, and Pin Ho, Appl. Phys. Lett. **62**, 621 (1993).

15. L. C. Lenchyshyn, H. C. Liu, M. Buchanan, and Z. R. Wasilewski, J. Appl. Phys. **79**, 3307 (1996).

16. J. Chu, Sheng S. Li, and A. Singh, IEEE J. Quantum Electronics, **vol. 35**, pp. 312-318 (1999).

17. Y. H. Wang, S. S. Li, J. Chu, and Pin Ho, Appl. Phys. Lett. **64**, 727 (1991).

18. B. F. Levine, A. Y. Cho, J. Walker, R. J. Malik, D. A. Kleinman, and D. L. Sivco, Appl. Phys. Lett. **52**, 1481 (1988).

113

19. Y. H. Wang, Jung-chi Chiang, Sheng S. Li, and Pin Ho, J. Appl. Phys. **76**, 2538 (1994).

20. Yaohui Zhang, D. S. Jiang, J. B. Xia, L.Q. Cui, C. Y. Song, Z. Q. Zhou, and W. K. Ge, Appl. Phys. Lett. **68**, 2114 (1996).

21. Harald Schneider, Frank Fuchs, Bernhard Dischler, John D. Ralston, and Peter Koidl, Appl. Phys. Lett. **58**, 2234 (1991).

22. Yuzo Hirayama, Jurgen H. Smet, Lung-Han Peng, Clifton G. Fonstad, and Erich P. Ippen, Jpn. J. Appl. Phys. **Vol. 33**, pp. 890 (1994).

23. Takashi Asano, Susumu Noda, Tomoki Abe, and Akio Sasaki, Jpn. J. Appl. Phys. **Vol. 35**, pp. 1285 (1996).

24. Takashi Asano, Susumu Noda, Tomoki Abe, and Akio Sasaki, J. Appl. Phys. **82**, 3385 (1997).

25. J. H. Smet, L. H. Peng, Y. Hirayama, and C. G. Fonstad, Appl. Phys. Lett. **64**, 986 (1994).

26. S. D. Gunapala and K. M. S. V. Bandara, Thin Films **21**, 113 (1995).

27. B. F. Levine, K. K. Choi, C. G. Bethea, J. Walker, and R. J. Malik, Appl. Phys. Lett. **50**, 1092 (1987).

28. S. D. Gunapala, K. M. S. V. Bandara, B. F. Levine, G. Sarusi, D. L. Sivco, and A. Y. Cho, Appl. Phys. Lett. **64**, 2288 (1994).

29. L. B. Allard, H. C. Liu, M. Buchanan, Z. R. Wasilewski, Appl. Phys. Lett. **70**, 2784 (1997).

30. A. G. U. Perera, W. Z. Shen, S. G. Matsik, H. C. Liu, M. Buchanan, and W. J. Schaff, Appl. Phys. Lett. **72**, 1596 (1998).

31. S. Y. Wang and C. P. Lee, J. Appl. Phys. **82**, 2680 (1997).

32. C. J. Chen, K. K. Choi, W. H. Chang, and D. C. Tsui, Appl. Phys. Lett. **73**, 1272 (1998).

33. C. J. Chen, K. K. Choi, M. Z. Tidrow, and D. C. Tsui, Appl. Phys. Lett. **68**, 1446 (1996).

34. S. D. Gunapala, J. K. Liu, M. Sundaram, J. K. Park, C. A. Shott, T. Hoelter , T. I. Lin, S. T. Massie, P. D. Maker, R. E. Muller, and G. Sarusi, Proc. 3rd Int. Symp. on Long Wavelength Infrared Detectors and Arrays, **ECS-95-28**, 55-66 (1995).

35. M. Z. Tidrow, K. Bacher, Appl. Phys. Lett. **69**, 3396 (1996).

36. J. Y. Anderson, L. Lundqvist, and Z. F. Paska, Appl. Phys. Lett., **58**, 2264 (1991).

37. M. Z. Tidrow, Xudong Jiang, Sheng S. Li, and K. Bacher, Appl. Phys. Lett., **74**, 1335 (1999).

38. S. V. Bandara, S. D. Gunapala, J. K. Liu, E. M. Luong, J. M. Mumolo, W. Hong, D. K. Sengupta, and M. J. Mckelvey, Appl. Phys. Lett., **72**, 2427 (1998).

39. B. F. Levine, G. Hasnain, C. G. Bethea, and Naresh Chand, Appl. Phys. Lett., **54**, 2704 (1989).

40. Y. Zhang, N. Baruch and W. I. Wang, Eletronics letters, **vol. 29**, 213 (1993).

41. B. F. Levine, C. G. Bethea, V. O. Shen, and R. J. Malik, Appl. Phys. Lett., **57**, 383 (1990).

42. J. Y. Duboz, L. Saminadayar, and J. M. Gerard, J. Appl. Phys., **78**, 2803 (1995).

43. J. Chu, S. S. Li and P. Ho, J. Cryst. Growth, **vol. 175/176**, pp. 964-970 (1997).

44. M. Z. Tidrow, J. C. Chiang, S. S. Li and K. Bacher, Appl. Phys. Lett., **70**, 859 (1997).

45. M. Z. Tidrow, Mat. Chem. And Phys. **50**, 183 (1997).

46. J. Chu and S. S. Li, IEEE J. Quantum Elect. **vol. 33**, pp. 1104-1113 (1997).

47. S. D. Gunapala, J. K. Liu, M. Sundaram, S. V. Bandara, C. A. Shott, T. Hoetler, P. D. Maker, R. D. Muller, Proceedings of SPIE, **vol. 2744**, pp. 722-730 (1996).

48. A. K. Ghatak, K. Thyagarajan, and M. R. Shenoy, IEEE J. Quantum Electron. **vol. 24**, pp.1524-1531 (1988).

49. J. W. Matthews and A. E. Blakeslee, J. Cryst. Growth, **vol. 27**, pp. 118-125 (1974).

50. J. W. Matthews and A. E. Blakeslee, J. Cryst. Growth, **vol. 29**, pp. 273-280 (1975).

51. J. W. Matthews and A. E. Blakeslee, J. Cryst. Growth, **vol. 32**, pp. 265-273 (1976).

52. Landolt-Börnstein, O. Madelung, *ed.*, Berlin: Springer-Verlag, 1986, Group III, **vols. 17a and 22a**.

53. G. Ji, D. Huang, U. K. Reddy, T. S. Henderson, R. Houre, and H. Morkoç, J. Appl. Phys. **62**, 3366 (1987).

54. F. H. Pollack, Semiconductors and Semimetals, T. P. Pearsall, ed., New York: Academic Press, **vol. 32**, 1990.

55. H. Asai, and Y. Kawamura, Appl. Phys. Lett. **56**, 746 (1990).

56. H. Xie, J. Katz, and W. I. Wang, Appl. Phys. Lett. **59**, 3601 (1991).

57. R. T. Kuroda and E. Garmire, Infrared Phys. **vol. 34**, pp. 153-161 (1993).

58. K. Hirose, T. Mizutani, and K. Nishi, J. Crystal Growth, **vol. 81**, 130 (1987).

DISTRIBUTION LIST

AUL/LSE
Bldg 1405 - 600 Chennault Circle
Maxwell AFB, AL 36112-6424   1 cy

DTIC/OCP
8725 John J. Kingman Rd, Suite 0944
Ft Belvoir, VA 22060-6218   2 cys

AFSAA/SAI
1580 Air Force Pentagon
Washington, DC 20330-1580   1 cy

AFRL/PSTL
Kirtland AFB, NM 87117-5776   2 cys

AFRL/PSTP
Kirtland AFB, NM 87117-5776   1 cy

Dr. Sheng S. Li
Dept. of Electrical and Computer Engineering
University of Florida
Gainsville, FL 32611-6130   1 cy

Official Record Copy
  AFRL/VSSS/David Cardimona   1 cy